UNIVERSITY OF LIVERPOOL

School of Engineering

PhD Thesis

Tailored optical vector fields for ultrashort-pulse laser mirco-processing

Thesis submitted in accordance with the requirements of

the University of Liverpool for the degree of Doctor of Philosophy

By

Jinglei Ouyang

February 2016

School of Engineering
The University of Liverpool
Brownlow Street
Liverpool
L69 3GH
UK

Declaration

I hereby declare that all of the work contained within this dissertation has not been submitted for any other qualification.

Signed:

Date:

Abstract

In this thesis, a Spatial Light Modulator (SLM) and a nano-structured S-waveplate were integrated with a picosecond laser system and employed to generate complex vector optical fields. Precise tailoring of optical vector beams is demonstrated, shaping their focal electric fields.

Using novel optical setups, radial and azimuthal polarizations with and without vortex phase wavefront were created, producing complex laser micro patterning on a polished metal surface. Imprinting Laser Induced Periodic Surface Structures(LIPSS) elucidates the detailed vector fields around the focal region, which shows clearly how the Orbital Angular Momentum(OAM) associated with a helical wavefront induces rotation of vector fields along the optical axis of a focusing lens. In addition, unique, variable logarithmic spiral micro-structures were imprinted on the metal surface. These are the first experimental observations of such micro-structured spirals created by multi-pulse exposure with spiral vector fields which are shown to be due to superpositions of plane wave radial and azimuthal polarizations.

A comparative analysis of micro-drilling with radially, azimuthally, circularly and linearly polarized beams with various wavefront was also carried out. The results are compared in terms of quality and efficiency, illustrating how the distinct machining properties associated with each beam make it best suited for specific processes or materials. A radially polarized beam was considered as the most efficient at drilling high-aspect-ratio features.

By applying an axicon phase map on the SLM, annular shaped laser beams with adjustable dimension were created and employed in semiconductor thin film selective removal, which enhanced processing speed to a new level. Furthermore, annular beams with radial and azimuthal polarization were generated, imprinting complex concentric ring LIPSS pattern on a polished stainless steel surface. Side white light illumination tests demonstrated distinguishable bright strips on these rings due to diffractive properties of LIPSS, which offers a novel way in variable information encoding technologies.

Finally, synchronization of vector field polarizations with micro-positioning at a material surface was demonstrated, leading to potential industrial applications of this work.

Acknowledgment

I would like to thank everyone who encouraged and supported me during the time of my PhD.

Sincere acknowledge goes to my supervisors, Prof. Geoff Dearden and Dr. Stuart Edwardson, who always give me encouragement, help, advice and guidance through the ups and downs of my research. I would like to thank Dr. Walter Perrie and Dr. Olivier Allegre, for their invaluable advice, endless patience and support. Without their dedication, this work would not have been possible.

I am very grateful to everyone from the Laser Group of the University of Liverpool who was involved in my research, in particular, Dr. Zheng Kuang, Dr. Eamonn Fearon and Mr. Doug Eckford. And also appreciate all the kind help from my fellow students: Yang Jin, Linyi Ye, Liwei Fu, Guangyu Zhu

Additionally, I would like to thank the Scholarship of University of Liverpool Graduate Association (Hong Kong) for providing financial support for my PhD study at the University of Liverpool.

Finally, I would like to sincerely acknowledge my beloved wife, Yuan Wang, for her constant support and understanding, and my parents for their financial support and unwavering faith throughout my study in the UK.

Contents

List of publications to date

Journal Publication:

Ouyang, J., Perrie, W., Allegre, O., Heil, T., Jin, Y., Fearon, E., Eckford, D., Edwardson, S. and Dearden, G. (2015). ***Tailored optical vector fields for ultrashort-pulse laser induced complex surface plasmon structuring.*** Opt. Express, 23(10), p.12562.

Neale, A., Jin, Y., **Ouyang, J.**, Hughes, S., Hesp, D., Dhanak, V., Dearden, G., Edwardson, S. and Hardwick, L. (2014). ***Electrochemical performance of laser micro-structured nickel oxyhydroxide cathodes.*** *Journal of Power Sources*, 271, pp.42-47.

Zhai, Z., Kuang, Z., **Ouyang, J.**, Liu, D., Perrie, W., Edwardson, S. and Dearden, G. (2014). ***Synchronization control for ultrafast laser parallel microdrilling system.*** Holography, Diffractive Optics, and Applications VI.

Allegre, O., Jin, Y., Perrie, W., **Ouyang, J.**, Fearon, E., Edwardson, S. and Dearden, G. (2013). ***Complete wavefront and polarization control for ultrashort-pulse laser microprocessing.*** *Opt. Express*, 21(18), p.21198.

Jin, Y., Allegre, O., Perrie, W., Abrams, K., **Ouyang, J**., Fearon, E., Edwardson, S.P. and Dearden, G. (2013). ***Dynamic modulation of spatially structured polarization fields for real-time control of ultrafast laser-material interactions.*** *Opt. Express*, 21(21), p.25333.

Conference Publication:

Ouyang, J., Jin, Y., Allegre, O., Perrie, W., Fearon, E., Edwardson, S. and Dearden, G. (2015). ***Tailored optical fields and their application in ultrafast laser materials processing.*** Lasertagung Mittweida 2015, At University of Applied Sciences, Mittweida, Germany.

Ouyang, J., Perrie, W., Allegre, O., Jin, Y., Fearon, E., Edwardson, S. and Dearden, G. (2015). ***Advanced beam structuring for picosecond-pulse laser microprocessing.*** 4th Industrial Laser Applications Symposium (ILAS). Association of Laser Users, Kenilworth, pp45.

Ouyang, J., Allegre,O., Perrie,W., Jin,Y., Fearon,E., Edwardson,S.P., Dearden,G. (2014). ***Three-dimensional investigation of focal fields produced with ultrashort-pulse Cylindrical Vector Beams.*** Photon 14, London, Poster Section 2,P.34.

Jin, Y., **Ouyang, J.**, Perrie, W., Dearden, G. and Allegre, O. (2015) ***Wavefront and polarization structuring for shaping the focal fields of ultrashort-pulse laser beams.*** Lasertagung Mittweida 2015, At University of Applied Sciences, Mittweida, Germany.

Allegre, O., **Ouyang, J.** , Perrie, W. , Jin,Y, Edwardson S.P. and Dearden,G. (2015) ***Advanced beam shaping for ultrafast laser micro-processing.*** 38th International MATADOR conference proceedings , Huwei, Taiwan, pp73-78.

Allegre, O., Jin,Y, **Ouyang, J.** , Perrie, W. ,Edwardson S.P. and Dearden,G. (2013). ***Generation and analysis of radial polarization fields in a picosecond-pulse laser beam.*** Advanced Solid State Lasers, Paris France, JTh2A.14.

Allegre O, Perrie W, **Ouyang J**, Edwardson SP, Dearden G (2013). ***Experimental study of radially and azimuthally polarized ultrafast laser beams.*** Proceedings of the 2nd Industrial Laser Applications Symposium (ILAS). Association of Laser Users, Nottingham, pp 10

List of figures

List of tables

List of symbols

A	*n/a*	Amplitude of electric field
D	μm	Diameter
E	*n/a*	Electric field
E_P	μJ	Pulse energy
f	*mm*	Focal length
F	J/cm^2	Laser fluence
m	*n/a*	Topological charge
n	*n/a*	Refractive index
Δn	*n/a*	Refractive index change
λ	*nm*	Wavelength
Λ	μm	Pitch period of LIPSS
Δv	*Hz*	Gain bandwidth of frequency
φ	*n/a*	Phase of complex field
$\Delta\varphi$	*n/a*	Phase change of complex field
τ_p	*fs*	Pulse duration
ω_0	μm	Beam waist
σ	*n/a*	Standard deviation

List of abbreviations

AP	Azimuthal Polarization
APOAM	Azimuthal Polarization with Orbital Angular Momentum
CGH	Computer Generated Hologram
CP	Circular Polarization
CPOAM	Circular Polarization with Orbital Angular Momentum
CPA	Chirped Pulse Amplification
CW	Continuous Wave
CV	Cylindrical Vector
GUI	Graphical User Interface
HAZ	Heat Affect Zone
HWP	Half Wave Plate
IP	Intermediate Polarization
IPOAM	Intermediate Polarization with Orbital Angular Momentum
ITO	Indium Tin Oxide
KOH	Potassium Hydroxide
LCOS	Liquid-Crystal On Silicon
LIPSS	Laser Induced Periodic Surface Structures
OAM	Orbital Angular Momentum
QWP	Quarter Wave Plate
OV	Optical Vortex
RP	Radial Polarization
RPOAM	Radial Polarization with Orbital Angular Momentum
SESAM	Semiconductor Saturable Absorber Mirror
SLM	Spatial Light Modulator
TFP	Thin Film Polarizer

Chapter 1 Introduction

1.1 Research background and motivation

Ultrashort pulse lasers have expanded applications of materials modification and is a very useful and versatile tool in the micro-processing area, a relatively new research field which emerged in the mid 1990's. Ultrashort pulse lasers demonstrate high beam quality, thus allowing tight focusing for production of features at the micron scale and so precision micromachining is achievable. Furthermore, the ultrashort temporal pulse length created the possibility to control the time constant for the laser-material interaction and allowed minimal damage during ablation which reduces melt and results in a tiny heat affected zone. Pulse energy is compressed within a very short time-span, resulting in ultra high level peak powers.

In the past few years, the benefit of materials processing with cylindrical polarizations has been described by several research groups [1-3]. The outstanding advantage of these polarization states is that the complete surface is processed with the same spatially constant polarization state. This allows direction independent movement of the substrate and avoid the polarization effect during processing. For example, in micro-drilling using linear polarized laser beam for a high aspect ratios, the exit holes will appear distorted due to the polarization dependent Fresnel reflections[4].

Non-conventional beam shapes have the advantage that they can be explicitly designed to meet the requirements of a given material configuration or application that could not be feasible with either Gaussian or Top-hat beams. For instance, optical vortex (OV) beam with a well-defined orbital angular momentum (OAM) carries a helical wavefront with a phase singularity in the center [5]. It has been shown that the OAM effects on the laser ablation process by using OV beam provide smoother processed surfaces and deeper drilling than conventional beam [6]. Another example is the use of Bessel annular beams in percussion drilling offering optical trepanning with adjustable hole size has been demonstrated in drilling sub-millimeter size through-holes on stainless steel [7,8].

Both the two techniques above enhance the laser processing efficiency, hence by combining the control of laser beam polarization and wavefront together leads to an interesting approach and taking laser processing technique to a new level. Such an approach in laser-materials research has rarely been demonstrated and so this area is ideal for a research study.

1.2 Objective and contribution

The aim of this thesis is to highlight the capabilities of tailored optical vector beams with ultrashort picosecond pulses as an advanced technology in laser

micro-processing. Research was focused on the generation of cylindrical vector beams with various wavefronts and developing the method for analysis; also included the potential application in several research field. The main objectives of this thesis are:

- To elucidate the factors of generating highly advanced vector laser beams.
- To demonstrate the tailored laser beam during surface processing
- To demonstrate the use of tailored laser beams in micro-drilling
- Identify the optimized operating parameters in various applications.

In this thesis research, a unique method of combining polarization and wavefront control was explored by using a nano-structured waveplate (polarization control) and spatial light modulator (SLM, wavefront control) in the setup. As an SLM is a dynamic diffractive optic, dynamic modulation of the above two properties can be achieved. The surface micro-structures observed and measured laser beam intensity profiles during the experiments helped to confirm these two key factors unambiguously in accord with theoretical predictions.

In the surface processing experiments, the use of tailored vector beams open potential applications in optical data encoding and selective ablation in semiconductor manufacturing. Moreover, a comparison between the conventional beams and tailored vector beams in laser micro-drilling, generated considerable data

and showed how the influence of polarization state and intensity profile determine the processing speed and quality.

1.3 Overview of this thesis

Chapter 2 provides an introduction to relevant background information on ultrafast laser micro-processing, polarization and wavefront control of laser beams. A literature review of ultrafast laser surface processing and micro-drilling and their applications is included.

Chapter 3 provides a description of the experimental equipment, setup and methodology used to implement and analyze the experiments described in this thesis.

In **Chapter 4** a Spatial Light Modulator (SLM) and a micro-structured S-waveplate were integrated with a picosecond laser system and employed to structure the vector fields into radial and azimuthal polarizations with and without a vortex phase wavefront as well as superposition states. Imprinting Laser Induced Periodic Surface Structures (LIPSS) elucidates the detailed vector fields around the focal region. In addition to clear azimuthal and radial plasmon surface structures, unique, variable logarithmic spiral micro-structures with a pitch $\Lambda \sim 1\mu m$, not observed previously, were imprinted on the surface, confirming unambiguously the complex 2D focal

electric fields.

In **Chapter 5**, the produced vector beams were used for micro drilling, showing how the intensity profile and state of polarization in the focal plane influence the processing speed and quality. These results illustrate how tailored vector beams can be used to optimize laser micro-processing. The great advantage of the method described here is its flexibility, with an almost infinite range of optical field combinations.

In **Chapter 6**, the SLM with applied axicon phase map can generate the annular shape laser beam. The size of annular ring can be adjusted by the various axicon phase map. Combined with an S-wave plate, one can obtain annular beams with radial/azimuthal polarized states. The produced annular beams were used in thin film drilling, ITO removal and surface patterning.

Chapter 7 summarizes the results achieved in this research project and maps out potential future industrial applications and provides suggestions for future work.

Chapter 2 Literature review

2.1 Introduction to ultrafast lasers

Laser is an ideal tool to in the world of Micro-processing and is essential in future micro-engineering development. Laser micro-structuring is a method of fabricating small feature size structures, typically 100μm, or less, using laser beams from the near infrared to deep ultraviolet. The laser pulse length range has become shorter and shorter since the invention of laser in 1960s [9]. Only decades ago, Q-switched, 10ns pulses would be the shortest obtainable but after the introduction of mode locking techniques[10,11],picosecond and now femtosecond lasers are applied industrially. Even shorter pulses, termed attosecond (10^{-18}s) can be generated and observed in the laboratory [12], and the trend for generating ever shorter pulses has never stopped. Precision micromachining with few exceptions is carried out with nanosecond (ns), picosecond (ps) or femtosecond (fs) laser pulses. In the main case, Ultrashort pulse laser micro-processing of materials is a relatively new research field which emerged in the mid of 1990s.[13] After that, it was recognized that the advantages of ultrashort pulse laser over ns for micro-processing of materials was significant and research in this field sharply increased throughout the world. Ps and fs pulse length of the ultrafast lasers can interact with the material in so short a time scale that thermal effects can be negligible. This created the possibility to precisely control the time constant for the laser-material interaction and allowed minimal thermal damage during material structuring or material removal. Furthermore, ultrashort pulse laser often have high beam quality, hence fine focusing allows the

production of features at the micron scale.

Producing such fs pulse durations at the level of pulse energy required for micro-manufacturing processes is generally achieved with a combination of advanced optical techniques, such as mode locking, and Chirped Pulse Amplification (CPA). Mode locking enables the production of extremely short, low energy nanojoule (nJ) laser pulses, whereas CPA enables their amplification to achieve a pulse energy in the millijoule (mJ) range, as required in micro-manufacturing applications. For generating ps laser pulses, CPA can be avoided and uses an active medium based on neodymium-doped crystals (e.g. Nd:YAG or Nd:YVO_4), which allow for direct diode pumping.

Most of the experimental work described in this thesis uses a ps-pulse laser source, namely a High-Q IC-355-800 Nd:VAN regenerative amplifier laser. This laser source has a diode pumped mode locked Nd:VAN oscillator (30MHz) and a regenerative amplifier to produce an energetic (200μJ), 10 ps pulse train at a wavelength of 1064nm and 5-50kHz rep. rate.

2.1.1 Mode locking

Mode locking is a technique which is used to produce ultrashort laser pulses by inducing a fixed phase relationship between the oscillating electromagnetic field modes (i.e. the longitudinal modes) of the laser's optical cavity. This was first proposed by Lamb in 1964 [14] and observed experimentally by Hargrove et al [15]. By their nature, ultrashort-pulse lasers emit radiation over a broad range of wavelengths. Thanks to mode locking, the wavelength components are timed exactly so that their electromagnetic field modes nearly cancel each other out, except for during a tiny period of time when they combine constructively in one intense pulse (see Fig.2.1).

The wavelength of electromagnetic radiation modes that oscillate in a laser's optical cavity are determined by two factors. The first one is the lasing transitions that occur in the laser gain medium. In an ultrashort-pulse laser, the gain medium is chosen to have a broad range of lasing transitions (i.e. a large gain bandwidth $\Delta\nu$). For example, a titanium-doped sapphire has a lasing wavelength range of approximately 300nm centered near 800nm i.e. a gain bandwidth $\Delta\nu$ of 130THz, and hence can support a temporal pulse-length $\tau = 1/\Delta\nu = 8$fs [16]. The second factor is the length of the optical cavity that surrounds the gain medium. The cavity length allows a set of discrete wavelength components (i.e. those that have an electromagnetic field mode with nodes at the cavity's end mirrors) to be amplified. By mode locking a

broad range of wavelengths, an ultrashort pulse is produced at a dynamic point in the cavity, at which the many electromagnetic field modes interfere constructively. This point of coincidence moves back and forth in the cavity at the speed of light.

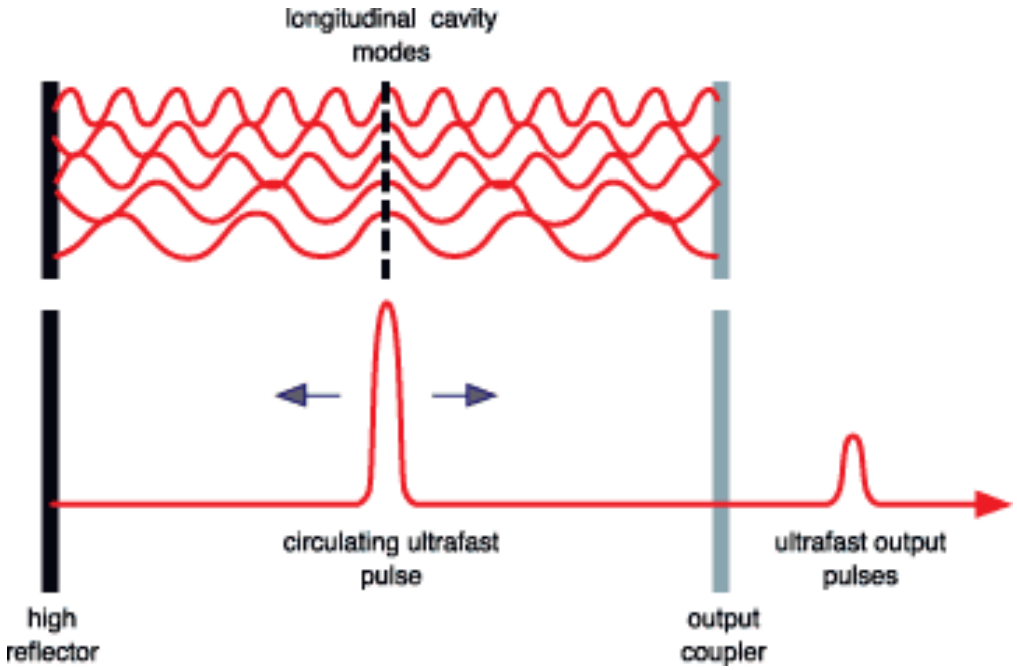

Fig. 2.1 *A number of longitudinal modes in the laser cavity produce the resultant output ultrashort pulse.[17]*

It is noted that mode locking does not occur naturally in a laser cavity. Without using an appropriate mode locking technique, the phase of each mode in the free running laser cavity would be uncorrelated from the other modes and the resulting output mode structure would fluctuate randomly. Mode locking can be achieved through a variety of techniques, separated into two groups: active mode locking and passive mode locking.

Active mode locking uses a dynamic light modulation device in the laser cavity,

externally driven with a synchronized signal. This is usually an acousto-optic modulator, which acts as a controllable attenuator. The light bouncing between the mirrors of the cavity is either attenuated when the device is “off”, or transmitted through when it is “on”. The modulator is “switched on” periodically each time the pulse has completed a cavity round trip.

Passive mode locking does not require any external input signal, and instead relies on the addition of a saturable absorber to allow modulation of losses by the cavity itself. A common saturable absorber used in many ultrashort lasers system is a semiconductor saturable absorber mirror (SESAM) which has a lower reflectivity for low-intensity light and higher reflectivity for ultrashort high intensity pulses.

It is noted here that lasers which operate in a continuous wave fashion (CW laser) have their electromagnetic radiation modes oscillating randomly in the laser cavity, with no fixed relationship between each other. This leads to a near-constant output intensity with no laser pulses.

2.1.2 Chirped Pulse Amplification (CPA)

For the fs ultrashort pulse laser oscillator usually operates at a higher pulse repetition rate (i.e.~20-30MHz), the pulse energy is in the range of nJ which is too low for the material processing, hence amplification to the μJ-mJ level is necessary. However, directly amplifying the ultrashort pulse would lead to damage of the optical components inside the amplifier due to the high peak intensity level of the pulses. In addition, the effect of non-linear self-focusing at ultrahigh peak powers associated with these pulses creates filamentation damage inside optical materials. The technique of Chirped Pulse Amplification(CPA) has been developed to avoid this limitation, using the large bandwidth associated with fs pulses [18]. As illustrated in Fig.2.2, which schematically shows the principle of CPA, there is a pulse stretcher between the oscillator and amplifier, increasing the pulse duration by a factor of 10^3–10^4 times, using a dispersive delay line hence reducing the peak power by this factor to avoid damage. Then, the stretched pulse can be safely amplified, neatly avoiding non-linear effects which would otherwise lead to component damage. Finally, in the compressor, the amplified long pulse containing the full bandwidth can be recompressed back to its original pulse duration with ~ mJ pulse energy.

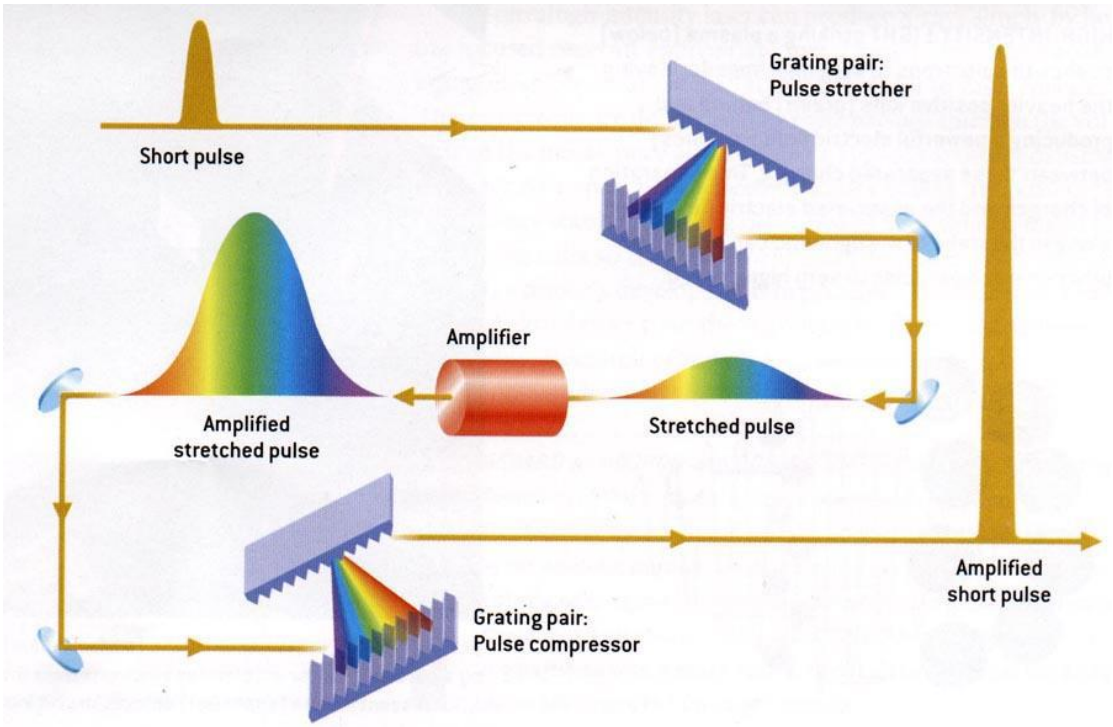

Fig. 2.2 *Schematic diagram of chirped pulse amplification.[19]*

2.1.3 Regenerative amplifier based on neodymium-doped crystals

From above description, the CPA technique is considerably complex, which bring the difficulty to reduce the size of the laser system. In addition, the tolerance of alignment on stretcher and compressor are quite strict in CPA system maintaining, which leads impractical operation in an industrial manufacturing environment.

Since recent investigations demonstrated that pulse duration in the range of several picoseconds are well suited for the precise machining of metals [20, 21], ps laser systems, which are much simpler and more cost effective, have been reported [22-27]

and manufactured [28,29]. As based on neodymium-doped crystals, which allowed direct diode pumping in the active medium to generate ps laser pulse. Moreover, due to the longer pulse duration than fs, the pulse intensity is not sufficiently high. In this case, CPA is not necessary to avoid any optical components damage inside the amplifier, which cause the whole ps laser system more compact.

Fig.2.3 shows a schematic of a Nd:VAN regenerative amplifier, the main components are the optical resonator formed by a series of high-reflective mirrors, Nd:VAN crystal pumped by a diode laser and an electro-optical modulator (Pockels cell). The picosecond seed oscillator generates pulses with MHz level repetition rate, then the pulses are injected into the regenerative amplifier through a optical isolator which consisted with a Faraday rotator and a half-wave plate(HWP). In combination with a thin-film polarizer (TFP) and a quarter-wave plate (QWP), the Pockels cell allows the injecting the laser pulses selected into the cavity of the amplifier. Finally, after several round trips, the amplified pulses can be ejected from the resonator by the same optical elements, the pulse picker here can be used to select the certain repetition rate pulse train with user's requirement.

Nowadays, commercial picosecond lasers based on this oscillator amplifier system can generate 10ps laser pulses with maximum $Ep \approx 200\mu J$, e.g. High-Q IC-355- 800, the picosecond laser system employed for current research (which will be discussed

in more detail in Chapter 3.1). The output repetition rate of the pulses is tuneable up to 50 kHz.

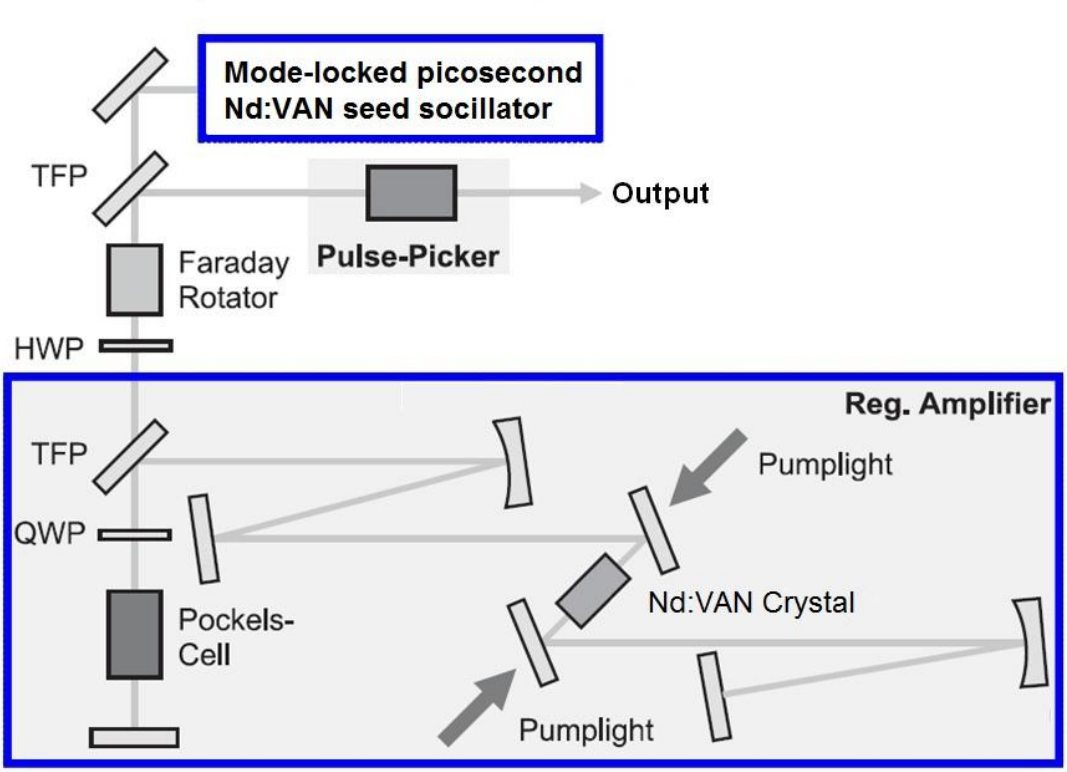

Fig. 2.3 *Schematic of the picosecond Nd:VAN oscillator amplifier*.

2.2 Laser-material interactions mechanisms

The most fundamental difference between long pulse lasers and ultrashort systems are the extremely high intensities that arise as a consequence of the ultrashort pulses. The key differences between long pulse and ultrashort pulse laser material interaction is summarized below.

2.2.1 Long pulse regime

Micro-machining materials such as metals or semiconductors in the long-pulse regime is a dynamic process where the material close to the surface of the work-piece is heated, molten and finally vaporized within the duration of each pulse [30,31] In this regime, laser pulses transfer most of their energy thermally by melting the material. the ablation and material removal is accomplished through melt expulsion mainly driven by the vapour pressure (see Fig.2.4).

The processing can be very unstable due to the complicated fluid dynamics of the fluid phase. The heat diffusion is sometimes associated with the formation of surface shock waves. While the amplitude of the shock waves varies with the material being processed, it is generally true that the more energy is deposited in the micromachining process, the stronger the associated shock waves. Additionally, the resolidification of the melt can lead to irregular shapes of the crater, which cause different mechanical properties from the original material.

For any given machining process, a balance has to be found between efficiency and quality. For example by increasing the pulse energy, more material is ablated by each pulse, making the process more efficient; however, this also produces more recast material on the sidewalls of the machined structures and this reduces the process quality.

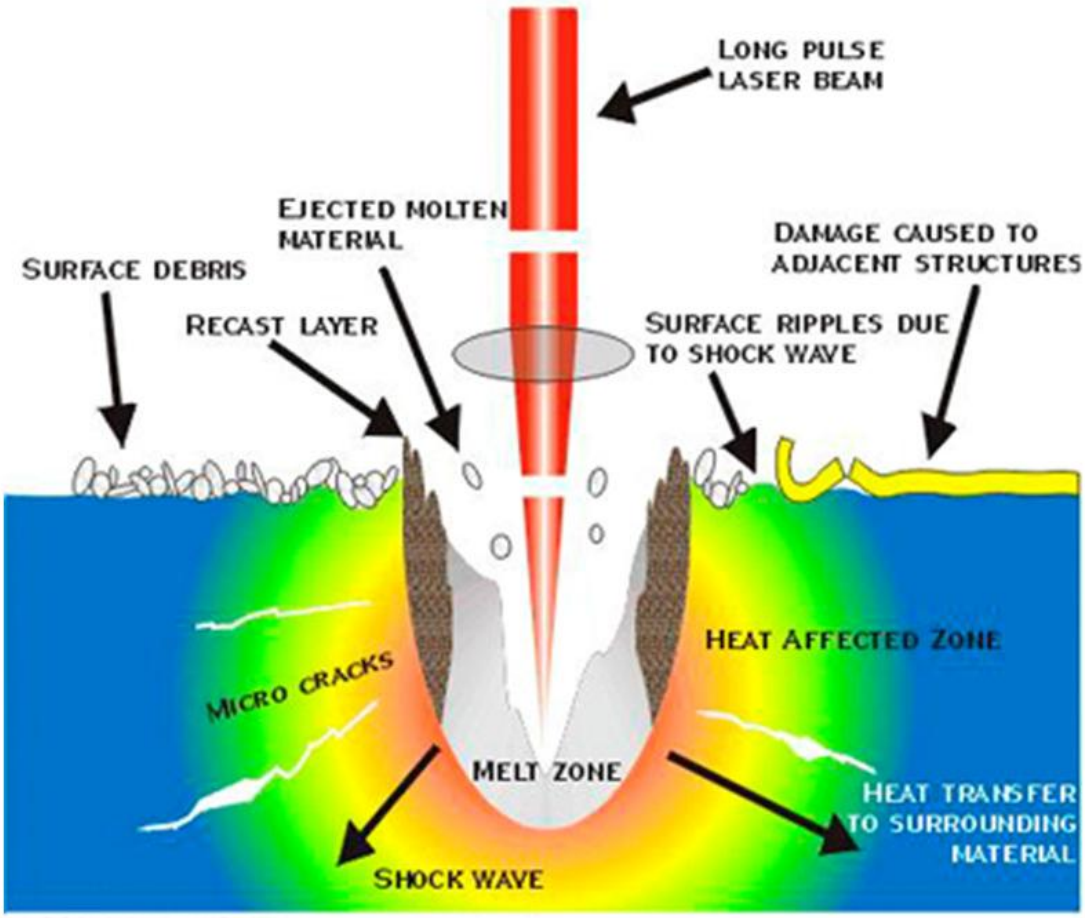

Fig. 2.4 *Schematic of long pulse induced laser material ablation.[31]*

2.2.2 Ultrashort pulse regime

In the ultrashort-pulse regime (see Fig.2.5), With ps/fs pulses, laser energy absorption and lattice heating takes place on an ultrafast timescale so that heat diffusion is negligible on this timescale. A thin, solid layer is transformed rapidly to a solid state, high temperature plasma (well above the material melting point), almost eliminating melt and removing the layer by direct vaporization away from the surface [33,34]. Most of this is accomplished before the next laser pulse induced, and there is rapid cooling due to the steep temperature gradient. In this case, the heat diffusion is further reduced by the fact that a large amount of the absorbed laser

energy is carried away by the direct vaporization. In contrast to the long pulse case, the ablation and material removal become highly precise with nearly no heat affect zone (HAZ).

In some semiconductors or dielectric materials, the intense energy transfer to the electrons causes their separation from the bulk material, leaving behind ions which repel each other and leave the bulk substrate material. This process is referred to as a Coulomb explosion [35].

Another example of an energy transfer mechanism is multi-photon absorption, which occurs in some dielectrics. Here, the high peak power of the ultrashort pulses causes the laser photons to excite molecules within the target material to their higher energy state.

In metals, each laser pulse locally heats electrons. Contrary to the light-weight electrons, the heavier ion lattice of the material cannot absorb optical radiation energy directly since they cannot follow the fast oscillations of the electromagnetic field. However, by collisions with the energetic electrons, the ion lattice is also heated up eventually. Due to the large mass difference between electrons and ions, only a small energy portion can be transmitted by each electron-ion collision [36]. Thermodynamic equilibrium between the electron system and the lattice is only reached after a time delay in the picoseconds range, after which the transferred

energy vaporizes the material. when the duration of the laser pulse is shorter than this time delay, it does not transfer its energy to the lattice directly. This reduces melt formation and thermally induced stress and it leads to a better process quality.

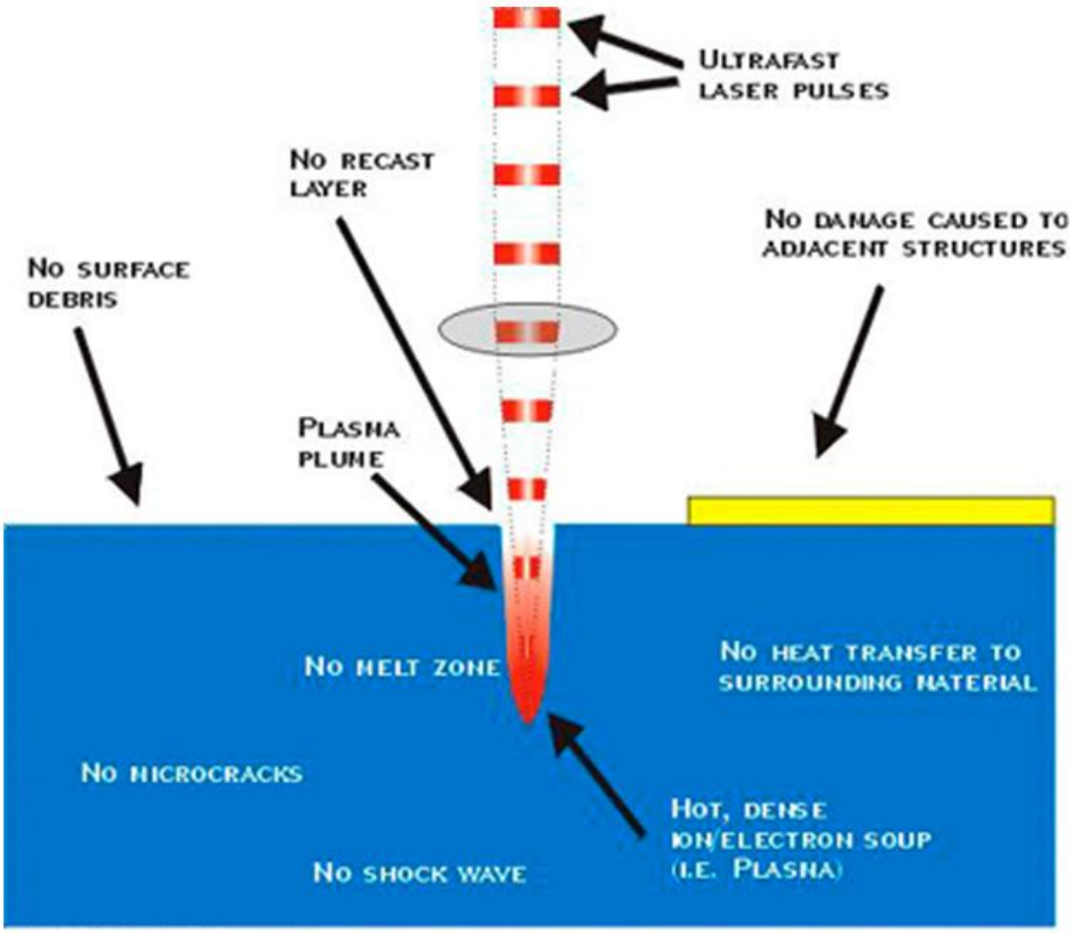

Fig. 2.5 *Schematic of ultrashort pulse induced laser material ablation.[31]*

2.3 Introduction to phase and polarization

An electromagnetic wave produced by laser radiation can be described as a self-propagating, transverse oscillating wave of electric and magnetic fields. The electric and magnetic fields both oscillate perpendicularly to the direction of wave propagation and perpendicularly to each other. Each of these fields can be described as a sinusoidal function, oscillating in both space and time.

2.3.1 Phase

If we plot the electric field along the axis of propagation of the laser beam at a given time, there are places along the axis where the field is at a maximum amplitude (i.e. a maximum positive field), places where it is zero and other places where the field is at a minimum amplitude (i.e. a maximum negative field), forming a sinusoidal function overall (Fig.2.6-a). These places along the axis of propagation represent different phases of the wave [37]. In other words, the phase of an electromagnetic wave can be defined as the location where the sinusoidal function has a given amplitude value (Fig.2.6-b). The solid lines indicate the places where the field is at a maximum $+A$, the dashed lines indicate the places where it is at a minimum $-A$. Each of these places represents a phase of the wave. The concept of phase is valuable in the context where a group of coherent electromagnetic waves travel together in the same direction, as is the case in a laser beam. In such cases, it can be useful to describe a phase front (also referred to as wavefront) as a surface defined

by the locations in space where all the sinusoidal functions have the same amplitude. In an undisturbed collimated laser beam, the phase front is generally a planar surface.

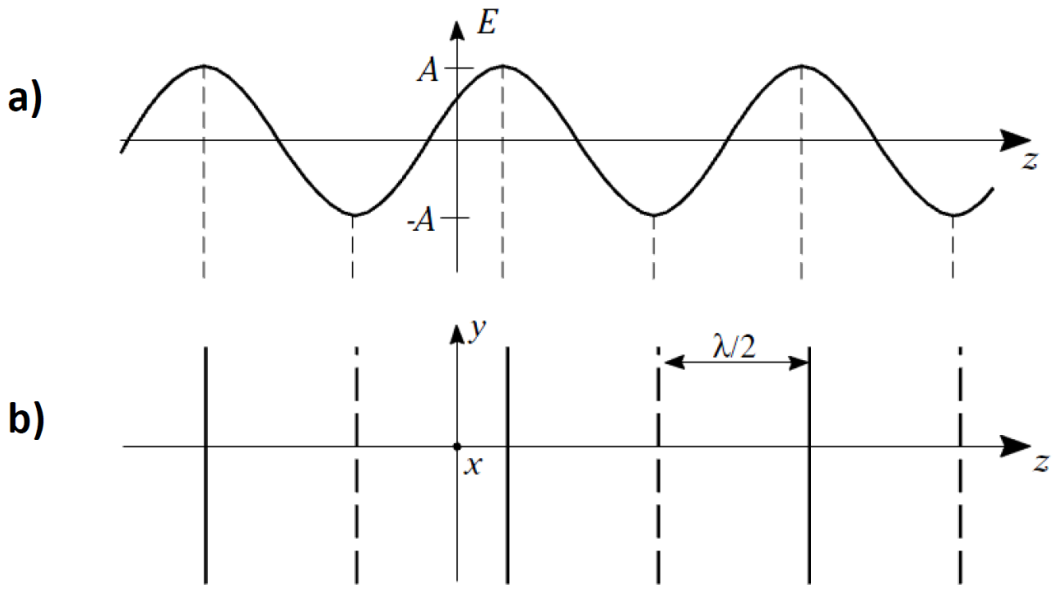

Fig. 2.6 *Schematic showing a) amplitude of the electric field E of an electromagnetic wave oscillates along the direction of propagation z; b) phases of the wave.*

2.3.2 Polarization

Polarization is one important property of light. This vector nature of light and its interactions with matter make many optical devices and optical system designs possible. The polarization of electromagnetic waves is a property related to the orientation in which electric field components oscillate. By definition, it is described by specifying the orientation of the wave's electric field at a point in space, over one period of oscillation of the wave [37].

The output beam polarization of lasers is often linear polarization, and in some

application it converted to circular polarization. Linear polarization is defined as the wave's electric field oriented in a single direction for the propagation; circular polarization is defined as two plane waves of equal amplitude while differing in phase by 90 ° during propagation. If the two electric field components vary in amplitude with fixed phase difference, the electric field can rotate clockwise or counter clockwise as the wave propagates, which is called elliptical polarization [38]. Fig.2.7 shows a schematic diagram of these different polarizations. Linear, elliptical and circular polarizations are termed spatially homogeneous, so that the state of these polarizations do not depend on the spatial location in the beam cross section.

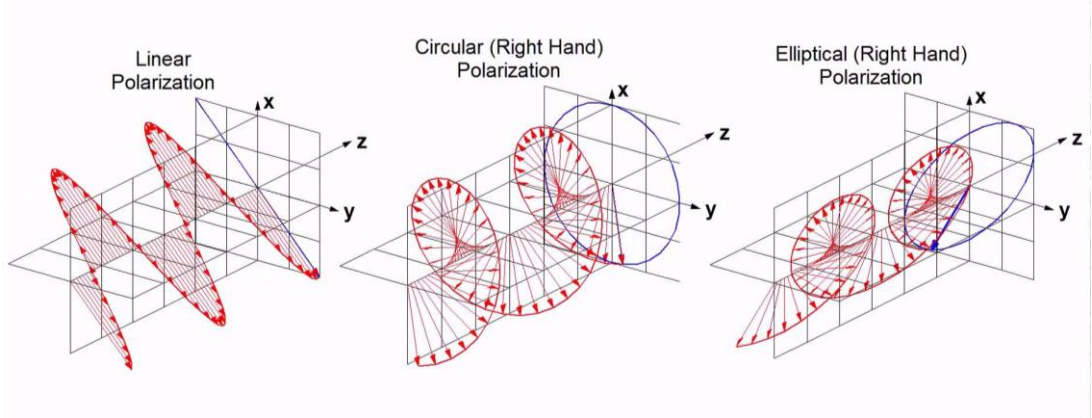

Fig. 2.7 *Schematic diagram of different polarizations.[39]*

Recently there has been an increasing interest in light beams with spatially varying state of polarizations. For example, laser beams with cylindrical symmetry in polarization, are termed cylindrical vector (CV) beams. The CV beams are vector-beams obeying axial symmetry in both amplitude and phase [40]. Radial and

azimuthal polarization are the extreme example of CV beams. Referring to Fig.2.8, a beam of light has radial polarization, if at every position in the beam, the polarization electric field vector points towards the centre of the beam. In this case the beam is divided into segments, and the average polarization vector of each segment is directed towards the beam centre. The orthogonal state to that of Radial is termed azimuthal polarization, in which the polarization vector is tangential to the circular beam. Note that the phase in these states is still planar.

If a laser is focused along the optic axis of a birefringent material, the radial and azimuthal polarizations focus at different planes. A spatial filter can be used to select the polarization of interest [41].

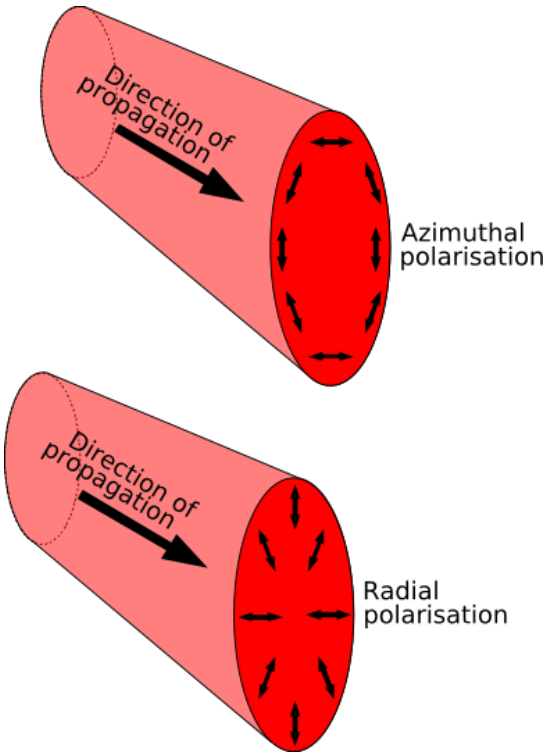

Fig. 2.8 *Schematic of radial and azimuthal polarization.*

2.3.2.1 Generation of CV beam

There are various methods which have been developed to generate CV beams since 1972 [42,43], depending on whether the generation methods involve amplifying media. These methods can be categorized as active or passive.

Typically, active methods involve the use of laser intracavity devices that force the laser to oscillate in CV modes. Intracavity devices can be an axial birefringent component or axial dichroic component to provide mode discrimination against the fundamental mode [42].

Passive methods convert the spatially homogeneous polarizations (typically linear or circular polarization) into CV polarization outside the laser cavity by applying birefringent or dichroic materials. For instance, a birefringent radial converter is a device that has its local polarization transmission axis aligned along either the radial or the azimuthal directions. When circularly polarized beam as input, the beam after the converter will be either radially or azimuthally polarized, depending on the handedness of the input beam [44]. However, the output also gains a spiral phase factor $e^{i\varphi}$, hence, to obtain a true CV beam, a spiral phase element with the opposite helical phase is needed to compensate phase to maintain planar wavefront of the output beam.

Another very popular and powerful passive method is using Spatial Light Modulator (SLM). Despite its relatively high cost, SLM offers the flexibility and capability to generate an almost arbitrary complex field distribution(detailed in Chapter 2.4). One such example is shown in Fig. 2.9 [45,46]. In this setup, two SLMs were used. The first SLM applied a spiral phase pattern which altered the input beam wavefront. The second SLM combined with the waveplates was used to control the polarization, where the degree of rotation is determined by the phase retardation of each pixel on the SLM. Proper configuration of these two SLMs setup allows the input linear polarization to be converted into any arbitrary polarization distribution, including CV beams. Note that, the SLMs also enable dynamic control, hence the state of polarization can be modulated in real-time.

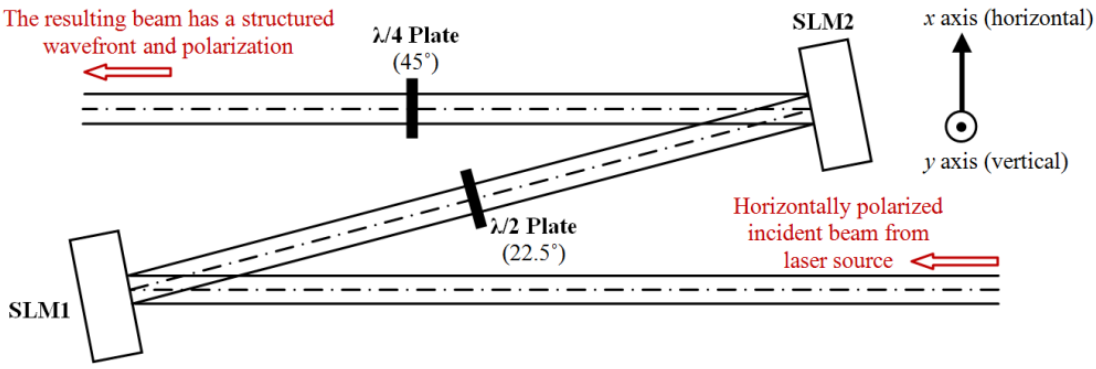

Fig. 2.9 *Schematic of the SLM Converter, which consists of two SLMs and two zero-order waveplates.SLM1 instigates a phase pattern designed to structure the beam wavefronts. After SLM1, the horizontal polarization pass through a half-waveplate with tilt angle of 22.5 ° . SLM2 and the quarter-waveplate with tilt angle of 45 ° are used to convert the incident linear polarization into the desired state of polarization. [45]*

Another methods for generating CV beams is a polarization converter plate, based

on using spatially variant retardation axis arrangements. For instance, a half-wave plate with continuously varying slow axis direction can be constructed in a silica glass plate by using femtosecond laser imprinting [47] , which rotates the incident linear polarization by the angle necessary to produce a radial or azimuthal distribution of the electric field (see Fig.2.10). By using this method, the output beam gains a planar wavefront without spatially variant phase, which is pure CV beam.

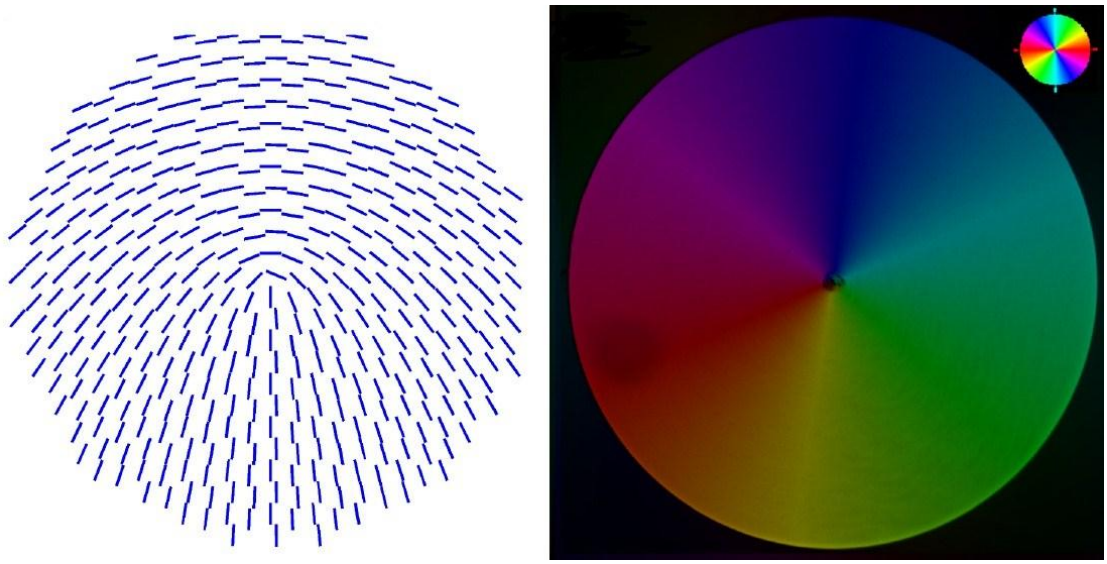

Fig. 2.10 *Schematic drawings of nanogratings distribution in half-wave polarization converters by Femtosecond laser imprinting, which convert linear incident polarization to radial or azimuthal polarization. The pseudo color indicates direction of the slow axis.[48]*

2.3.2.2 Applications of CV beam

Under very high-NA focusing with CV beams, the *z* component, can dominate the total focal field distribution which determines the focal spot size. For radially polarized incidence, it will contain a strong and narrower longitudinal component on

the focal optical axis, while the radial component gains a donut shape with a zero amplitude and no azimuthal component for this case [48].This unique focal distribution of vector field consequently leads to a smaller spot size compared with other polarizations, which has applications in high-resolution imaging, and can improve spatial resolution in microellipsometry [44]. Moreover, due to the polarization symmetry, the electric field at the focus of radially polarized beam has an extremely strong *z* component. This property is very useful for 3D stable trapping of metallic nano praticles[49].

Laser micro-machining is a fast growing application in industrial manufacturing and widely used. The focused laser beam intensity profile and polarization state is an important factor in this field. CV beam laser machining has been studied in several research groups, and shown to increase the efficiency for high aspect ratio during laser cutting [50] and drilling [51] of metal sheet when compared with linear or circular polarization. This will be detailed in Section 2.6.

2.4 Spatial Light Modulator (SLM) technology

Spatial Light Modulator (SLM) is a powerful device based on liquid-crystal technology for modulation of both phase and polarization of an incident beam of light. They can be divided into electrically addressed SLM and optically addressed

SLM; When optically addressed, they can be divided into reflective SLM and transmissive SLM. In the experimental work of this thesis we used a phase only, reflective type, Liquid-Crystal On Silicon (LCOS) SLM manufactured by Hamamatsu Photonics (see Fig.2.11).

Fig. 2.11 *Liquid-Crystal On Silicon (LCOS) SLM manufactured by Hamamatsu Photonics. [52]*

This SLM has a parallel-aligned nematic liquid crystal layer covered by a protective glass substrate with a coated transparent electrode. All these layers are attached to a reflective silicon substrate (see Fig.2.12). The silicon substrate is a Charge-Coupled Device (CCD) chip, having a two dimensional 20μm size pixel array structure which can electrically load data from the Computer Generated Holograms (CGHs). Each pixel is independently driven by an accurate voltage (related to grey levels in CGH). Each pixel contains electric field E, which will lead to the changes in the refractive index change (Δn) of the liquid crystal[53]. When the input light is reflected by the silicon substrate while passing though the liquid crystal twice, the phase of the

output will be modulated by the refractive index change of liquid crystal. With a graphical user interface (i.e. monitor display) connected with the SLM, the generated CGHs can be displayed on the monitor as a bitmap file with grey level variation determining each pixel's phase change Δφ. As the CGHs are displayed as 8 bit, the bitmap has 2^8=256 grey levels, hence the phase change Δφ can be symbolized by the 0-255 grey levels. Fig.2.13 shows a typical phase modulation characteristic, showing a high level of linearity between grey level and phase shift. A phase shift of 2π radians or more as input grey level is increased can be achieved.

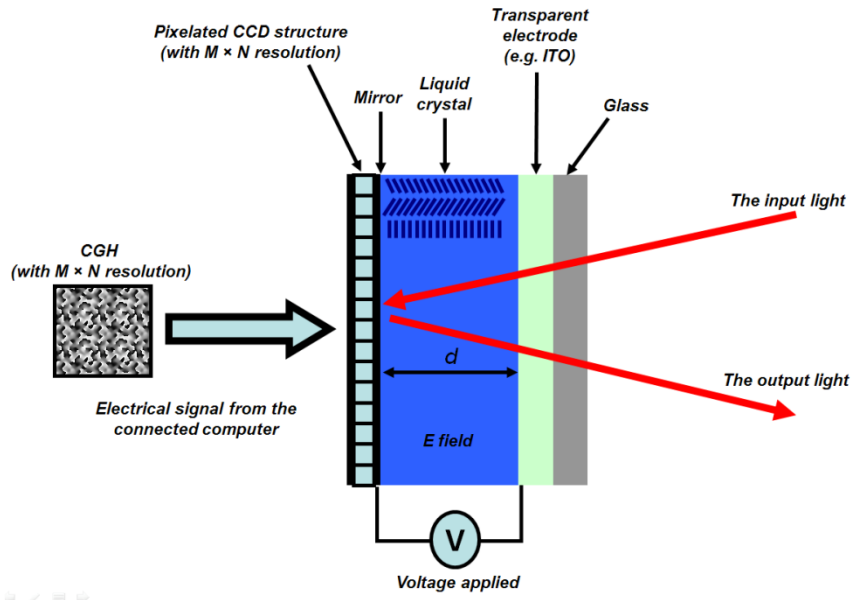

Fig. 2.12 *The basic structure of a SLM.[54]*

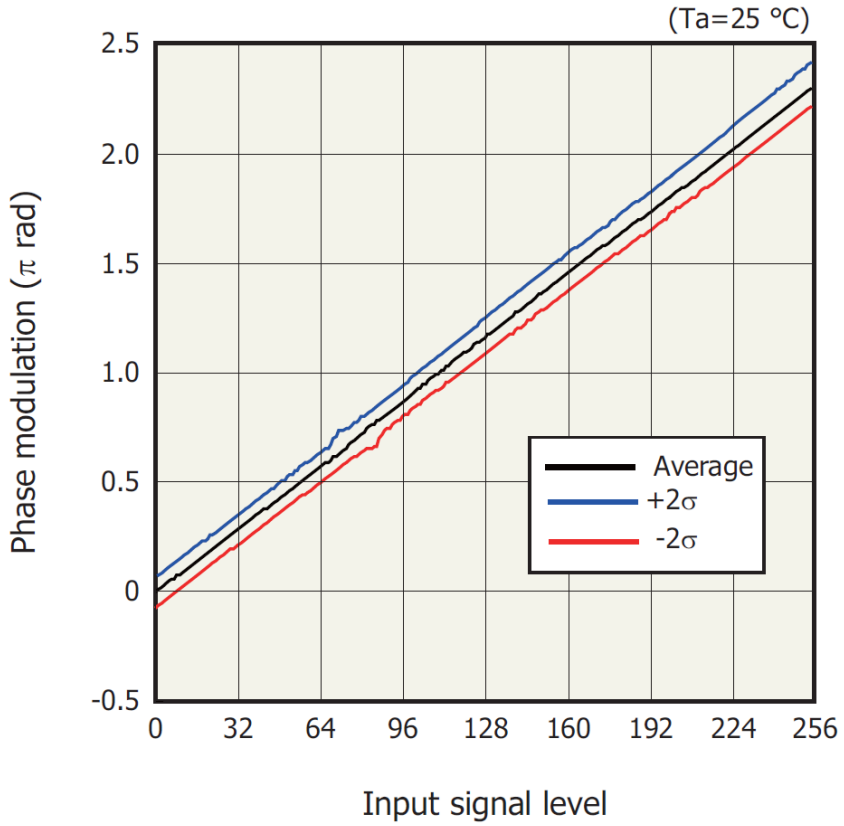

Fig. 2.13 *The measured results from a Hamamatsu X-10468 series SLM showing a near linear increase of the phase modulation with increasing the grey level (from 0 to 255).[55]*

With choice of optical configuration, the SLM offers the flexibility and capability in various applications, such as laser beam wavefront modification [56], polarization control [46,57], aberration correction [58] and optical pulse shaping [59].

In wavefront (phase only) modification method, the incident laser beam should be linearly polarized with the direction of electric vector parallel to the optical axis (director) of the liquid crystal. In this case, the relative phase between each pixel of the SLM shapes the wavefront of output beam without any polarization variation.

For polarization modulation, the incident beam is linearly polarized with its polarization direction at 45° to the director. In this orientation, due to the birefringence properties of the liquid crystal, this configuration leads to the output beam's polarization spatially controlled by each localized pixel of the SLM. By combining the SLM with certain waveplates, the linearly incident beam can also be converted to cylindrical vector beams.

2.5 Laser Induced Periodic Surface Structures (LIPSS)

When a focused laser beam irradiates on the material surface, by the a laser fluence near or just above the ablation threshold, Laser Induced Periodic Surface Structures, which are also called LIPSS, are produced. These kind of structures show self aligning formations similar to ripples on a water surface, which was firstly reported by Birnbaum [60] in 1965 on various semiconductor surfaces. Since then, further experimental studies [61-64] suggest that LIPSS are a universal phenomenon appearing for a wide range of wave length and pulse duration on a large variety of materials. These can be generated by multiple pulse exposure with a static beam, but also with a scanning beam (see Fig.2.14).

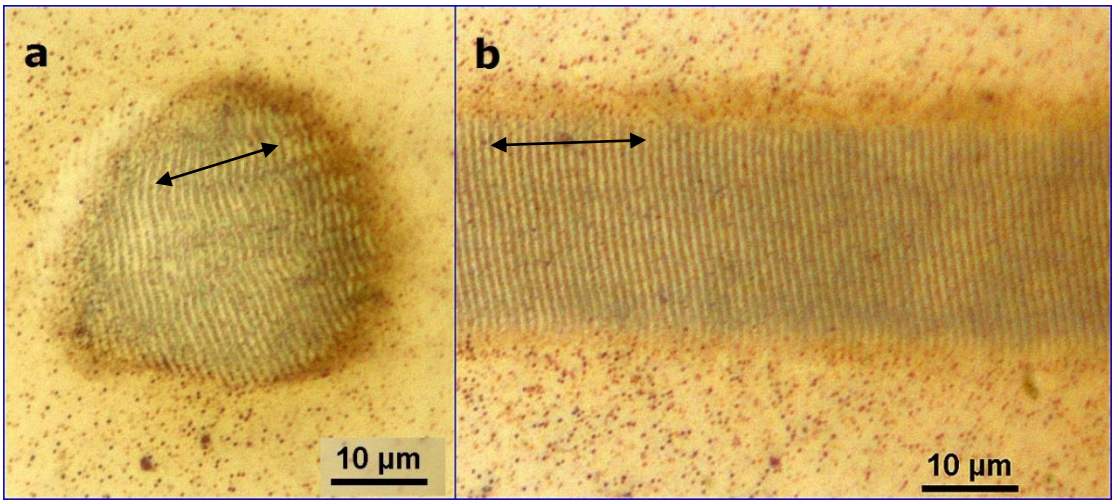

Fig. 2.14 *LIPSS formation by a) static spot, b) scanning beam from HighQ 10ps laser with 1064nm wavelength (black arrows indicated the polarization direction).*

The formation mechanism of this kind of ripple may be caused by modulation of the deposited energy due to interference at the material interface between laser beam and matter polarization associated with laser-induced surface excitation [65]. The surface is modified during the pulse, determined by the electromagnetic field interference patterns which are given by the so-called "general surface scattering" model. Here, the wavelength of ripples are predicted to be [66]:

$$\Lambda = \lambda / (n \pm sin\theta) \qquad \text{Eq.2.1}$$

where λ is the laser wavelength, n the refractive index of the irradiated material and θ is the incidence angle of laser beam. This prediction was tested experimentally and a good agreement between the theory and experiment was found. Although the underlying mechanism responsible for the ripples formation remains controversial, it

is widely accepted that the ripple orientation is dominated by the polarization state of the incident laser beam, which has been verified by experiments [67]. For linearly polarized laser beam, the classical ripples (with pitch ~ beam wavelength) orientation induced on material surface is perpendicular to the irradiation beam polarization. If the LIPSS induced by elliptically polarized laser beam, the ripple orientation is determined by the major axis of the polarization ellipse.

2.5.1 Application of LIPSS

The property of LIPSS microstructure on material surfaces can modify their micro or nano scale topographies. Hence, the generation of LIPSS in a single-process step provides a simple way of surface structuring toward a control of optical, mechanical, or chemical surface properties which can be used for various applications.

Colour effect due to the diffraction of light by periodic structures on metallic surfaces has already been shown [68,69]. LIPSS generated by ultrashort pulses produce coloured shapes on a metal surface by diffraction process, Dusser et al [70] used a half wave plate to mechanically encode linear polarization to reproduce a colourful image of the Dutch painter, Vincent van Gogh, scanned under white light. This was achieved by suitable colorimetric calibration when controlling polarization orientation of laser beam at each location. Thus control of the nanostructures with

laser surface processing can achieve a pre-defined picture as in Fig.2.15. The SEM images indicated the controlled nanostructures with two different orientations by orthogonally polarized laser beam.

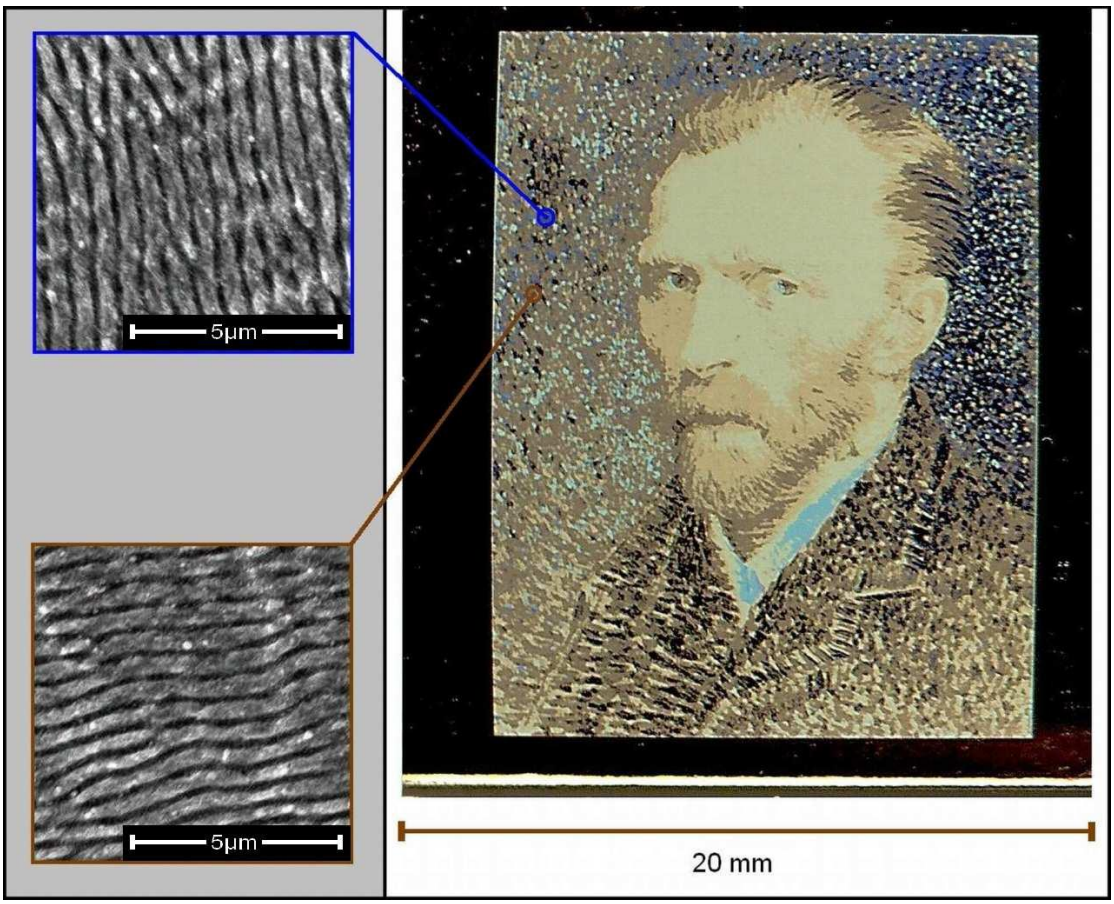

***Fig. 2.15**. Example of color effects obtained by controlled nanostructures with a femtosecond laser beam on a 316L stainless steel sample.[70]*

Beside the interesting structural colours, the induced surface structures on metals can also alter surface wettability. Jiangyou et al [71] used a ps laser to fabricate large area LIPSS on copper surface and the wettability of the surface was analyzed. With suitable combinations of the laser processing parameters, some of these ripples exhibited super hydrophobicity with a large contact angle up to 153.9 ± 3.2° (see

Fig.2.16). It has been shown that after laser irradiation treatment, the distinctive laser induced structure plays a significant role in the wetting behaviors. With this work, it shows a possibility to modify the wetting behavior of common engineering materials.

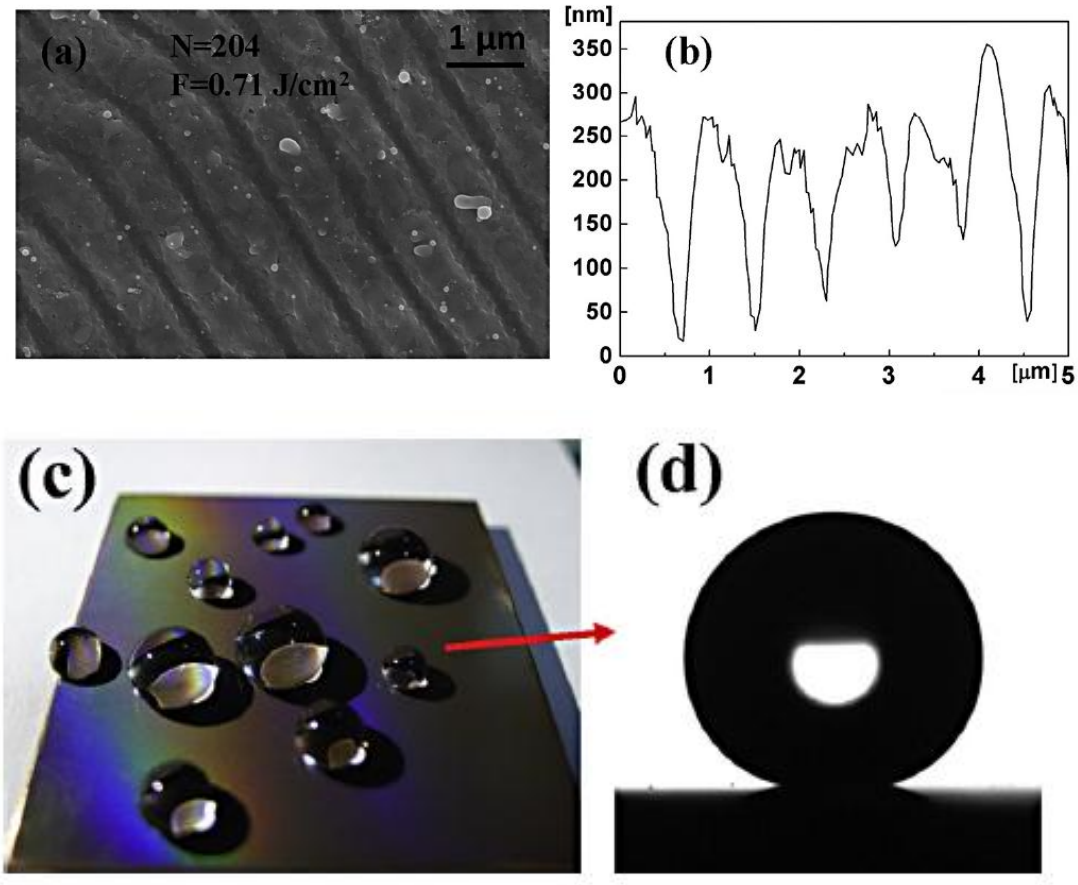

Fig. 2.16 *Water droplets on the processed copper surface with high contact angle. a) SEM micrograph of the laser irradiated copper surface; (b) the corresponding cross-sectional profile obtained by AFM measurement; c) and d) optical image of water droplets on the prepared sample.[71]*

Within the ripples structure of LIPSS, the contact surface area after laser treatment, is also increased which can be applied in energy storage devices. Storing and delivering power relies on the amount of the electrochemically active material that

can accumulate at the electrode/electrolyte. Recently, Alex et al [72] demonstrated the preparation of micro-structured nickel metal electrodes by using ultrashort pulse laser generated surface LIPSS. The electrochemical activity of the LIPPS nickel metal cathodes were investigated in aqueous KOH using cyclic voltammetry. The results of the voltammetry show that the formation of LIPPS yields a considerable enhancement in the electrochemical activity of the nickel surface (see Fig.2.17). It would be expected that maximising the accessible surface area of nickel cathodes would create a larger area for active material accumulation, leading to improved energy storage performance.

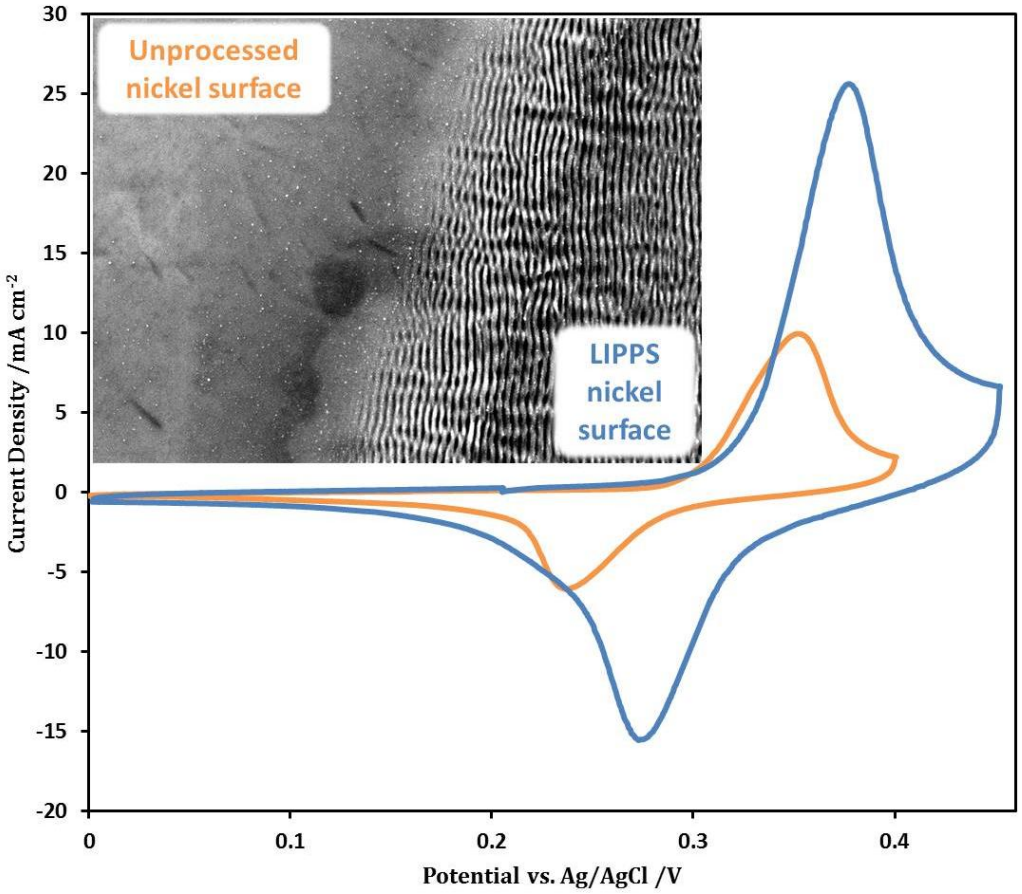

Fig. 2.17 *The surface of nickel metal foils was processed with the use of ultrashort pulse length, low energy laser pulses. Cyclic voltammetry shows increased electrochemical activity of these laser processed foils.[72]*

2.6 Introduction to laser drilling

One of the important and successful application of lasers, in industry has been in the field of laser drilling. Laser drilling emerges as a viable and successful substitute for holes less than 0.25mm in diameter that are otherwise difficult to drill mechanically [73]. It is now widely recognized that ultrashort laser pulses possess unique advantages than longer laser pulses in precision laser drilling, such as absence of plasma shielding effect, a well-defined ablation threshold, and a minimization of heat affected zones [74-78]. Industrial applications include the very precise drilling of holes for fuel-injection nozzles [36], the processing of silicon wafers [79], airfoil cooling holes in components of aircraft engines [80], or the precise machining of medical stent devices [13,32].

2.6.1 Laser drilling technique

There are four principal techniques for laser drilling: single-pulse, percussion, trepanning and helical drilling (see Fig.2.18). Single-pulse and percussion are simpler and faster drilling methods since they use only the focused laser beam for machining, without any further optics. The resulting hole is roughly the same diameter as the laser beam spot size. However they do not provide the best hole quality due to recast layer, tapering and bellow shape [73]. Trepanning and helical drilling offer moved laser beam interacting with the work-piece which produce holes

wider than the laser beam spot size. Trepanning is a standard technique for drilling large holes, e.g. 500μm, which would be considered as a percussion drilling process followed by a cutting procedure. The advantages of trepanning are the consistency and ability to drill shaped holes, which also reduces the hole's taper.

Helical drilling makes use of breaking up of the process into a multitude of ablation steps in order to enhance the accuracy. Compared with trepanning, the beam path of helical drilling is not limited to circular geometry, any shape can be formed by suitable optical scanning system or movement of the work piece. The laser pulses ablate the layers of material gradually so that the ablation front follows a helical path. The recast layers deposited on the side walls can be removed by successive passes of the beam, thus improving the end process quality. Although it is much more expensive and time consuming than other drilling methods, helical drilling satisfies the requirement of high accuracy and high machining quality [36]. It is also the only option for drilling holes with a very high aspect-ratio (i.e. > 10). The hole quality can also be further improved by using an assist gas during drilling to reduce oxidation, or by drilling at reduced atmospheric pressure to facilitate ablation and molten material ejection.

As a result, single-pulse drilling usually involves a large pulse energy and/or longer pulse duration, which is not a very accurate process. Percussion drilling involves

using a laser pulse train to gradually ablate deep holes. Trepanning consists of a percussion drilling, followed by a cutting procedure. Helical drilling usually involves low pulse energies and shorter pulses and produces the most accurate structures.

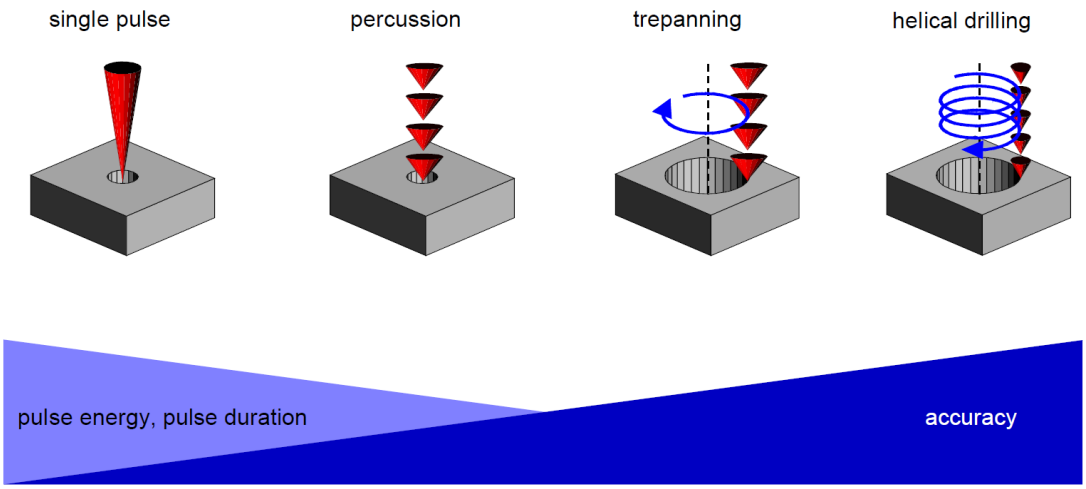

Fig. 2.18 *Schematic showing the four most common techniques for laser drilling.[36]*

2.6.2 Influence of parameters of laser drilling

For direct hole drilling, the quality of the laser beam, pulse duration, pulse repetition rate and polarization effect are all important parameters [73,81,82]. Yet many issues remain to be solved when high quality holes are to be drilled in various materials. These include cracks, large taper size, unsatisfactory shape etc.

2.6.2.1 Pulse duration

In general, when using long pulses (nanosecond time scale or above) for laser drilling, significant heat diffusion occurs during the pulse between the melting point and vaporization temperature after laser energy is coupled within the surface of the absorbing material [81]. This leads to create a large bulk of liquefied material during the processing, hence undesired growth of burr would emerge. On the contrary, when a pulse duration is shorter than 10 picoseconds, thermal diffusion into the surrounding material during the pulse is almost negligible, hence the melt depth can be minimize to much less than a micron and can be reduced to the nanometer level by decreasing the pulse duration to the fs timescale[36].

2.6.2.2 Repetition rate

When laser drilling at high repetition rate, with ultrashort pulses, particle shielding and heat accumulation determine the drilling efficiency and quality [82]. Particle shielding occurs when the time between subsequent pulses is so short that the deposited heat cannot diffuse out of the irradiated zone, which can be considered a "shield" resisting the pulse energy breakthrough, reduces the drilling efficiency. Particle shielding effect can be counteracted by the heat accumulation when using high pulse energy, but leads to poorer drilling quality caused by a tall rim on the hole's edge. These two effects would limit the useful range of process parameters and strongly depend on the size and geometry of the structures to be ablated.

2.6.2.3 Polarization effect

The influence of polarization on micro-drilling has been experimentally demonstrated in [4,51,83,84], showing that drilling high-aspect-ratio (depth/diameter) microscopic holes in metal with linear polarized ultrashort-pulse lasers produces anisotropic profiles. As the width of hole decreased with the material removal through the processing piece, p-polarized and s-polarized radiation, show different absorptivity due to the side wall angle (see Fig.2.19), resulting in changes to the hole's geometry and gradient. P-polarized radiation (parallel to the incident plane) was more absorbed by the hole side wall while much more s-polarized radiation(perpendicular to the incident plane) was reflected by the material[83]. This is expected from the Fresnel equations for angular dependence of reflectivity of a metal with polarization. This results in a distorted intensity profile, affecting the shape of the hole when the beam reaches the exit. For instance, when linearly polarized laser beam used in micro-drilling, there are two bulges located around the remaining circular shape.(see Fig.2.20) To solve this distorted shape of hole, a circularly polarized beam can be employed, averaging P and S components so that the absorption in each region is nearly equal. However ripple formation on the surface of the side wall by the distortion associated with circular polarization[84]. Besides this, the processing efficiency also needs to be considered when drilling at high-aspect-ratio microscopic features. In this case, neither circular nor linear polarized beam offers the desired result. To overcome these limitations, cylindrical

polarization in micro-drilling has been studied in recent years [1,4,51], and reported highest processing efficiency along with ideal quality of hole shape. Cylindrical polarization (radial/azimuthal) have been already described in Chapter 2.3(see Fig.2.8) These two CV beams result in temporally and spatially constant polarization state at the beam cross-section which allows direction independent movement during the processing [4].

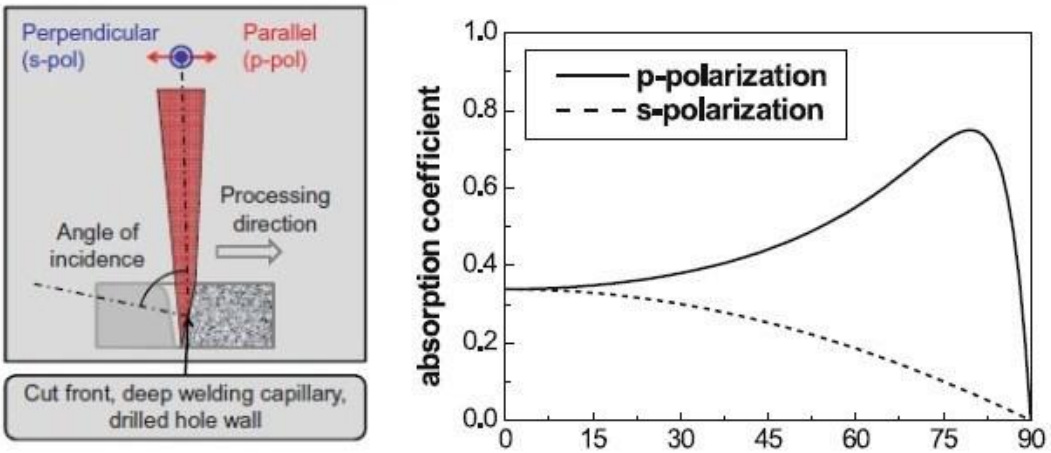

Fig. 2.19 *Schematic of p, s polarization and their absorption coefficient versus incident angle on mild steel.[4,51]*

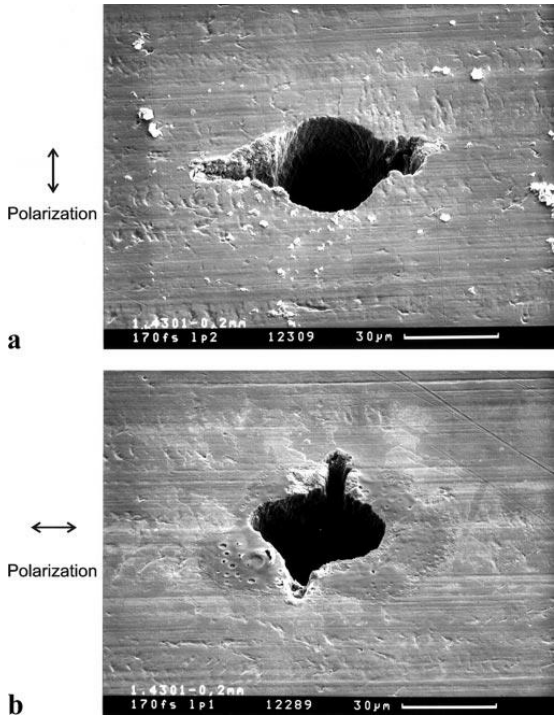

Fig. 2.20 *Geometry of exit holes during drilling showing the bulges orthogonal to the orientation of the linearly polarized laser light is a) vertical and b) horizontal.*

2.7 Introduction of laser beam shaping

Laser beam offer a highly directional and localized source of energy, which facilitates materials modifications at precise locations. Hence, the control and influence of laser beam shape, which defined as the irradiance distribution of the light when it arrives at the material of interest, is an important factor in materials processing [85].

Most lasers operate in the fundamental transverse electromagnetic mode of the cavity (TEM00), which is called as Gaussian beam mode, is the most common beam shape used in material processing (see in Fig2.21-a). As a unique property, it

remains a Gaussian shape throughout the beam path and when focused by a lens. The Gaussian beam of given diameter also has the lowest divergence, which allows for a small focused spot, which makes Gaussian beams ideal for micro-fabrication applications.

Top-hat beam are also widely used for materials processing applications (see in Fig2.21-b). Some optical elements are used as a beam shaper to transfer the Gaussian mode to Top-hat mode. However, an excimer laser can directly produce a Top-hat output with the appropriate cavity optics. With improved spatial uniformity, Top-hat beams are beneficial for specific processes, such as heat treatment in laser annealing [86], pulsed laser materials deposition [87] and welding applications with improved weld quality [88]. However, unlike with Gaussians, Top-hat beams (which have higher M^2) do not maintain their shape with propagation, only generating the uniform intensity distribution near the focal point or imaging location of the optical system.

Furthermore, there are several non-conventional beam shapes which give advantages over Gaussian or top-hat in some specific applications. For instance, Bessel beams (non-diffractive) are used in optical manipulation [89], which allowed the simultaneous trapping of several particles at the same time or the transport of 60μm microspheres over a distance of half a meter. In atom optics, Laguerre-Gaussian or

optical vortex light beams have been successfully used for atom guiding [90,91].

Bessel beam is defined as a beam whose electric field is explicitly described by a zero-order Bessel function of the first kind J_0 [92]

$$E(r,\phi,z) = A_0 \exp(ik_z z) J_0(k_r r) \qquad \text{Eq.2.2}$$

where r and ϕ are transverse and polar coordinates, z is the coordinate in the propagation direction, and k_z and k_r are the longitudinal and radial wave vectors. More generally, the term Bessel beam could refer to higher order functions although we ignore those here. Since the beam intensity is proportional to the square of the electric field for a Bessel beam,

$$I(r,\phi,z) \propto J_0^2(k_r r) \qquad \text{Eq.2.3}$$

this beam does not appear as a single spot, but rather as a series of concentric rings(see in Fig2.19-c).

When the Bessel beam in the far field, as the separation between the wave vectors increases, the beam intensity in the central axis decreases and eventually attains a null value. In this case, this beam can called as an annular beam, with

doughnut-shaped beam, is a beam with an intensity distribution concentrated in a ring with no on-axis intensity(see in Fig.2.19-d).

Annular beams can be generated by using apertures [93], an axicon or conical lens element [94], SLM based methods [95] and optical fibers [96]. In this current research, a SLM was used to generate the annular beam. An appropriate CGH can easily produce a phase pattern in an SLM that corresponds to a diffractive axicon, and as a result, the SLM will generate annular beams with user-defined wedge angles. Details will describe in Chapter 6.

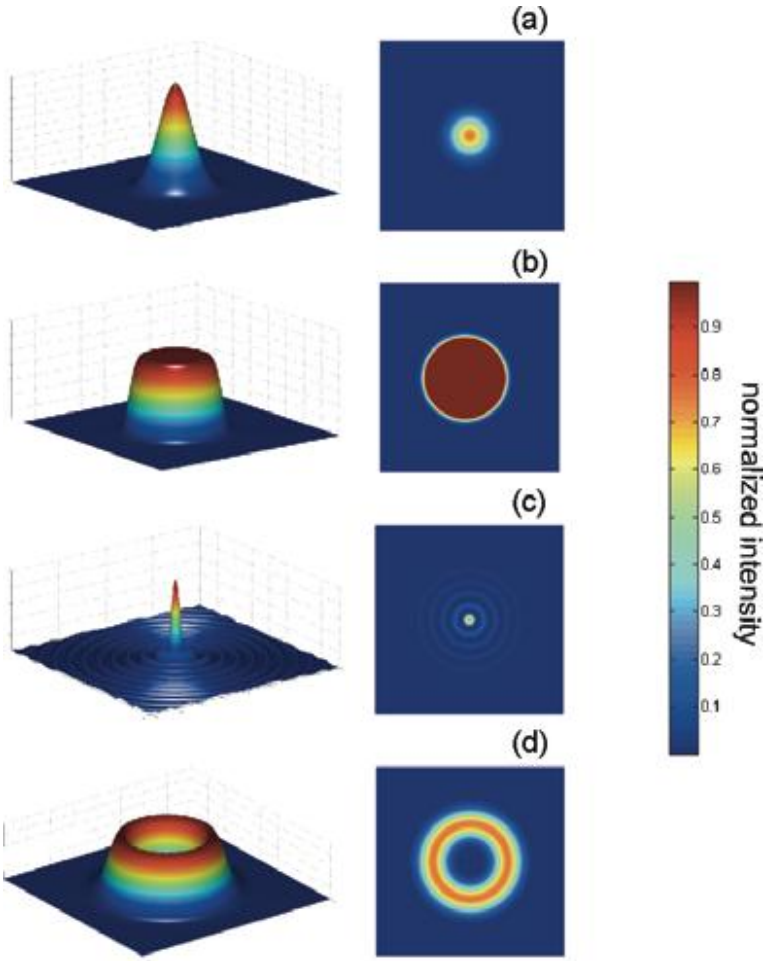

Fig. 2.21 *2D and 3D intensity distribution of a)Gaussian beam; b)Top-hat beam; c) Bessel beam; d) annular beam.[92]*

A related structure to the annular beam is the so-called optical vortex (OV) beam. An OV beam, which carries a orbital angular momentum(OAM), is defined as a beam whose phase varies azimuthally along the direction of propagation. OV's are characterized by their topological charge (*m*), which corresponds to the number of twists in the phase front within one wavelength. Due to the twisting of the phase front, the phase in the beam center is multiply defined, giving rise to an optical singularity that produces a vanishing amplitude at this point [97] giving the appearance of an annulus in intensity.

It is important to note that the literature tends to take a general view to the term "annular beam" and uses it to refer to any beam with a null intensity along the beam axis. In this research we define the annular beam specifically for beam generate by axicon phase CGH.(detailed in Chapter 6)

Chapter 3 Experimental equipment

3.1 High-Q picoseconds laser system

In this present research work, we used the custom designed Nd:VAN seeded regenerative amplifier laser system (HighQ IC-355-800) supplied by HighQ laser GmbH[28]. It is a Class IV laser running at up to 50kHz repetition rate with output wavelengths at 1064nm, 532nm, and 355nm, with pulse duration $\tau \approx 10$ ps and maximum average power at 2W. It is an extremely compact and easy to use laser system, which is principally comprised by three parts: laser head, laser controller and closed cycle water-to-air cooling system.(see Fig.3.1)

As temporal pulse length is 10ps, and maximum pulse energy $E_p \leq 200\mu J$, complicated chirped-pulse amplification (CPA) is not required in this laser system. Based on the direct diode pumping, without any manipulation of pulse duration, the laser system is stable and reliable. As shown in Fig.3.2, the laser head contains the following subcomponents: a seed laser, a regenerative amplifier, a pulse picker and the follow-up optical path for the output laser beam. The mode-locked seed oscillator initially generates 10 ps pulses at MHz level repetition rate with diode pumping; then the pulses train are injected into the regenerative amplifier through the Faraday isolator; after that the amplified pulses can be selected by the pulse picker. Moreover, the fundamental output wavelength of 1064nm can be frequency-doubled and tripled by properly adjusting the relevant half wave plate (HWP), generating 532nm and 355nm output, respectively. The system is remotely controlled

by the computer software which can alter the laser output parameters by mouse clicks and drags (see Fig.3.3). Moreover, the system can be externally controlled by a TTL signal for the laser gating, which allows the option for high level synchronization during laser processing.

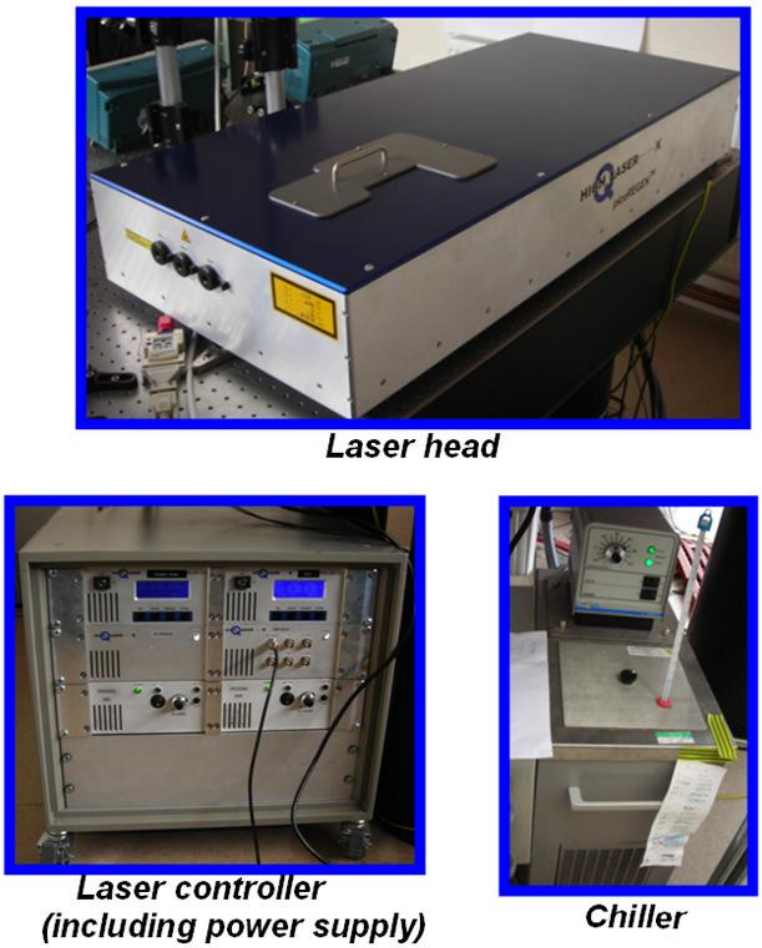

Fig. 3.1 *high-Q IC-355-800 picosecond laser system layout.*

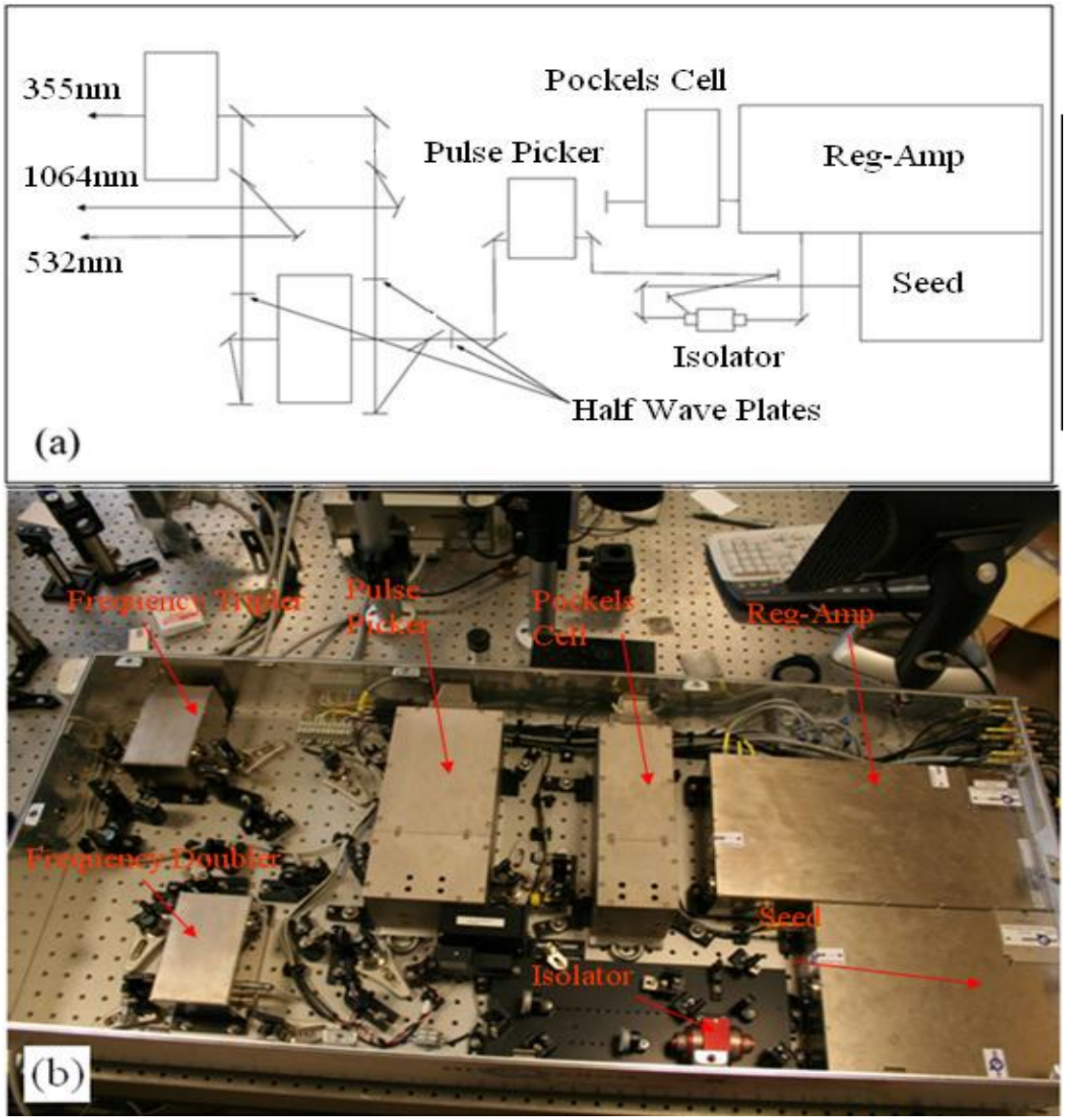

Fig. 3.2 *(a) Schematic of the optical setup inside laser head and (b) The corresponding image of laser head internals.*

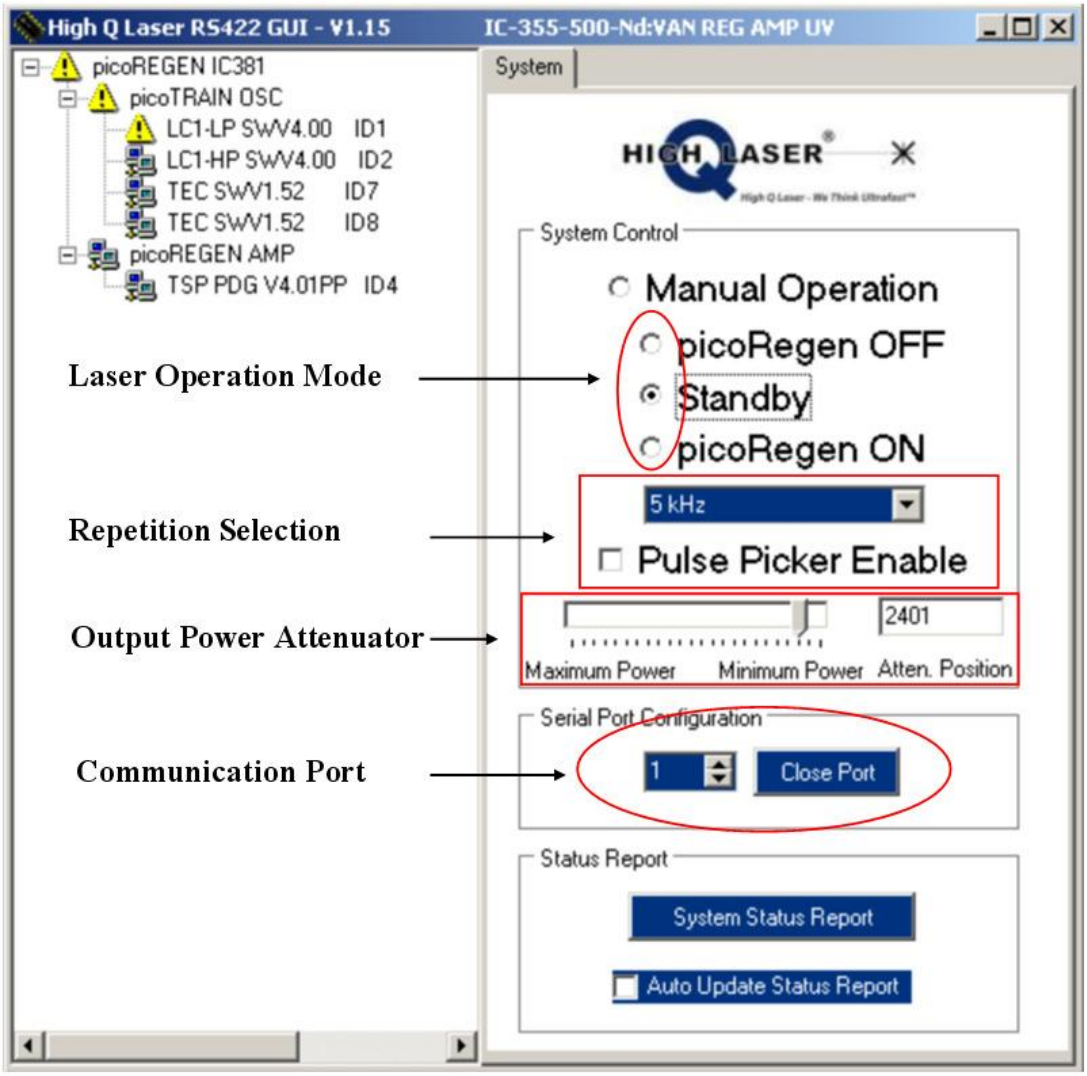

Fig. 3.3 *Graphical user interface (GUI) for the HighQ laser.*

3.2 Spatial Light Modulator (SLM)

A Hamamatsu Photonics phase only spatial light modulator (X10468-03) was used in this experimental work (see Fig.3.4). It is based on a pixelated liquid crystal device whose mechanism has been described in Chapter 2, with a dielectric coating providing > 95% reflectivity on the backplane for laser wavelength at 1064nm and resolution of 800x600 pixels (each pixel equals 20μm, which gives an incident window size of 16x12 mm).

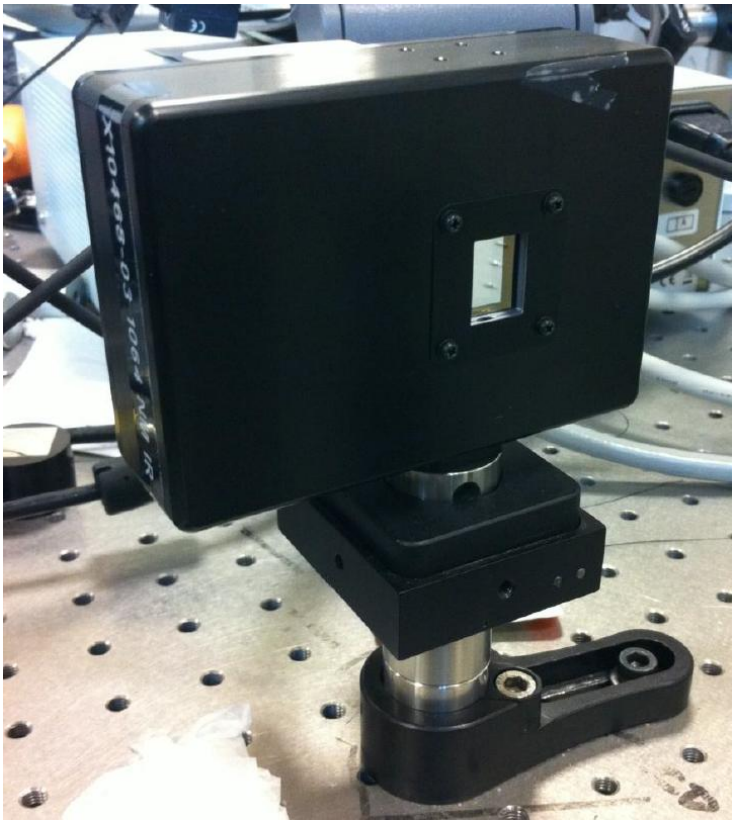

Fig. 3.4 *SLM in optical path, beam is directed onto the LCD where user defined CGHs are displayed.*

The X10468-03 is a parallel aligned nematic crystal device, in which the LC molecules are aligned vertically along the optical axis, hence causing a phase change to the light polarized along the molecular axis (director) , but leaving the light polarization perpendicular to the director completely unaffected.

The SLM is attached to a controller unit and connected with a computer, the liquid crystal display (LCD) acts as a secondary monitor screen of the computer. Using the software provide by Hamamatsu, different computer generated holograms (CGH) can be loaded on the LCD by applying a discrete voltage to individual pixels, each voltage corresponding to a given grey level.

3.3 S-waveplate

S-waveplate (RPC-1030-10-109, with operation wavelength at 1030 ± 35nm, manufactured from Altechna) is a space variant polarization converter based on the nano-structuring imprint inside a fused silica substrate, which converts incident Linear to Radial or Azimuthal polarization.(see Fig.3.5) The principle of the S-waveplate was described in Chapter 2. For optical configuration, one aligns the center of the S-waveplate with the optic axis of the incident laser beam and then rotate the alignment mark on the substrate, parallel to incident linear polarization orientation. In this case, the output will be radially polarized. If the incident linear polarization is perpendicular to the alignment mark, the output will be azimuthally polarized.

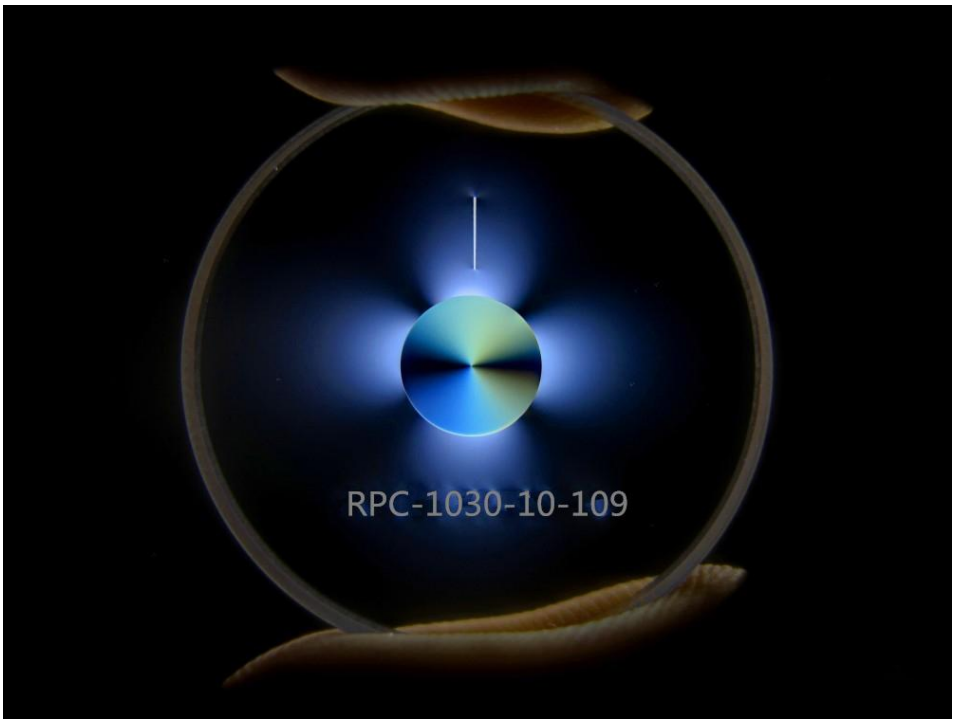

Fig. 3.5 *S-waveplate (Altechna) used to convert incident linear polarization to Radial and Azimuthal polarizations.*

3.4 Scanning Galvanometer system and multi-axis motion control system

The Galvanometer scanning head used in the experimental work (Nutfield XLR8-10) was employed to scan the laser beam at the test sample, mounted on the stage and focused by a flat field f-theta lens. Fig.3.6 shows the schematic of Galvanometer working principle, the system consists of 2 galvanometer scanners (X and Y), a flat field f-theta lens (focal length f=100mm) and integrated driver electronics all enclosed in a black metallic scan head.

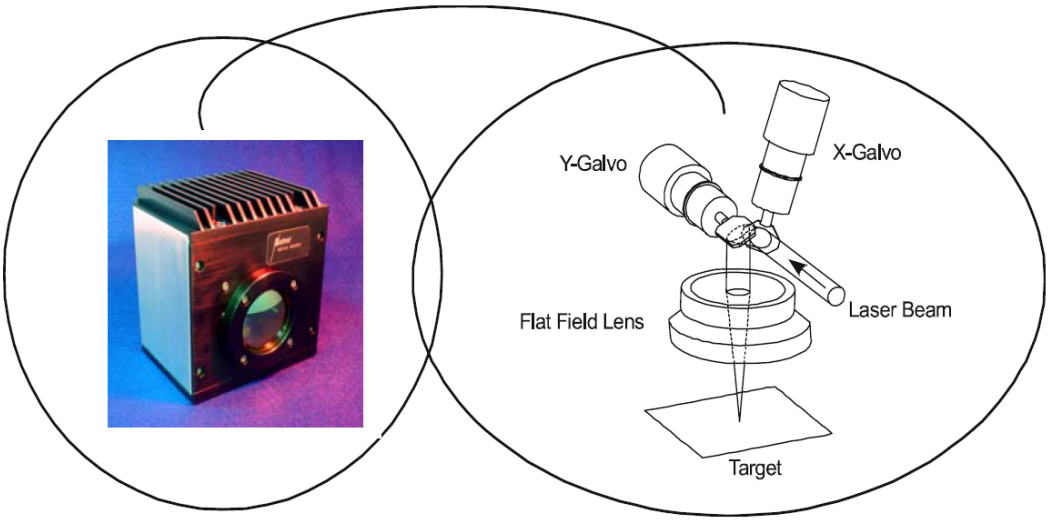

Fig. 3.6 *Schematic of Nutfield XLR8-10 scanning head working principle.[98]*

Two dielectric mirrors (operating wavelength at 1064nm) attached on the galvanometers provides the capability of deflecting optical beams in an X/Y configuration for a range of laser applications. The synchronized actions of the two galvanometer servo-controlled turning mirrors directs the laser beam to specific

locations on the target material surface in both the X and Y directions through the flat field lens producing an agile micro-machining system. The galvanometer can scan up to 10^4mm/s, with a resolution < 4μm over a 60 x 60mm maximum scan field. For this model there are no edge effects inside the working field because the laser beam is always nearly perpendicular to the substrate top surface.

The Galvanometer system was controlled by the SCAPS-SAMlight software having a user friendly interface. In the grid area, various geometrical shapes and texts can be created or loaded from other files. The laser micro-structuring parameters such as traverse speed, number of repeat scans, hatch spacing and hatch type can be specified in this software (see Fig.3.7).

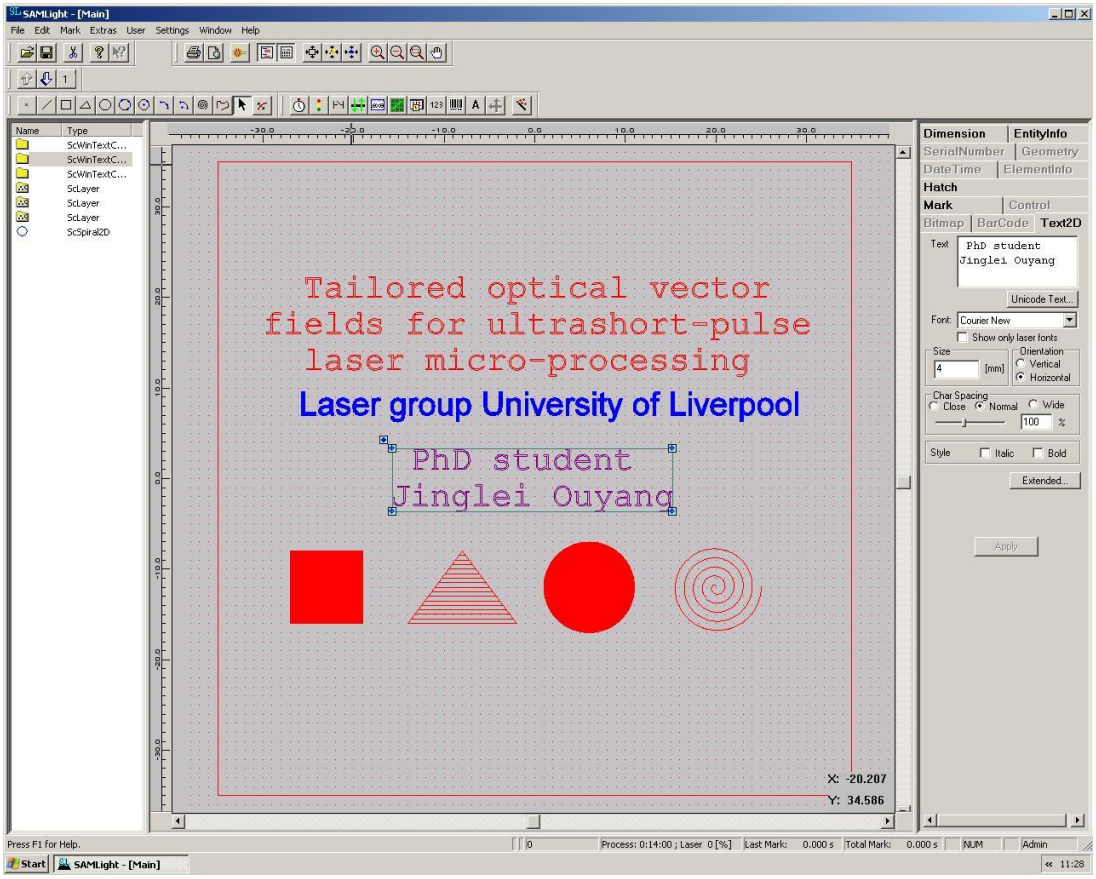

Fig. 3.7 *User interface of SCAPS- SAMLight scanning software.*

In industrial processes, much larger machining fields are often required. For this situation, the edge effect can be avoided by integrating the scanning head's action with motion control of the stage system. This is implemented by moving the high resolution stage instead of scanning out of the working field.

To ensure high precision motion control, we used Aerotech stages (A3200 series) and Nview HMI programming interface. The Aerotech stage can provide high accuracy 5 axis movement (X-Y-Z three dimensional movement plus the goniometers with angles tilted in U and V) with a resolution of 0.5μm in all

directions (see Fig.3.8). The working range of the stage gains 100x100mm in X,Y axis and 15mm in Z axis, with maximum speed 500mm/s.

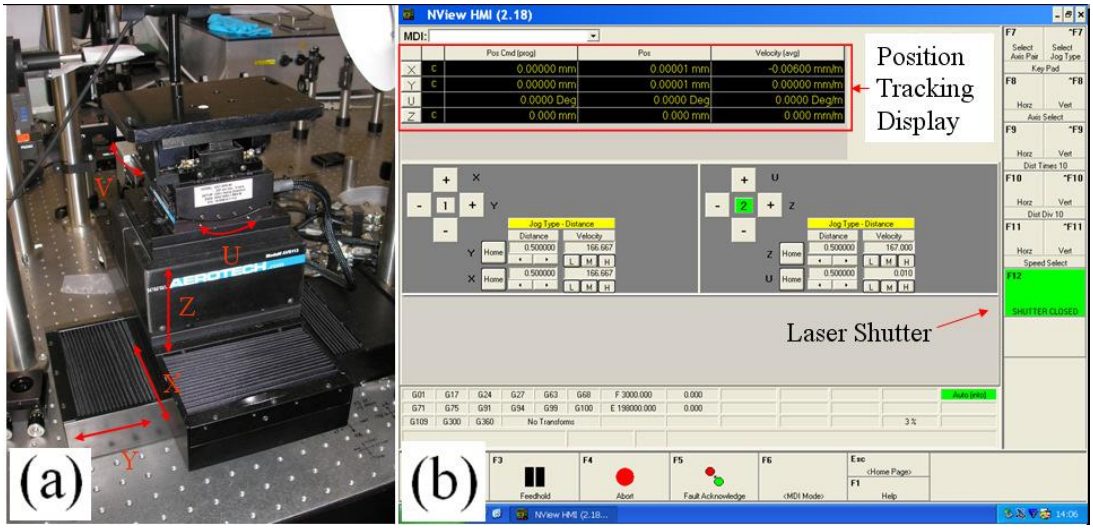

Fig. 3.8 *a) Aerotech 5 axis stage and (b) Windows graphical user interface (GUI).*

This CNC stage was controlled by the Npaq driver and Nview GUI. Commands were either entered directly into the software using the Nview programming interface or loaded from any other CNC language. Movement of the stage can be defined in two ways, as either absolute co-ordinates (with respect to the table origin) or as relative co-ordinates (with respect to the last position); this allows for both independent and directed axis movement. In addition it was possible to define values for the traverse speed and vector speed (directed movement), acceleration and deceleration and shutter control.

3.5 Analysis equipment

3.5.1 Spiricon beam profiler

The laser beam profile can significantly affect the micromachining quality. In this study, a Spiricon beam profiler (Model LBA-300,working wavelength window:190nm-1100nm) was used to investigate the laser beam profile, both near and far field. This LBA-PC beam profiler system consists of the following equipment: a Spiricon LBA-PC frame grabber card, with software; a CCD camera mounted on a laser beam sampler holding wedged fused silica pick-off and OD filters for signal attenuation (see Fig.3.9). It provides all the essential features needed for laser beam analysis. Some of these features are: high speed high resolution false colour beam intensity profile displays in both *2D* and *3D*; numerical beam profile analysis employing advanced proprietary calibration systems; both whole beam and linear Gaussian fits to beam data; signal to noise ratio improvement through averaging and background subtraction with statistical analysis of all measured parameters. The detector area is 8x6 mm with a pixel spacing of 9.9x9.9 μm. Some settings, such as camera gain, camera blooming effect and laser beam attenuation, may affect overall accuracy. With all these parameters optimized, an accuracy of ±2% can be obtained.

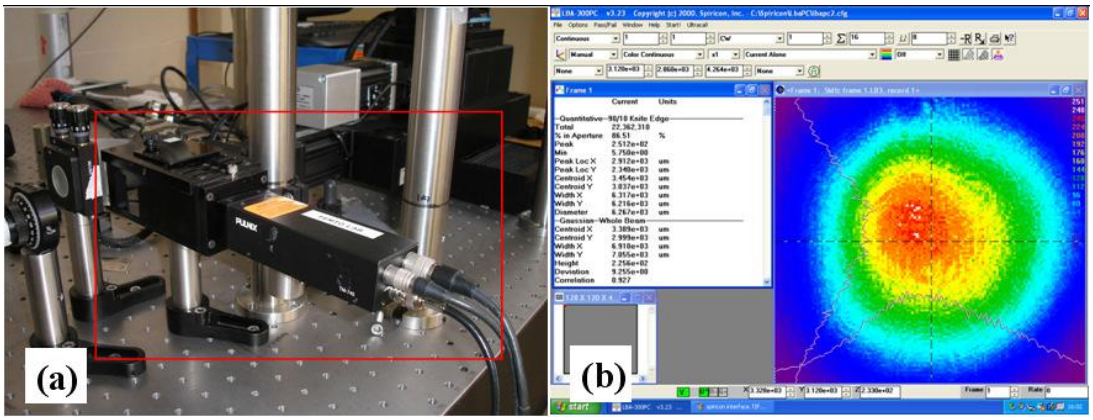

Fig. 3.9 *Spiricon laser beam analyser system (left) and user interface of LBA-300 sofware (right) with observed intensity profile from the HighQ laser system.*

3.5.2 Microscope system

In this experimental work, most of the micro-machined features on the samples are on the micron scale. The Leitz Wetzlar optical microscope attached with a Nikon digital camera (DS-U2) provides 2D images of the surface condition before and after treatment with the laser. The microscope has several available magnifications to allow detailed inspection of the surface pre and post processing; these objective lenses were: x5 (NA=0.1), x10 (NA=0.25) , x20 (NA=0.4), x50 (NA=0.75) and ×100 (NA=0.9) (see Fig.3.10).

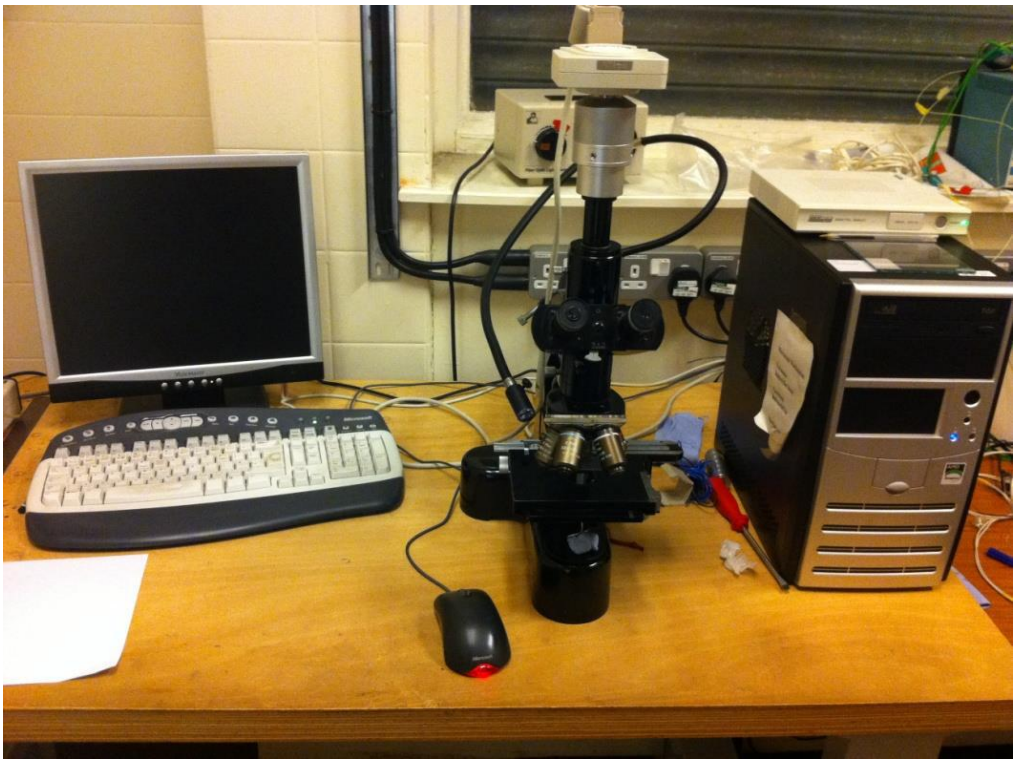

Fig. 3.10 *Nikon microscopy system showing the microscope objectives. images are taken through the top down camera and transferred to the PC Software.*

The optical microscopy setup comprises three parts: optical microscope, digital camera and Nikon post processing software. The use of a conventional microscope allows the user to observe the surface by adjusting the focus and light to the required conditions; then by switching to the Nikon software the user is able to operate the digital camera to capture, save images and make basic measurements in the XY plane (see Fig.3.11). It is calibrated regularly by measuring the company provided standard samples.

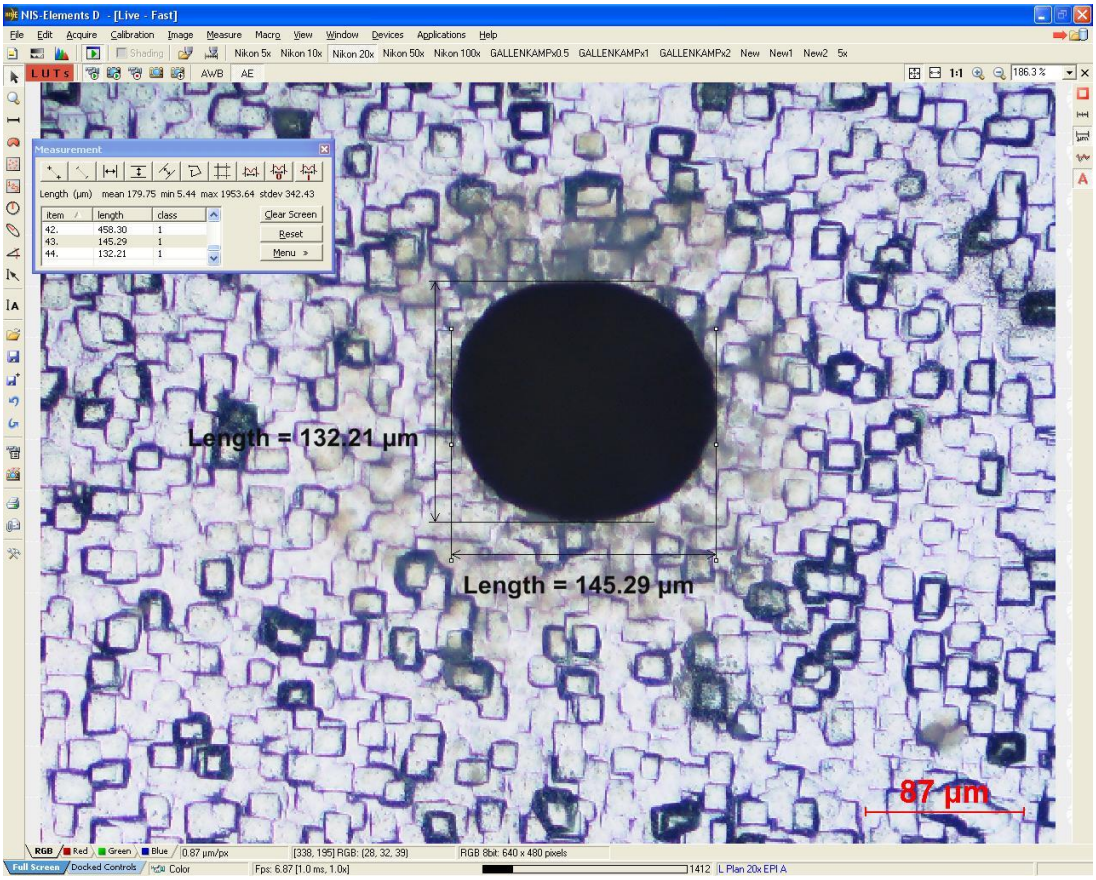

Fig. 3.11 *User interface of Nikon camera software.*

3.5.3 WYKO NT1100 white light interferometric microscope

The Nikon digital microscope can only obtain 2D information, hence, a WYKO NT1100 interferometric microscope was employed to achieve the surface topography in three dimensions. It is a non-contact optical profiler which provides the XY plane with ~ 0.5 micron level resolution and vertical, Z resolution of a few nanometres. This microscope connect with an advanced computer software, which offers an analysis package, allows dissection and formatting the measured surface data (see Fig.3.12).

Fig. 3.12 *WYKO NT1100 interferometric microscope.*

Fig.3.13 gives its working schematic, a white light beam is passed through a beam splitter, half of the beam is delivered to a reference surface and other half to the test surface; the reflected light from both surface recombine to form interference fringes. Due to the short coherence length of white light, interference pattern can only be observed over a very shallow depth of field for each focus position. The microscope objective scans vertically downward recording the interferograms at varying heights on the test surface. The analysis package uses the computing algorithms to demodulate the envelop of the fringes and extract vertical position corresponding to the peak fringe signal for each point on the test surface, hence a completely 3D surface morphology is obtained.

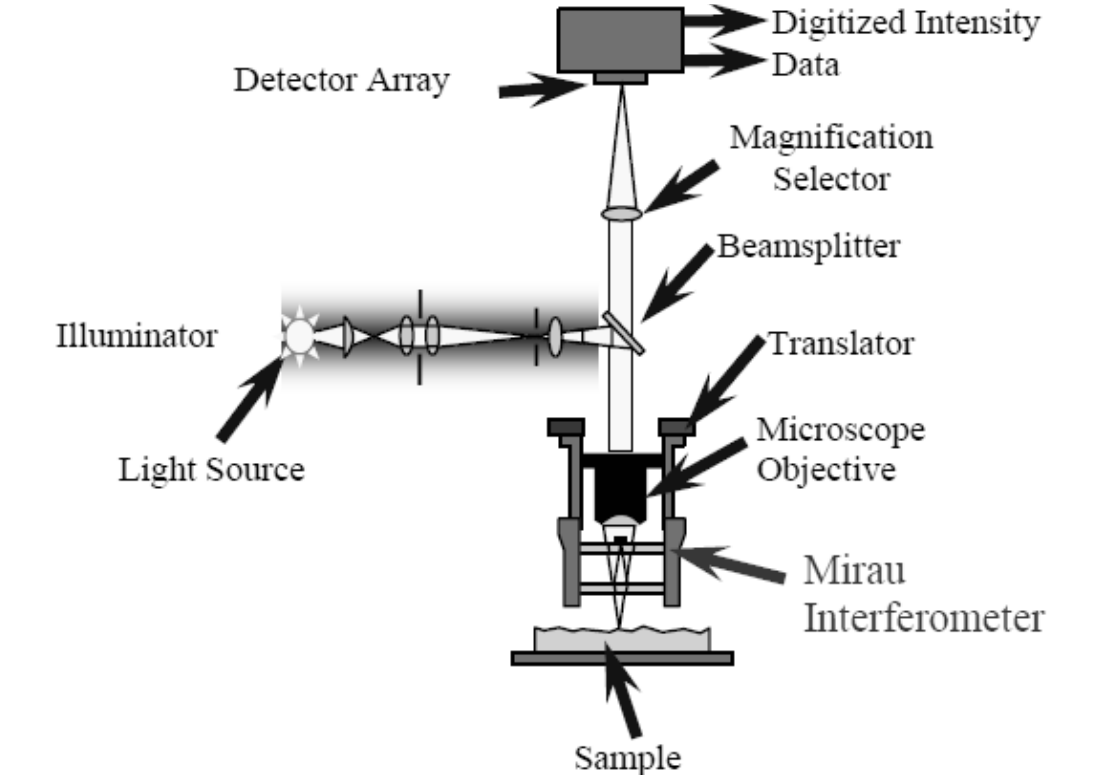

Fig. 3.13 *Optical schematic of WYKO interference microscope used for measurement of fine surface structure.*

When doing a measurement, the sample was put on the stage. By tuning the height of the stage, interference fringes could be seen from the screen when sample surface was in the focus position. After that, by executing scan action the sample surface could be measured accurately. The software provides powerful measurement and analysis capabilities, including surface height statistics. The system is calibrated at periodic intervals by measuring against a standard sample provided with the microscope.

3.5.4 Scanning Electron Microscope(SEM)

A Jeol (JSM 6610) scanning electron microscope (SEM) was utilized to provide detailed surface images at high magnification up to ×300k.(see Fig.3.14) The accelerating voltage of this system can be varied between 0.3 – 30kV. The specimen stage was a 5-axis eccentric goniometer with a maximum displacement of X = 125mm, Y = 100mm, Z = 80mm, T = -10 – 90°(tilt) and R = 360° (rotation). Samples were placed into a chamber before being evacuated to low pressure; dielectric samples were taped to the sample holder using conductive tape to prevent surface charging. An infrared miniscope attached to the side enabled viewing of the sample whilst under high vacuum. Image was captured by the software package, manual or automatic adjustment of the image focus, contrast, magnification and illumination was possible. Attached externally to the Jeol SEM was an Inca X-act EDX (Oxford instruments) analyzer; the EDX detector converts the energy of individual x-rays into voltage signals of proportionate size. Results were subsequently displayed using proprietary software as a series of peaks, which using the inbuilt material library, can identify individual elements by x-ray energy.

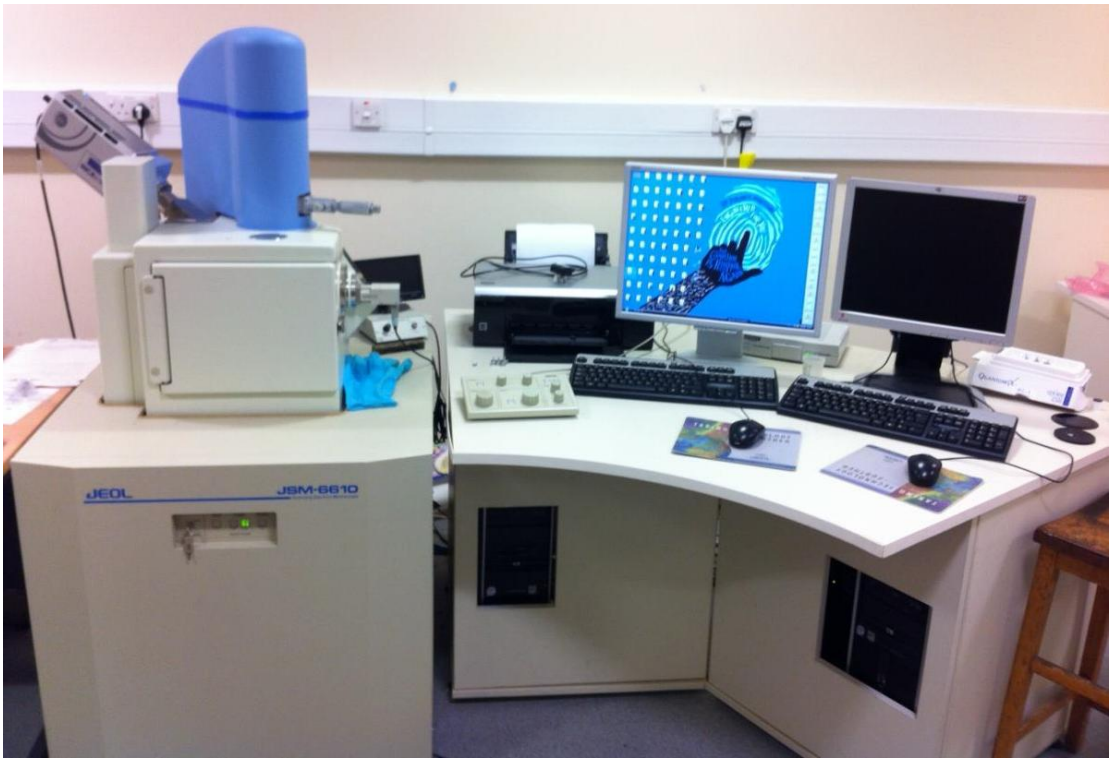

Fig. 3.14 *Layout of Jeol JSM6610 SEM.*

Chapter 4 Generation of complex cylindrical vector beams and application to picosecond laser surface processing

4.1 Introduction

Laser beams with a space-variant electric field orientation and amplitude are referred to as Cylindrical vector beams [99] and have great potential for furthering theoretical understanding of light waves and light-material interactions. Radial and azimuthal polarization states are extreme examples of these vector states and can be produced with specific laser cavity designs [100], a Spatial Light Modulator (SLM) [46] or nano-structured waveplates [47]. Pure radial and azimuthal polarizations have a Laguerre Gaussian (LG) ring intensity distribution with a polarization singularity at the centre while pure vortex beams with any given polarization have a LG intensity distribution with a phase singularity. The use of vector beams has resulted in advances in applications such as microscopy [101], optical trapping [49] and ultrarelativistic electron acceleration [102]. Since the z-component of a vector beam is negligible when focusing with low NA optics, 2D vector fields result in a fixed plane, orthogonal to the beam k-vector. A recent study on femtosecond laser induced LIPSS structuring on Silicon using optical vortex beams by K K Anoop et al [103] created with a liquid crystal q-plate showed a developing radial micro-structure, highlighting the multi-pulse feedback mechanism responsible for plasmon structuring. Also, the central zero intensity singularity expected of a Laguerre Gaussian (LG) ring intensity mode was decorated with nano-particles. In addition, K. Lou et al [104], using femtosecond laser vector fields, generated 2D near wavelength micro-structures on a thin copper film on fused silica substrate.

Here, an SLM was combined with an interferometric technique to add a spiral phase and variable phase shift φ_0 which controlled the detailed vector fields and hence LIPPS structuring. Previously, Yang et al [46], using two Spatial Light Modulators demonstrated the ability to dynamically modulate radial and azimuthal polarization states in real time along with linearly polarized LG intensity profiles with a 532nm wavelength picosecond laser, synchronized to the motion control system. The resulting low frequency surface micro-structure LIPSS and patterns with pitch Λ ~0.5 μm confirmed the purity of the desired 2D vector fields for surface patterning.

In this chapter, complex 2D vector fields was demostrated, generated by combining a phase only SLM and nano-structured S-waveplate with a NIR picosecond laser source to machine surface micro-patterns via plasmon structuring which highlights the orthogonal local electric field structure [105,106]. OAM was then added with a helical phase applied to the SLM. As the near field beam intensity profiles are Laguerre Gaussian due to the phase/polarization singularities, detailed polarization analysis of vector beams with and without Orbital Angular Momentum (OAM) are analyzed around the focal point of a lens (far field) by translating a detector consisting of a polarizer and CCD camera. This clarifies the effect of a vortex phase on the propagating vector fields which induces a clear rotation of the vector field around the lens focal plane and further supported by the observed Plasmon structuring.

Also, by altering linear polarization direction incident on the S-waveplate, complex surface patterning was extended to a new level, creating remarkable logarithmic spiral LIPPS which result from the field generated by a superposition of radial and azimuthal polarizations. Logarithmic spirals (first described by Descartes and admired by Bernoulli) often appear in nature, for example, the spiral arms of galaxies, [107], the cloud formations observed from space in a cyclone and spiral patterns in shells.

While more complex vector fields have been impressed on low power Gaussian beams with 633nm [108] and 532nm [109] sources, the application to high power picosecond laser surface plasmon structuring has been more limited and thus of great interest in the search for precise surface patterning with a high degree of complexity.

4.2 Three-dimensional investigation of cylindrical vector beam focal fields

4.2.1 Aim of the experiment

This experiment tried to investigate the tailoring of vector beams to shape the focal fields. Polarization analyzed intensity profiles were used to detect the vector beams with or without OAM focusing property, while laser induced plasmon structuring help to visualize the vector fields in the focal region.

4.2.2 Experimenal details

The experimental setup is shown in Fig.4.1. A seeded ultrafast laser Regenerative amplifier (High-Q IC-355-800, Photonic Solutions) has a 10ps temporal pulse width, 1064nm wavelength, M^2 <1.3, 50kHz repetition rate and horizontal linear polarization output. The laser beam is expanded with a x3 telescope (CVI) to a diameter of 6mm, passes through an attenuator ($\lambda/2$ plate and Glan-laser polarizer with transmission axis horizontal), beam vector fields structured using a reflective phase only SLM (Hamamatsu X10468-03) and an uncoated fused silica S-waveplate (Altechna). With the SLM used as a mirror (fixed phase), and with incident linear polarization, radial and azimuthal states were created by rotating the S waveplate axis to $\theta = 0$ and $\pm$ 90° respectively while superposition vector fields could be generated when the waveplate was set in the range -90° < θ < +90°. OAM was

added by applying a spiral phase (topological charge m =1), Computer Generated Hologram (CGH) to the SLM(see Fig.4.1 CGH pattern attached next to the SLM). A 4-f correlator system [120] (Lens 1 and 2 in Fig.4.1, $f_1 = f_2 = 300$mm) re-images the resulting beam vector fields into the 10mm input aperture of a scanning galvo (Nutfield XLR8-10) and focused with a flat field f-theta lens (f = 100mm). Polished stainless steel samples, mounted on a precision 5-axis (x, y, z, A, U) motion control system (A3200 Npaq system, Aerotech) were carefully positioned around focal field of the lens.

Also, by having a 45° flip mirror, the transmitted radiation through lens L1 (f=300mm) was re-directed to the Spiricon camera via a wedged fused silica beam splitter (45°) which acted as a polarization analyzer since the first surface was close to the Brewster angle. The reflected beam is therefore vertically polarized. Translation of the camera along the optic axis near the focal plane of lens L1 allowed spatial polarization analysis along the z-axis. This allowed measurement of the vector fields confirming the effect (or otherwise) of OAM on both polarization and intensity, prior to surface micro-structuring with the f-theta lens.

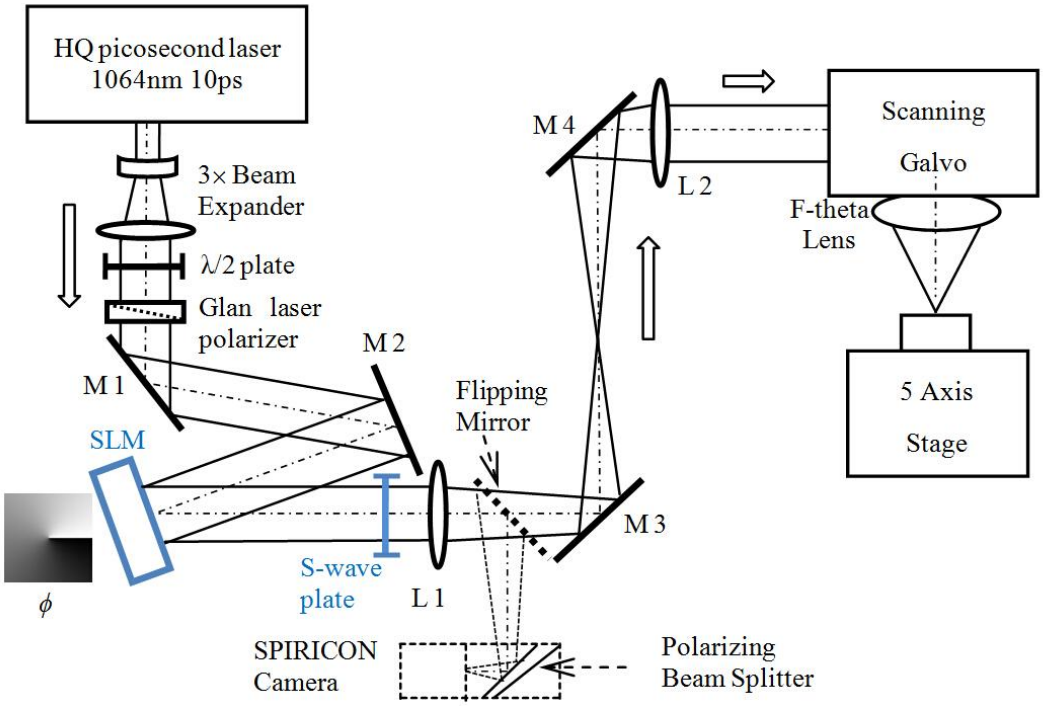

Fig. 4.1 *Experimental set up of High-Q picosecond laser micro-processing system.*

In the experiments, a number of beam vector field configurations are produced by tilting the S-waveplate optical axis to various angles. Henceforth, vector beams with a radial, an azimuthal, or an intermediate tilted polarization (see Fig.4.2) are referred to as RP, AP and IP beams respectively. A circularly polarized beam is also used in some of the experiments, produced by replacing the S-waveplate with a quarter-waveplate with its fast axis tilted to 45˚. This is referred to as CP beam henceforth. For comparison purposes, an orbital angular momentum is then added to all these beams by using the SLM to induce an optical vortex phase wavefront with a topological charge value of m=1, with the waveplate configured as before. Henceforth, the radially, azimuthally, intermediately and circularly polarized beams with an orbital angular momentum are referred to as RPOAM, APOAM, IPOAM

and CPOAM respectively. For each vector field configuration, the collimated near field beam (without focusing by Lens 1 in Fig.4.1) is analysed by placing the polarizing filter and SPIRICON profiler (dotted components in Fig. 1) ~300mm after the waveplate. The resulting collimated beam intensity profiles are show in Fig.4.2. In all cases, the polarization purity was ~95%.(measured by rotating a polarizing filter and recording the maximum and minimum transmitted power) In theory, the beam intensity profiles of CV beams with vortex wavefront added (Fig.4.2 d-f) should be the same with the one with planer wavefront (Fig.4.2 a-c), which means OAM did not affect the intensity distribution in the near field. The twist lobes showing in Fig.4.2 (d)-(f) may caused by the distortion from SLM.

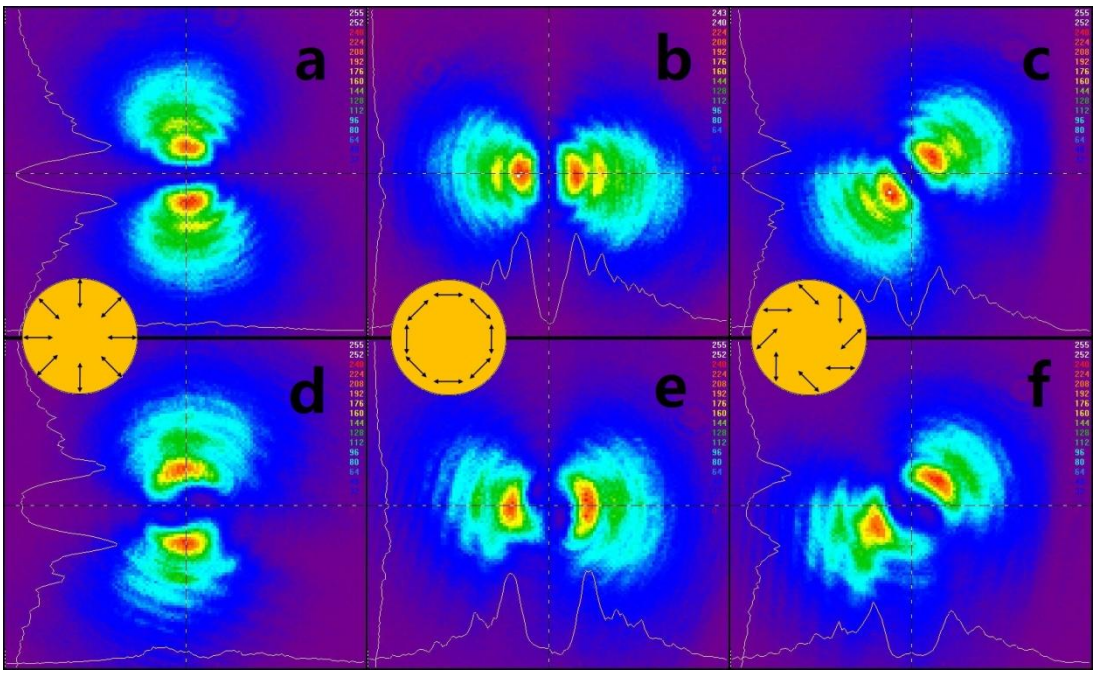

Fig. 4.2 *Collimated beam profiles: (a) RP beam. (b) AP beam. (c) IP beam, with polarization vectors tilted at 45˚. (d) RPOAM beam. (e) APOAM beam. (f) IPOAM beam. Intensity in arbitrary unit, transmission axis of polarizing filter oriented vertically. The insets show the electric field sectors (shown as arrows) of each incident collimated vector beam.*

4.2.3 Polarization analysis at lens focal plane

A first method for analysing the focal fields consists in projecting the focused beam through the polarizing filter onto the SPIRICON profiler, located in a range of places along the optical axis of the focusing lens (see Fig.4.3). For practicality, a 300mm lens (Lens 1 in Fig.4.1) rather than the f-theta lens used in subsequent micro-structuring experiments. Fig.4.4 shows the measured intensity profiles when translating the polarization analyzer/camera ±10mm in the vicinity of the lens focal plane and reveals a clear distinction between the vector beams with and without orbital angular momentum. The far field RP, AP and IP beams produced with incident linear vertical polarization on the S-waveplate and polarizer have a distinct double-lobe intensity profile [Fig.4.4(a)-(c)] which rotates with the angle θ and is invariant as it propagates along the optic axis of the focusing lens apart from the obvious scale factor, proportional to the distance away from the focal plane. On the other hand, all the beams with orbital angular momentum have a twisted profile with non-zero intensity at the centre [Fig.4.4(d)-(f)], which varies significantly along the optic axis. These results highlight the complexity of the focal electric fields and the remarkable effect of the presence of a vortex phase on the vector beams which leads to rotation of the vector fields around the focal plane and inversion of the spiral direction, on either side of the focal plane, which was quite unexpected. At the focal plane, the intensity profile has an approximately elliptical shape with spiral arms, indicated in the middle row [Z = 0 , Fig.4.4(d)-(f)] with the long axis of the ellipse

dependent on the incident polarization [i.e. horizontal or vertical when the incident beam is radially or azimuthally polarized respectively, see Fig.4.4(d) and (e) respectively]. A clockwise rotation of the waveplate also caused a clockwise rotation of the ellipse axis, whereas the central peak intensity remains unchanged, which implies a hybrid polarization state.

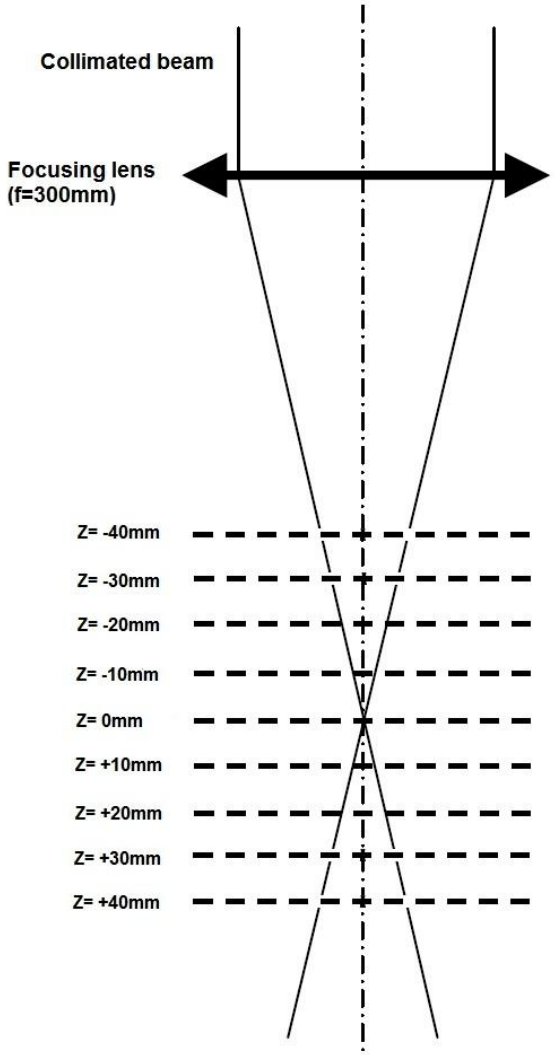

Fig. 4.3 *Schematic showing the focused beam captured by Spiricon camera at range of places along the optical axis of the focusing lens, the focal plane of the lens is set at Z=0mm and the dotted line indicated the camera position.*

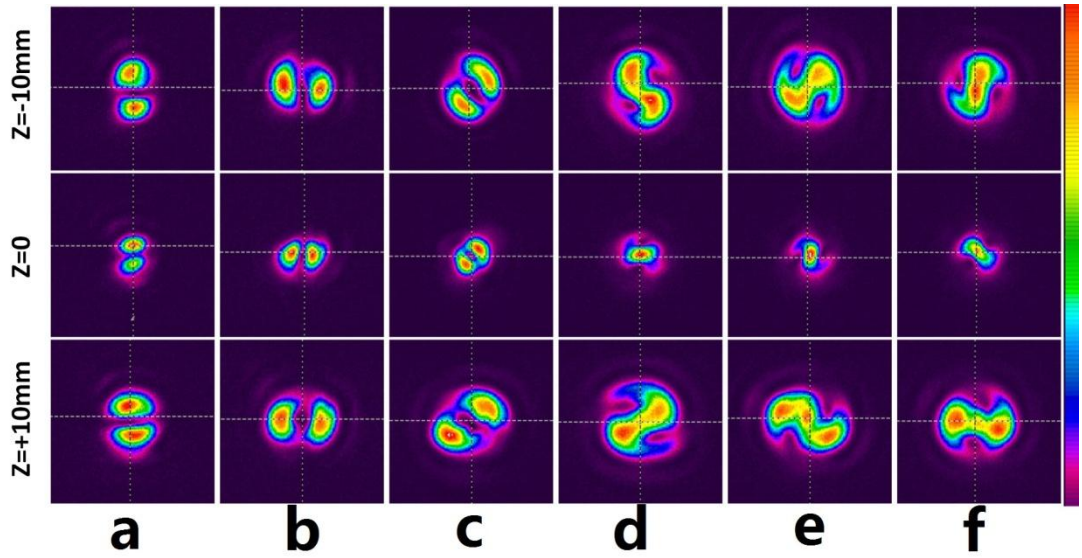

Fig. 4.4 *Reflected intensity distributions measured when polarization analyzer was translated near lens through focal plane, (a) RP (θ = 0°), (b) AP (θ = 90°), (c) IP (θ = +45°), (d) RPAOM, (e) APAOM, (f) IPOAM.*

For further clarity, Fig.4.5 shows the measured reflected intensity profiles measured up to d = ±40mm from the lens focal plane and stacked in an isometric view. The beams without OAM have stationary vector fields with z, but the vector fields with OAM show a non-zero intensity on axis and vector field rotation due to the spiral phase. Thus, the observed profiles along the optic axis over distances much greater than the Rayleigh length.(R ~6mm in this case)

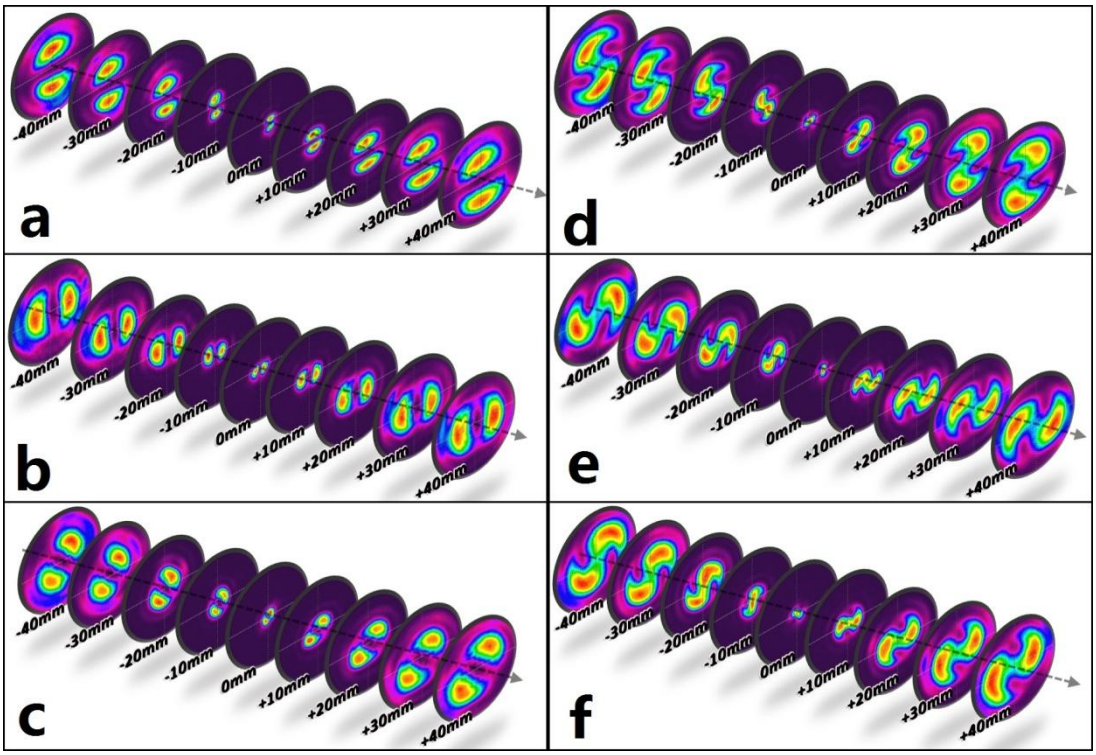

Fig. 4.5 *More detailed polarization analysis along optic axis within ±40mm of the far field, with (a) RP, (b) AP, (c) IP, (d) RPOAM, (e) APOAM and (f) IPOAM.*

The field distribution of the spiral phase mode Laguerre Gaussian LG(0,1)* can be described by [110]:

$$E(r,\phi) = E_0\sqrt{\rho}e^{-\rho/2}e^{\pm i\phi} \qquad \text{Eq.4.1}$$

where r and ϕ are the cylindrical coordinates (where $\rho = 2r^2/\omega_0^2$, ω_0 is the spot size of the Gaussian beam) and helicity depending on the ± sign. Hence, intensity distribution given by $I(r,\phi) = E^*E = I_0\rho e^{-\rho}$, a ring intensity with zero intensity (phase singularity) in the middle, plotted in Fig.4.6(a). In the case of a radially polarized beam with the same intensity distribution passing through a polarizer, the observed double lobe intensity pattern in Fig.4.2 can be understood simply. Following Machavariani [110], the LG(0,1)* spiral phase mode can be represented

by a superposition of two orthogonal degenerate LG modes;

$$E_x(r,\phi) = E_0\sqrt{\rho}e^{-\rho/2}\cos(\phi) \qquad \text{Eq.4.2}$$

$$E_y(r,\phi) = E_0\sqrt{\rho}e^{-\rho/2}\sin(\phi) \qquad \text{Eq.4.3}$$

Radial polarization can thus be represented by radially oriented field vectors, given at each point in the field given by:

$$E(r,\phi) = E_0\sqrt{\rho}e^{-\rho/2}\cos\phi\vec{e_x} + E_0\sqrt{\rho}e^{-\rho/2}\sin\phi\vec{e_y} \qquad \text{Eq.4.4}$$

where $\vec{e_x}$ and $\vec{e_y}$ are the unit vectors in the x and y directions. Passing this beam through a linear polarizer with the transmission axis in the x-direction yields an electric field given by:

$$E(r,\phi) = E_0\sqrt{\rho}e^{-\rho/2}\cos\phi\vec{e_x}\bullet\vec{e_x} \qquad (\vec{e_x}\bullet\vec{e_y} = 0) \qquad \text{Eq.4.5}$$

and hence transmitted intensity distribution,

$$I(r,\phi) = E^*E = I_0\rho e^{-\rho}\cos^2\phi \qquad \text{Eq.4.6}$$

while the reflected intensity (relevant here) must have the angular term $\cos^2\phi$ in Eq. 4.6 replaced with $\sin^2\phi$. This resulting 2D intensity distribution is plotted in Fig.4.6(b) and compares very favorably with that observed in Figs.4.4(a) and Fig.4.5(a) for radial polarization reflected from polarizer. This distribution is valid for both near and far field as vector fields are stationary. For AP/IP states, the intensity distribution requires only a simple rotation (90°/45°).

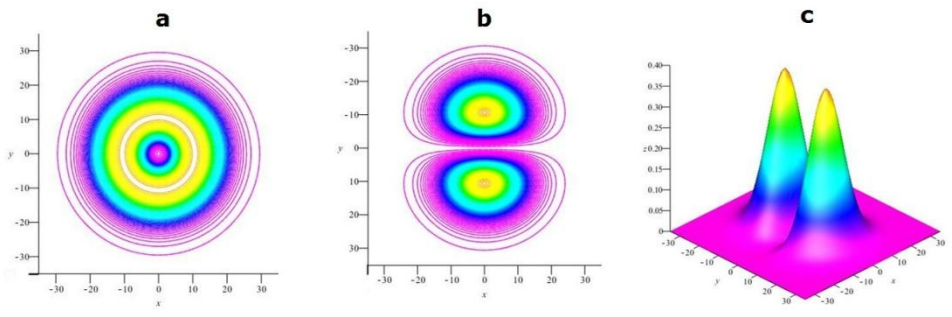

Fig. 4.6 *(a) LG(0,1)* radial polarized intensity distribution 2D, (b) 2D double lobe intensity distribution calculated from Eq.4.6 when a radially polarized beam is reflected from a linear polariser (transmission axis horizontal), (c) 3D intensity representation of (b).*

In the case of polarization states with a helical phase added, this procedure applies approximately when one compares the polarization analysis in the near field (Fig.4.2). However, the far field profiles, Fig.4.4(d-f) are much more difficult to calculate as the vector fields also rotate in the vicinity of the focal plane while changing handedness on either side.

4.2.4 Imprinting and mapping of vectors fields via LIPSS

To better elucidate the focal field properties further, a second focal analysis method is used: each vector beam in turn is used to micro-machine laser ablation spots (and thus imprint its intensity and polarization distribution) on the polished stainless steel sample placed in the focal region of the f-theta lens (Fig.4.1), via laser plasmon structuring. Near threshold ablation on the metal results in the growth of microscopic Laser Induced Periodic Surface Structures (LIPSS) within the ablation spots. The finesse of these low frequency periodic micro-structures with period $\Lambda \sim$

λ initially improves with exposure and develops orthogonally to the local electric field vectors [111, 112]. This enables the analysis of the vector field landscape unambiguously in the focal region, complementing the polarization measurements. By translating the surface above and below the f-theta lens focal plane while observing the LIPSS after laser exposure, the resulting plasmon patterns confirmed the local vector field distributions. With the laser operating at 5kHz frequency, the fluence focused at the sample surface was attenuated to F ~0.4J/cm ^{2}per pulse and exposure set to N = 50 pulses/spot. After laser exposure, the ablation spots were imaged with an SEM microscope.

Fig.4.7 shows SEM images of LIPSS patterns on the ablation spots structured with RP and AP beams, from Z = +0.5mm above the focal plane, at the focal plane, Z =0, and Z =-0.5 mm below the focal plane. The LIPPS, which have an annular structure with zero intensity at centre, are very clear, maintaining their orientation, thus stationary, independent of focus position. Radial polarization produces circular LIPSS and azimuthal polarization produces radial LIPSS, entirely consistent with polarization analysis in Fig.4.4. These patterns also confirm the polarization purity to be excellent.

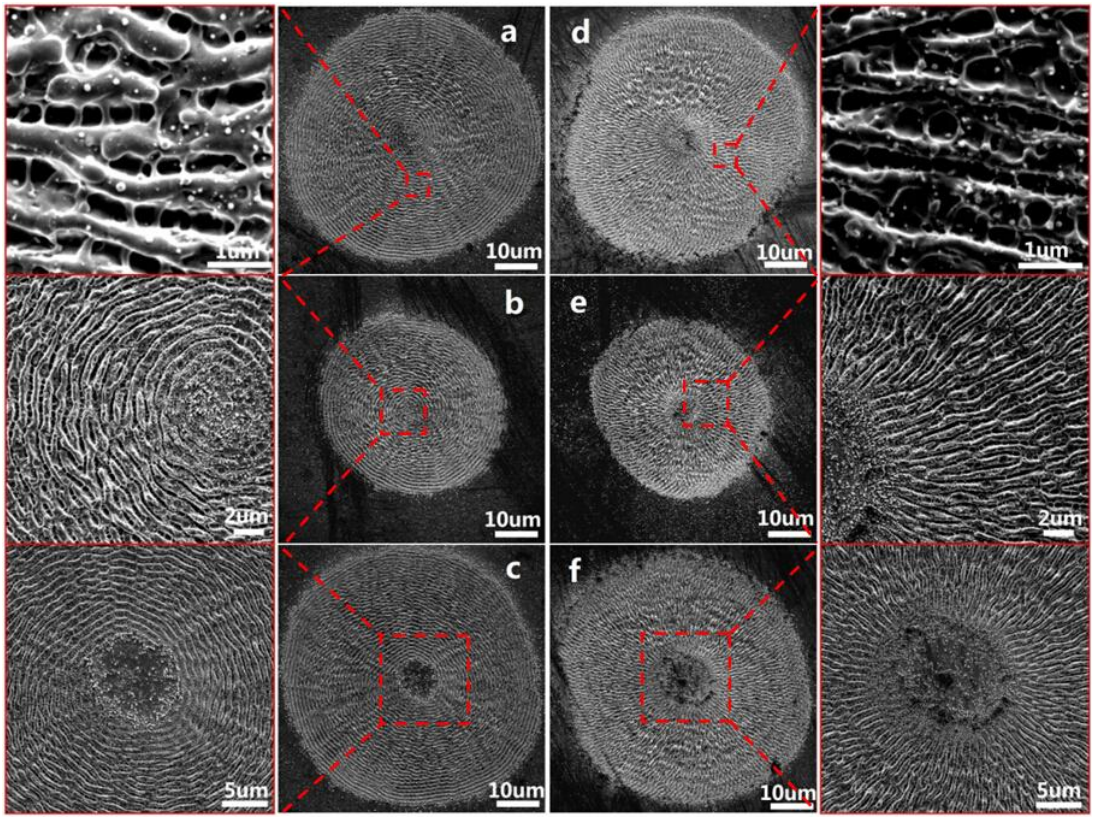

Fig. 4.7 *SEM images of stationary LIPSS patterns structured with RP and AP beams when substrate translated through the focal plane (a) RP 0.5mm above focal plane, (b) at the focal lane and (c) 0.5mm below the focal plane, (d) AP 0.5mm above focal plane, (e) at the focal plane and (f) 0.5mm below the focal plane.*

Fig.4.8 shows the ablation spots produced around the focal plane when the RPOAM and APOAM beams had a helical phase added with topological charge $m = 1$. The SEM images now confirm that there is no singularity thus showing ablation at centre consistent with a Gaussian-like intensity profile already observed in the polarization measurements, [Fig.4.3(d) and (e)]. There may however be some distortions induced due to steps in the vortex phase-map applied to the SLM. From Fig.4.8, clear spiral LIPSS are produced just outside the central region but LIPSS finesse reduces at the centre of the focal spots, which one might expect to be due to overexposure. However, when significantly reducing fluence per spot, it remained difficult to

produce clear LIPSS in the centre of the laser focal spots, consistent with the centre being circularly polarized [110]. Furthermore, the incident RPOAM beam produced a focal spot with LIPSS oriented in a radial pattern confirming that the focal field was azimuthally polarized in these regions, and vice versa with azimuthal, consistent with previous study by Allegre et al [45]. The addition of OAM thus appears to transform the incident RPOAM beam to its orthogonal state (APOAM) at the focal plane and vice versa. The spiral direction (right handed above) also reverses to left handed below the focal plane, in accord with the spiral flip observed on the polarization analysis.

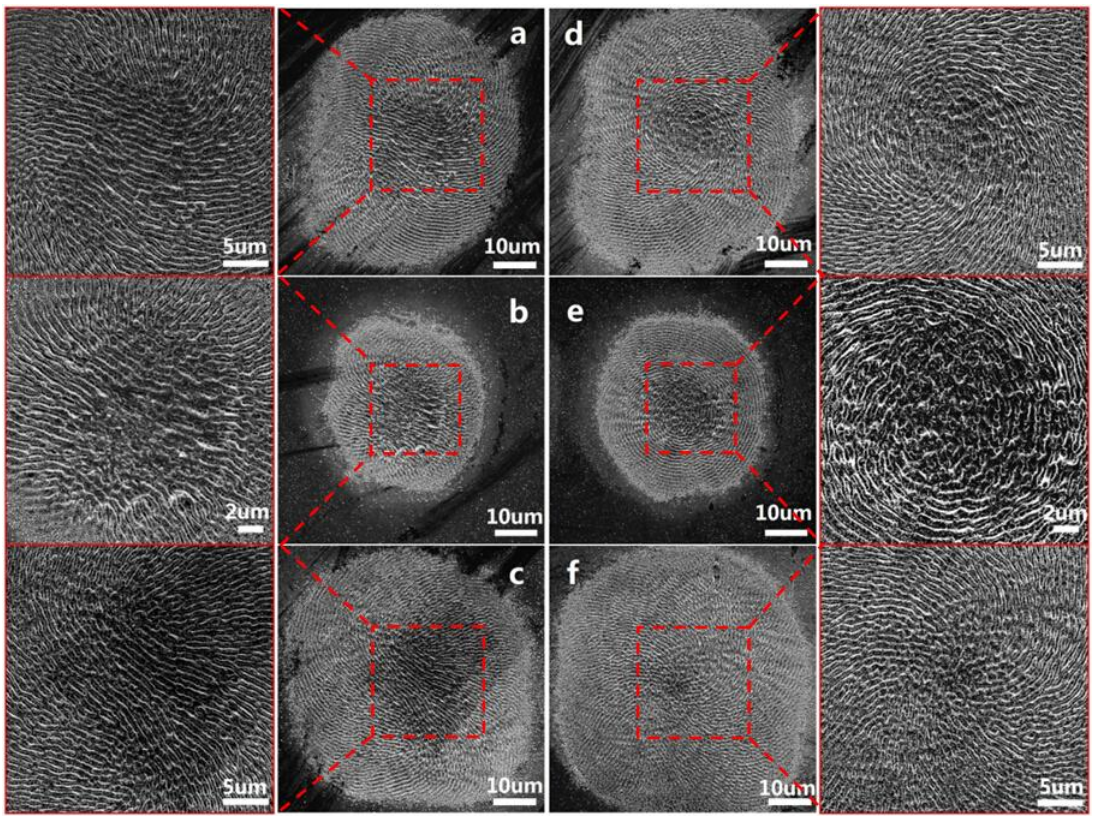

Fig. 4.8 *LIPSS formation with the RPOAM and APOAM beams when substrate translated through the focal plane (a) RPOAM 0.5mm above focal plane, (b) at the focal lane and (c) 0.5mm below the focal plane, (d) APOAM 0.5mm above focal plane, (e) at the focal plane and (f) 0.5mm below the focal plane. The spiral structures reverse direction above and below the Fourier plane consistent with polarization observations.*

4.2.5 Focal field analysis using Jones vector formalism

From section 4.2.3, the CV beams with various polarization were analysed by the focal intensity profiles. Here a simple analytic model based on Jones vectors which mathematically presents the focal filed polarization was used to complement the experimental analysis above. For brevity, the focal fields are only expressed at two specific points in the focal plane: at the optical axis (shown as Point $\boldsymbol{O}$ in Fig.4.9) and at a location corresponding to the edge of the focal spots (Point $\boldsymbol{A}$ in Fig.4.9). Thanks to cylindrical symmetry, the polarization properties at other points in the focal plane can then be inferred from those at Points $\boldsymbol{O}$ and $\boldsymbol{A}$. The focal fields are expressed as Jones vectors noted $E_{\boldsymbol{O}}$ and $E_{\boldsymbol{A}}$ in a coordinate system designated $(\boldsymbol{O}, \vec{\boldsymbol{X}}, \vec{\boldsymbol{Y}})$, which is defined in Fig.4.9. The focal Jones vectors produced with radially polarized incident beams (with or without orbital angular momentum) are all summarized in Table 4.1.

When the incident radially polarized beam has no angular momentum, the resulting focal Jones vector at Point $\boldsymbol{O}$ has a zero amplitude (Table 4.1) and the Jones vector at Point $\boldsymbol{A}$ is oriented radially (i.e. along the axis $\boldsymbol{X}$). All the places located at same distance from the centre as Point $\boldsymbol{A}$ also have polarization vectors oriented radially (i.e. away from the centre). This is shown in Fig.4.10(a). Note that the beams without orbital angular momentum, produce a ring-shaped distribution (zero field amplitude shown as a dot in the centre) since all the electric field vectors cancel each

other out at the optical axis. On the other hand, when the incident beam has angular momentum of m=1, the resulting focal Jones vectors have higher amplitude at Point ***O*** than at Point ***A*** (see normalized vector amplitudes in Table 4.1). The polarization is circular at Point ***O***, whereas at Point ***A*** it is elliptical with a strong elongation along the axis ***Y*** (see Table 4.1). In other words, the electric field vector at Point ***A*** is mostly oriented azimuthally (i.e. tangentially from the centre). All the places located at same distance from the centre as Point ***A*** also have polarization vectors mostly oriented azimuthally, as shown in Fig.4.10 (b).

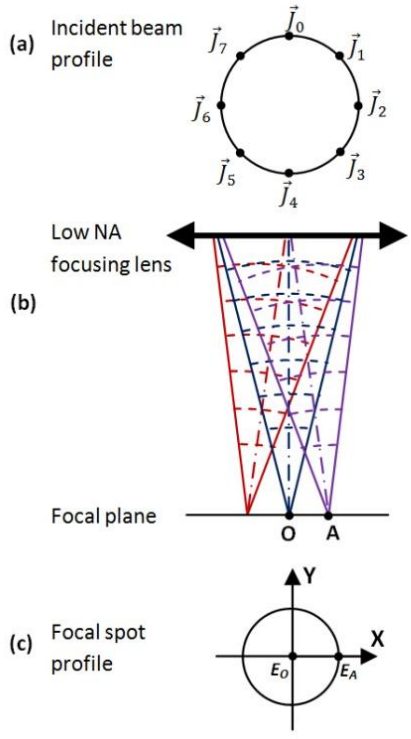

Fig. 4.9 *Schematics showing: (a) eight Jones vectors J_i in an incident collimated beam profile; (b) a side-view of the focused wavefront; (c) the reference coordinate system (**O**, **X**, **Y**) at the focal plane.*

Table 4.1 Jones vectors in the focal plane. The location of Points ***O*** and ***A*** in the focal plane are shown in Fig.4.9.

Incident collimated beam configuration	***Focal plane position***	***Jones vector components (X; Y)***	***Jones vector normalized amplitude***
Radially polarized beam without angular momentum -RP	*Point **O***	$E_O = (0\ ;\ 0)$	*0*
	*Point **A***	$E_A = 0.57\times(1\ ;\ 0)$	*~0.57*
Radially polarized beam with angular momentum -RPOAM	*Point **O***	$E_O = 0.5\times(e^{i\frac{\pi}{2}}\ ;\ 1)$	*~0.71*
	*Point **A***	$E_A = (0.1e^{i\frac{\pi}{2}}\ ;\ 0.4)$	*~0.41*

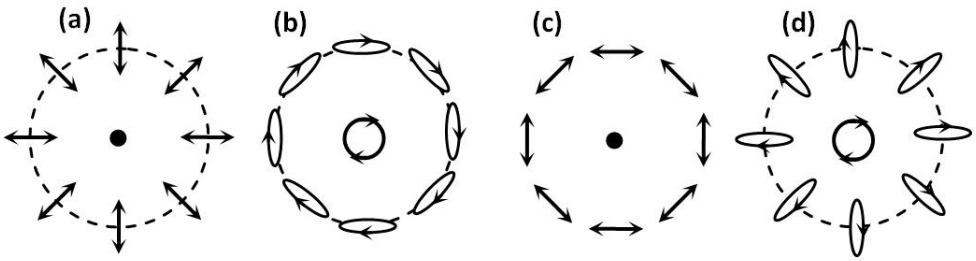

Fig. 4.10 *Schematics showing the focal electric field vectors (shown as arrows) produced by low NA focusing of (a) RP beam; (b) RPOAM beam (topological charge of m=1);* ***(c)*** *AP beam and* ***(****d) APOAM beam (topological charge of m=1).*

The Jones vectors in Table 4.1 explain how the orbital angular momentum affects the focal fields of radially polarized beams: "adding" angular momentum of *m*=1 to a radially polarized beam converts the focal field from an annular distribution (i.e. with zero intensity in the centre) to a near Gaussian distribution (with peak intensity in the centre). Furthermore, the focal field has a hybrid state of polarization, circular near the central peak and mostly azimuthal in the wings of the Gaussian profile. Note that the focal fields of incident azimuthally polarized beams with orbital

angular momentum were modelled in the same way and the results are consistent with those described above: a near Gaussian profile is obtained with a hybrid polarization state. Importantly, this Jones vector analysis clarifies the experimental results in previous section, such as the elliptical intensity profiles in Fig.4.4 (which is due to the hybrid polarization state with a partial inversion at the focal plane), or the absence of clear LIPSS in the centre of the laser spots in Fig.4.8 (the circular polarization prevents their formation). Furthermore, the partial inversion in the state of polarization around the edges of the laser spot is a peculiar phenomenon with implications for micromachining.

4.2.6 Discussion

In the early attempts, to achieve the aim of polarization analysis the CV beam with various wavefront, only one SLM and without S-waveplate setup was tested. However the output of the CV beams by this method gains distortion due to the resolution limit from SLM when generating the vortex wavefront polarized beams. To solve this limitation, a possible way is to apply two SLM setup method which was mentioned in Chapter 2.3.2.1(see Fig.2.9). But the two SLM setup was much more expensive than the setup combined SLM and S-waveplate. So in the further experiment, the current setup with one SLM and S-waveplate was considered as a proper solution and implemented through the research.

From experimental results, two diagnostic techniques were used to characterize the optical properties of these vector beams: one for analyzing the beam profile and polarization using a Spiricon camera with polarizing beam splitter and the other for analyzing intensity/polarization by imprinting LIPSS on a polished stainless steel surface with multi-pulse low fluence exposure.

In polarization analysis at lens focal plane, here used a 300mm lens (Lens 1 in Fig. 4.1) rather than the f-theta lens used in experiments which increasing the beam spot size and would be beneficial in intensity profile observation on SPIRICON carema. With the help of polarizing filter, distinctive beam intensity distribution with various polarization state after focusing has been observed. Radial and azimuthal polarization states (and superpositions states) without OAM maintain a stationary electric field distribution along the propagation axis and LG intensity with a polarization singularity and intensity distribution scaling with distance from the focal plane. On the other hand, the effect of adding a helical phase applied to the SLM results in clear rotation of the vector fields with spiral direction inverting above and below the focal plane. The results of measuring up to ±40mm from the lens Fourier plane reveals how the orbital angular momentum associated with a vortex wavefront induces complex field landscapes, the apparent inversion in the state of polarization around the edges of the spots is an unexpected phenomenon. However, these far field profiles with adding OAM (m=1) are so much complex to

calculate as the vector fields also rotate in the vicinity of the focal plane.

In surface processing analysis, The wavelength-sized LIPSS typically develop orthogonally to the local electric field vectors and thus enable to analyse the vector field landscapes in the focal region with a better accuracy than the optical analysis method above. For planar wavefront, LIPSS are produced with a high uniformity within the ablation spots and indicate that the polarization state is maintained in all observation planes, with no variation along the optical axis of the focusing lens. On the other hand, the geometry of the laser spots with vortex wavefront, with deeper ablation in the centre than around the edges, was consistent with a Gaussian-like intensity profile. It can be seen that LIPSS have been produced around the edges, but not in the centre of the focal spots. Further ablation experiments with various fluence values showed that it was extremely difficult to produce clear LIPSS in the centre of the laser focal spots, which can be concluded with the centre being circularly polarized.These important experimental results demonstrate the variability of the focal fields along the optic axis due to the addition of orbital angular momentum. Cardano et al [108] previously investigated experimentally the effect of spin to OAM conversion with a "q-plate" and measured the detailed spatial vector fields (via Stokes parameters) near the focal plane of a lens within one Rayleigh range. Their results showed a clear vector field rotation as observed here by both polarization analysis and surface micro-structures.

4.3 Spiral LIPSS surface processing

4.3.1 Aim of experiment

Radial and Azimuthal polarizations are extreme examples of these interesting states with ring intensity modes and polarization singularities. Their superpositions result in electric fields displaying a logarithmic spirals. Here the ultrafast laser induced periodic surface micro-structuring was used to elucidate and confirm these vector fields when micro-structuring metal surfaces with picosecond laser exposure.

4.3.2 Experimental setup

The same picosecond laser processing setup in Fig.4.1 was used with the SLM acting as a mirror while altering linear polarization direction incident on the S-waveplate.

4.3.3 Results and discussion

With OAM removed while rotating the S-waveplate to intermediate angles, -90° < θ < 90°, a series of unique, remarkable spiral Plasmon micro-patterns resulted at the lens focal plane, Fig.4.11. By rotating the S-waveplate axis (angle θ) relative to the incident linear polarization, it was possible to generate plane wave radial (θ = 0°) and azimuthal (θ = ± 90°) polarizations and a series of highly interesting spirals at intermediate angles. Orthogonal polarization states have a $\delta\theta$ = 90° hence Fig.4.11(a) and (e), (b) and (f), (c) and (g), (d) and (h) correspond to orthogonal polarization

states.

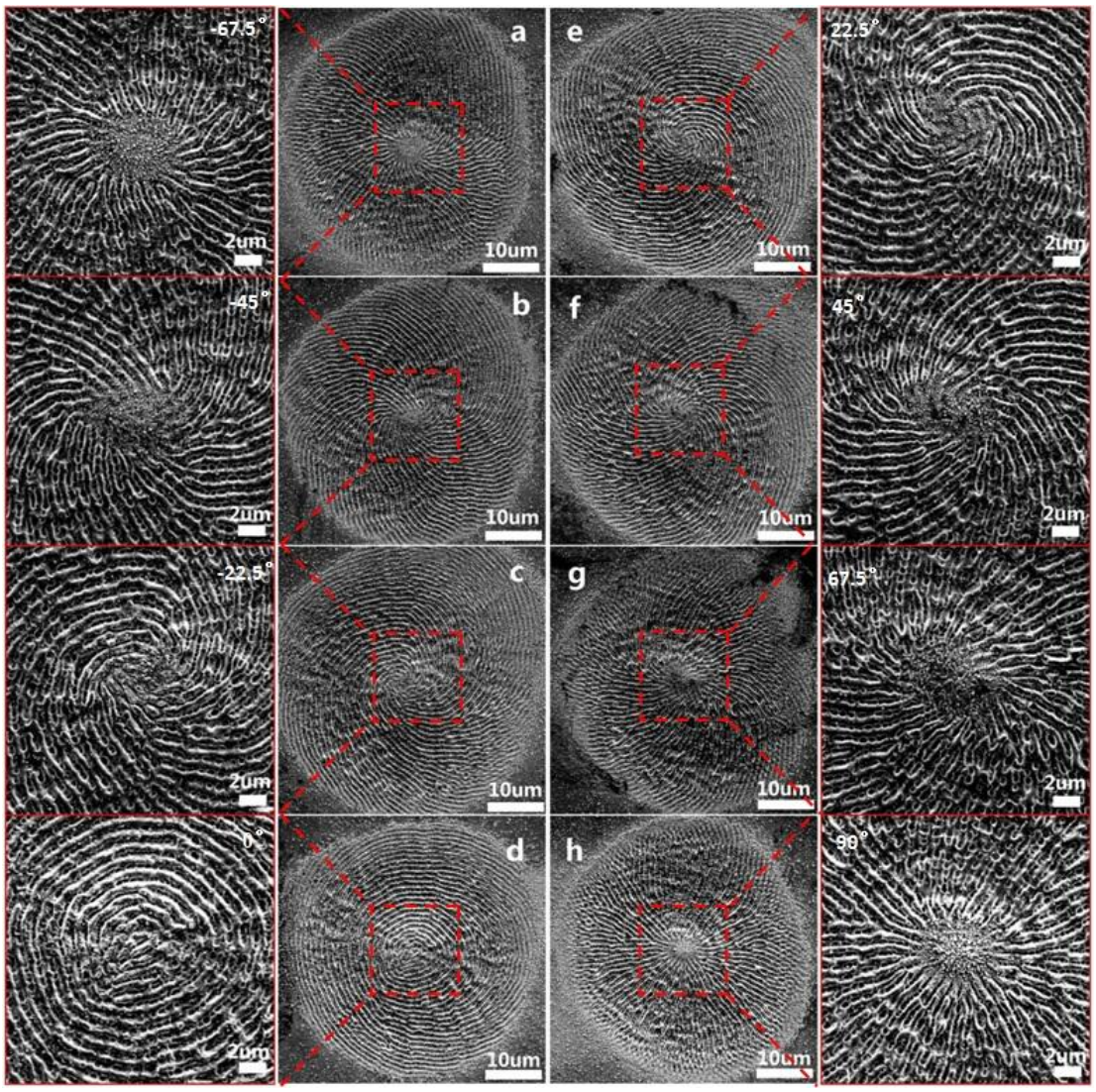

Fig. 4.11 *SEM images of spiral plasmons from superposition states generated by altering S-waveplate axis θ (a) -67.5°, (b) -45°, (c) -22.5°, (d) 0° (radial), (e) +22.5°, (f) +45°, (g) +67.5° and (h) +90° (azimuthal).*

The spiral geometry has been analyzed for θ = 22.5° and 45° and found to fit closely the logarithmic spiral function, $r(\phi) = ae^{k\phi}$ where a = 0.57 (with r in μm) and k = 0.414 and 1.0 respectively. The constant k determines the spiral winding and thus $k = \tan\theta$. The theoretical fits to these spirals are shown in Fig.4.12(a) and (b) which

match the observed structures quite well. The fit to $\theta = 22.5°$ looks even better. All the spirals are logarithmic where the spiral separations along a given axis increase with rotation. At any given point in the field, the tangent to the curve and a radial line from the centre has a fixed angle.

It can be confirmed that the spiral micro-structures result from a superposition of the radial and azimuthal vector field components. Such logarithmic spiral electric fields, due to superpositions of radial and azimuthal polarizations were previously predicted by F.Gori in 2001 [113]. Fig.4.12(c) also supports this idea which shows the vector field in a geometrical model (when $\theta = 45°$) when summing radial and azimuthal field components with equal amplitude at each location in the vector field.

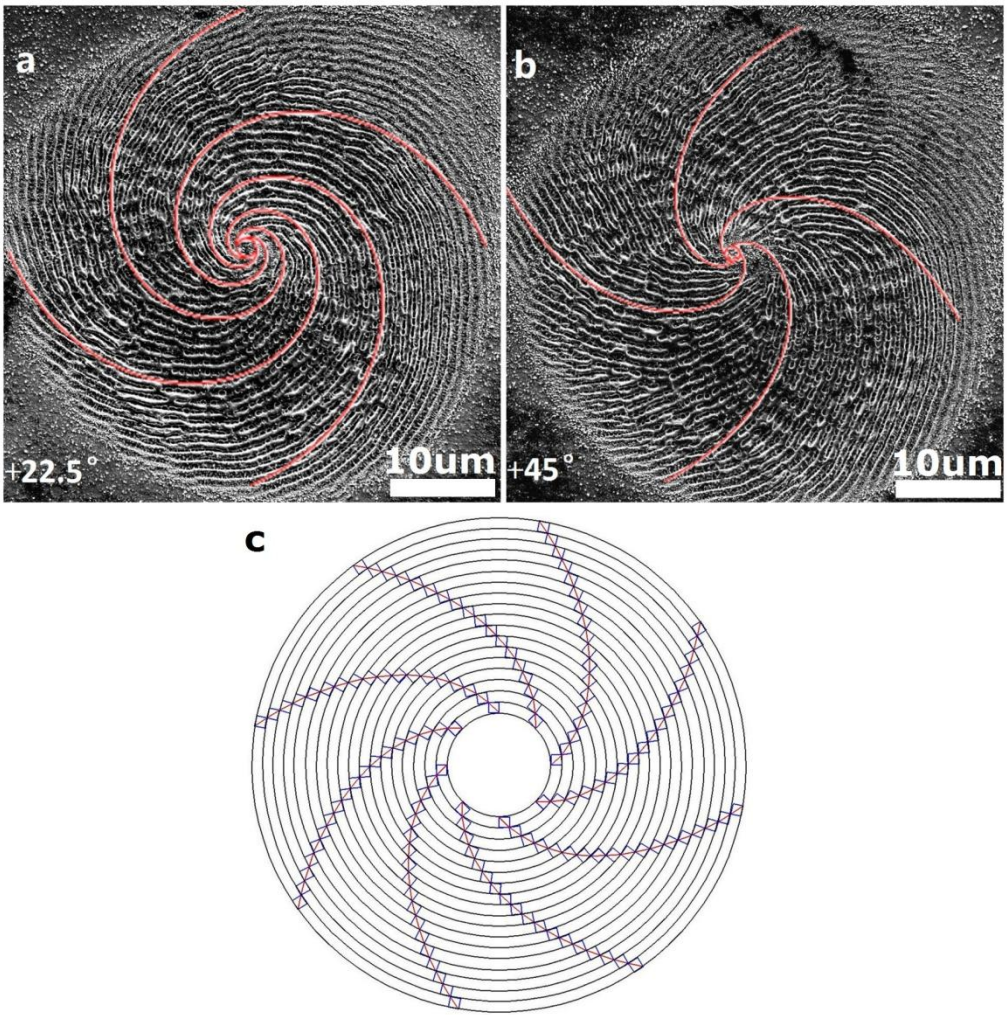

Fig. 4.12 *Detail of SEM images at (a)* θ *= 22.5 °and (b)* θ *= 45 °with the theoretical fits to logarithmic spirals (red curves) where* a *= 0.57 and* k *= 0.414 and 1.0 respectively, (c) a simple geometric superposition of radial and azimuthal field components (with equal amplitude) at* θ *= -45 °, generating a spiral electrical field distribution whose field direction is orthogonal to the plasmon spirals at every location in (b).*

The ablation spots on the polished stainless steel would appears a complex surface patterning with logarithmic spiral structure. These are the first observations of such micro-structured spirals in experiment created by multi-pulse exposure with spiral vector fields.

A phase only SLM can also rotate linear polarization by combining the SLM with a quarter waveplate (after SLM) with incident linear polarization set at 45° to the SLM director. With quarter waveplate fast axis set at 45°, CGH's with varying grey levels then generate elliptical polarizations which are converted to linear polarizations (after the quarter waveplate) whose orientation rotates with grey level. When synchronized with motion control at the substrate, this allowed dynamic complex plasmon structuring on stainless steel. Using this approach, Fig.4.13 shows a 4x4 spot array representing a circulant matrix where the main diagonal was micro-structured with radial polarization while the off axis elements were structured with superposition states.

Exposure was set to N = 50 pulses/spot at a fluence F ~ 0.4J/cm ²per pulse at 5kHz repetition rate. Pre-saved grey level maps in the Hamamatsu software were run in sequence with a delay of 200ms applied between exposures to allow CGH's to refresh completely. Trigger signals were generated by the RTC4 card controlling the Galvo positioning and hence synchronization.

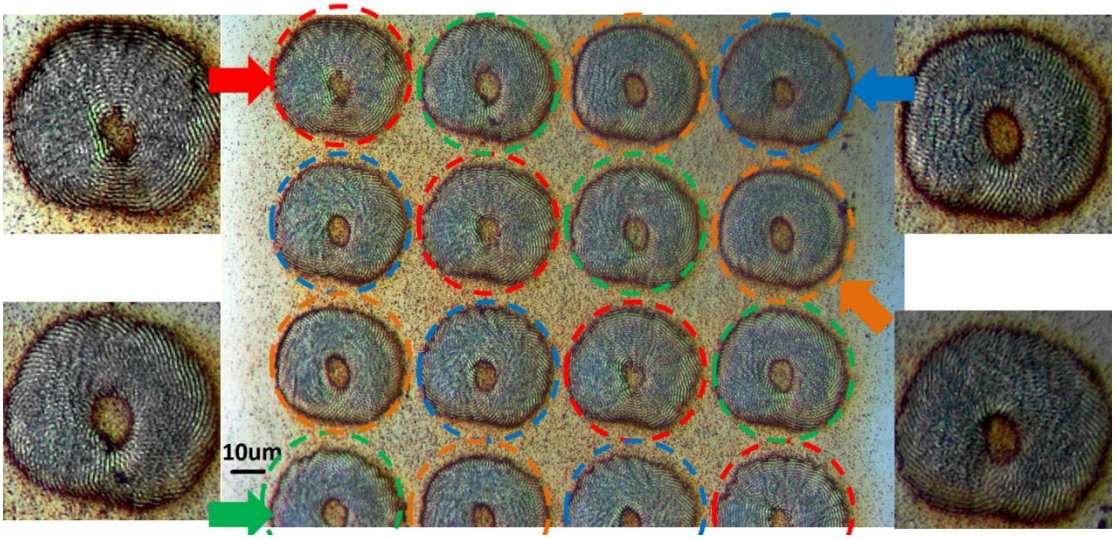

Fig. 4.13 *dynamic surface plasmon structuring representing 4x4 circulant matrix with radial polarisation on the main diagonal. The various states of polarization were synchronized with galvo motion on the surface.*

Applications of these complex spiral structures and field distributions are envisaged. For example, polymer moulds of these 40μm diameter spirals, although having ~ 1μm pitch (and which have smaller nano-structures within) might well affect cell interactions on surfaces if the pitch of these LIPSS could be reduced with shorter wavelengths, which could be expected. The spots inscribed with different vector states also represent a form of information encoding. If one dynamically rotates incident linear polarization (possible with the SLM) while synchronizing motion on a substrate [46], pre-determined patterns could be created at will. In the case of utra-high intensity femtosecond pulses with these spiral electrical fields, particle acceleration might be advanced. It is interesting to note that by starting with patterned dielectric arrays of SiN nano-pillars in a Vogel spiral, near field coupling of the incident radiation along the spiral arms was recently experimentally

demonstrated and theoretically predicted [114].

4.4 Chapter summary

In this Chapter, using the S-waveplate, plane wave radial and azimuthal polarizations and their superpositions, logarithmic spirals (RP, AP and IP respectively) were created. These are stationary vector fields so that local polarization direction is an invariant property as the beam propagates along the optic axis of a low NA focusing lens. When focused, these states maintain a ring (Laguerre-Gaussian) intensity distribution which scales linearly with distance from the focal plane with zero intensity (polarization singularity) in the middle.

Surface Plasmon patterning with plane wave radial and azimuthal polarizations confirmed that the directions of local electric field vectors were orthogonal to the LIPPS directions. Complex logarithmic spiral Plasmon structures were created by employing spiral polarized beams generated by altering linear polarization direction incident on the S-waveplate axis, which could be altered from right to left handed along with the degree of spiral. These are the first experimental observations of such spiral vector fields, confirmed by multi-pulse exposure on a polished metal surface with picosecond laser pulses. The spiral vector fields have been shown to result from superpositions of radial and azimuthal polarizations with varying amplitudes and

theoretically modeled with satisfactory results.

With the S-waveplate and SLM together, a vortex phase was applied with topological charge m=1 adding orbital angular momentum to these beams, non-stationary vector field results and beam propagation in the region around the focal plane, shows a twisting profile with non-zero intensity at the centre. This highlights the remarkable effect of the vortex phase on the vector beams leading to rotation of the vector fields around the focal plane, changing direction on either side. These conclusions were supported umambiguously by polarization/intensity analysis around the focal plane and by imprinting complex LIPSS above and below the focal plane on a polished surface, elucidating the three dimensional structure of these polarization states when focusing with a low NA lens. At the focal plane, the polarization near the centre appears to be circular, thus orbital angular momentum can be converted to spin angular momentum.

By synchronizing state of polarization with motion control at the substrate, this allowed dynamic complex plasmon structuring on stainless steel. Using this approach, a 4x4 spot array with a range of polarizations representing a circulant matrix was demonstrated. Such a matrix can be viewed as a form of information encoding.

Chapter 5 Ultrashort pulse laser micro-drilling study by using cylindrical vector beams

5.1 Introduction

In the previous chapters, a Polarization Mode Converter setup has been introduced and demonstrated how it can produce a radial or an azimuthal polarization state at the focal plane of a low NA focusing optics. The Polarization Mode Converter was studied both experimentally and theoretically, indicating that an inversion in the state of polarization occurs, i.e. the state of polarization with OAM (m=1) at the focal plane is orthogonal to that of the collimated beam before the focusing optic.

In this chapter, the Polarization Mode Converter is combined with high laser beam fluence to micro-drill stainless steel and silicon wafer plates. Recent experimental work [1,4,51] also investigates micro-machining with radial and azimuthal states of polarization, suggesting that the potential benefits of using these states of polarization are more subtle than predicted in early theoretical studies [4]. Depending on the material, processing parameters and aspect-ratio of the machined structures, either a radial, an azimuthal or a circular polarization is most efficient. In particular, Meier et al. demonstrated experimentally, using a nanosecond-pulse laser source, that a radial polarization is usually more efficient than other modes at drilling through 1-3mm thick brass and copper plates, whereas an azimuthal polarization is more efficient at drilling mild steel plates of similar thicknesses[51]. M. Kraus *et al.* compared the efficiency of drilling 0.5-1mm thick steel plates with a radially and an azimuthally polarized beam, using a picosecond-pulse laser source

[1]. It was shown that the azimuthally polarized beam was more efficient at micro-drilling high-aspect-ratio holes when the plate thickness was above 0.5mm.

The work presented in this chapter focuses on micro-machining 0.3-0.5mm thick sample substrates using a picosecond-pulse laser source with the Polarization Mode Converter described in earlier chapters. A comparative analysis of micro-machining with radially, azimuthally, circularly and linearly polarized beams with or without Orbital Angular Momentum(OAM) is carried out. In each case, the results are compared between the various states of polarization.

Thanks to the dynamic nature of the SLM along with the S-wave plate, the state of polarization can be programmed and modified to better suit an industrial process, without requiring any mechanical rotation of the polarization optics. Hence, compared with the other methods for producing cylindrical vector beams (CVBs) used in the experimental work described above, the Polarization Mode Converter allows further flexibility.

5.2 Micro-drilling

5.2.1 Aim of the experiment

During a laser micro-machining process such as helical drilling, multiple internal reflections occur inside the holes. Polarization affects the laser-material energy

coupling at each reflection. In this chapter, the tailored focal fields demonstrated in chapter 4 are used for helical micro-drilling of stainless steel and silicon substrates and results, in terms of quality and efficiency, compared with traditional polarization states (circular and linear). This illustrates how the distinct machining properties associated with each beam make it best suited for specific processes or materials.

5.2.2 Experimental setup and procedure

The experimental setup of this micro-drilling test used the High Q picosecond laser system in Chapter 4, Fig.4.1. For the drilling experiments, samples are mounted on a precision 5-axis motion control system allowing accurate positioning in the focal plane of the f-theta lens. Having demonstrated the ability to manipulate vector beams and shape the focal fields into various complex landscapes in Chapter 4, the micromachining properties can be investigated by some of these vector beams (i.e. RP, AP, RPOAM and APOAM beams). For comparison purposes, linearly and circularly polarized Gaussian and "donut" beams (the latter are simply obtained by inducing an orbital angular momentum of m=1 to the linearly or circularly polarized Gaussian beams) also used. Trepanning drilling carried out on stainless steel 302 sheets (370um and 500um thick) and silicon wafers (500um thick) which are typical substrates used in industrial micromachining. All the drilling tests use a pulse energy of 80μJ (i.e. an average fluence of 11.3J/cm^2 at the focal plane) with a pulse

repetition rate of 10kHz, and the beam is scanned (trepanned) along a circular path with a 100μm diameter and a 20mm/s scan speed. Various laser exposure times were as follows; 20s, 45s, 70s on 370μm stainless steel sheet; 45s, 70s, 140s on 500um stainless steel sheet and silicon wafer.These tests are repeated 10 times with each vector beam to average the results. After laser drilling, all the results are analyzed with an optical microscope.

5.2.3 Results and discussion

First, the results are assessed qualitatively by comparing the relative size, shape and edge quality of the drilled holes. Figs.5.1, 5.2 and 5.3, which show typical holes drilled in the silicon and steel substrates, highlight significant differences in the hole geometry produced with AP and APOAM beams (i.e. with a annular and Gaussian focal intensity profile respectively). This is especially visible with the exit holes, which are larger and smoother in the latter case (see for example Fig.5.3-a and - b). In fact, the APOAM beam produces holes which are more similar to those made with the circularly polarized CP Gaussian beam (see exit holes, Fig.5.3-c). Note that the linearly polarized (LP) beam produces the worst drilling quality, with a distorted hole entrance and elliptical exit.

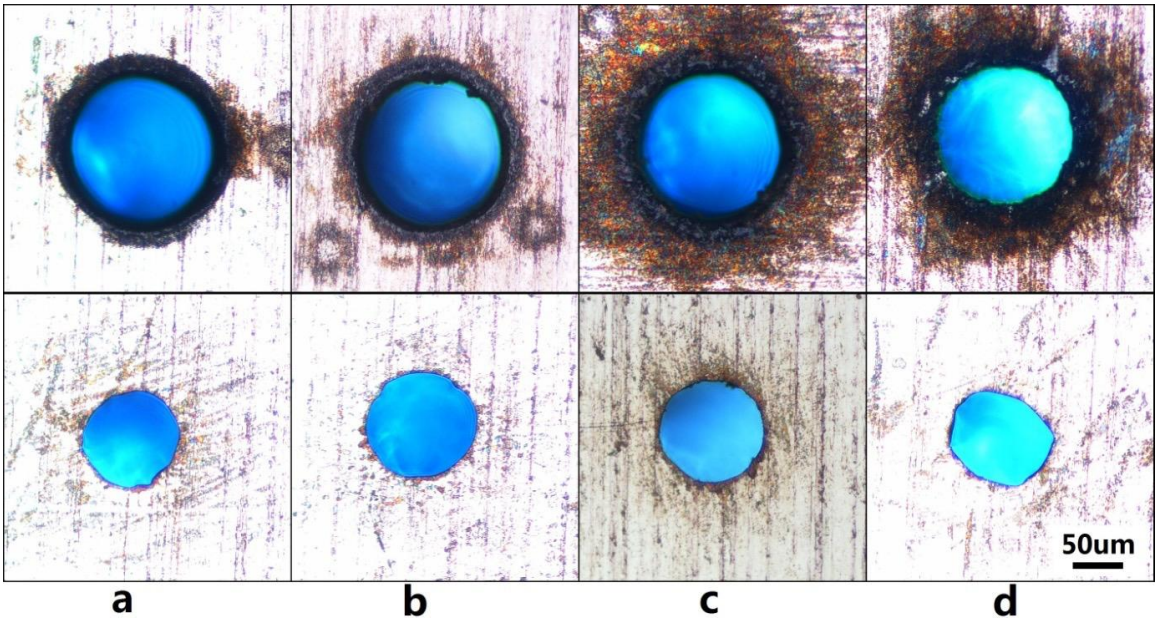

Fig. 5.1 *Optical micrographs showing drilling results on 370um Stainless Steel sheet with: (a) AP, (b) APOAM, (c) CP and (d) LP beams at fluence ~11.3J/cm^2 and with ~20s laser exposure duration. Top row shows the entrance and bottom row the exit.*

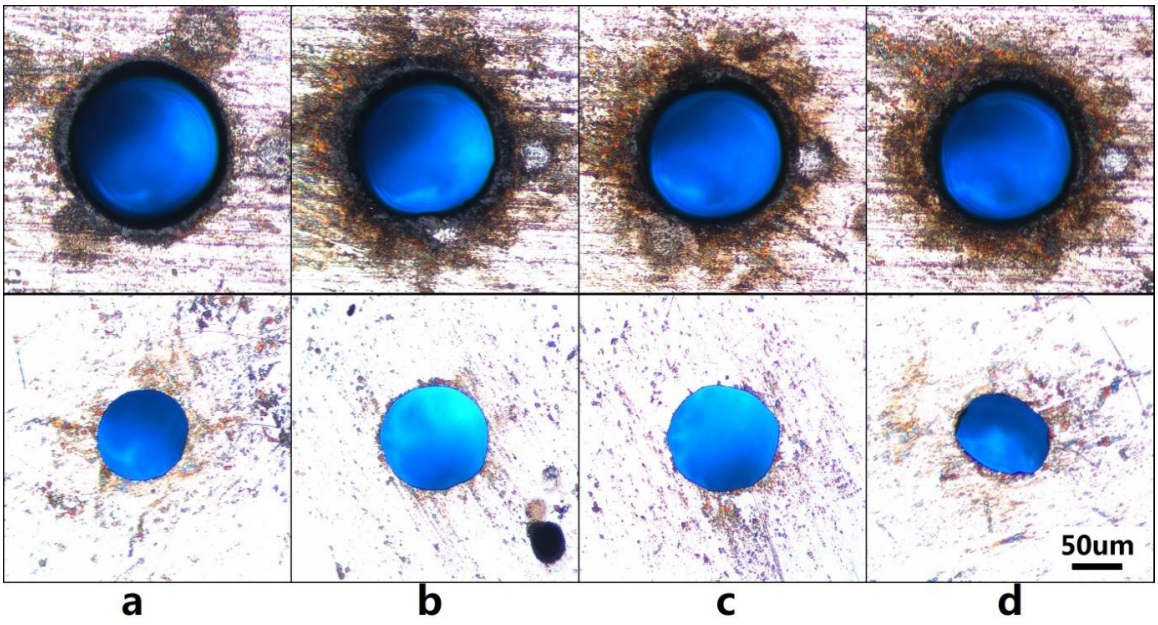

Fig. 5.2 *Optical micrographs showing drilling results on 500um Stainless Steel sheet with: (a) AP, (b) APOAM, (c) CP and (d) LP beams at fluence~11.3J/cm^2 and with ~70s laser exposure duration. Top row shows the hole entrance and bottom row the exit.*

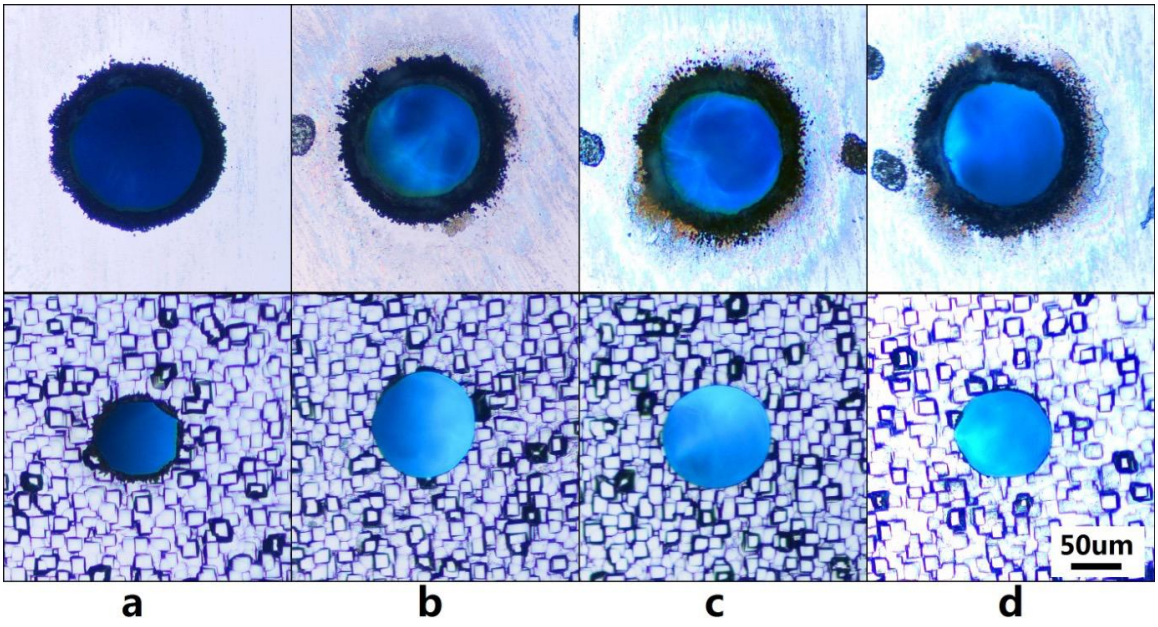

Fig. 5.3 *Optical micrographs showing drilling results on 500um Silicon wafer with: (a) AP, (b) APOAM, (c) CP and (d) LP beams at fluence~11.3J/cm^2 and with ~140s laser exposure duration. Top row shows the entrance and bottom row the exit.*

Next, the drilling efficiency of the vector beams were evaluated by measuring the diameter of the produced holes entrance and exit. The complete drilling results with various exposure times are showing in table 5.1. As the linear polarization produces elliptical exit holes, this led to less accurate results, hence this data are not included. As seen, with the exposure time increasing, the exit hole's diameter, becomes larger, as more material is machined away near the exit side. However, the entrance diameters for a given polarization (and so intensity distribution) are almost independent of exposure time since fluence is well above ablation threshold, so entrance dimensions saturate certainly within < 20seconds.

Table 5.1 Complete drilling results for the cylindrical vector beams with various laser exposure time.

370um Stainless Steal						
Entrance diameter(um)						
Exposure duration(s)	RP	RPOAM	AP	APOAM	CP	CPOAM
20	170.336	162.984	170.476	162.468	162.348	171.812
45	171.492	164.676	171.364	164.468	163.383	172.816
70	172.252	166.272	172.424	166.58	164.226	174.261
Exit(um)						
Exposure duration(s)	RP	RPOAM	AP	APOAM	CP	CPOAM
20	94.116	96.872	86.064	98.404	97.940	86.832
45	104.68	106.868	96.876	110.880	109.548	96.084
70	109.068	111.688	103.736	115.416	114.228	104.864
500um Stainless Steal						
Entrance(um)						
Exposure duration(s)	RP	RPOAM	AP	APOAM	CP	CPOAM
45	171.676	164.780	171.596	164.937	163.508	172.632
70	172.32	166.962	172.976	166.232	164.312	173.952
140	173.748	167.134	173.968	167.95	165.42	174.964
Exit(um)						
Exposure duration(s)	RP	RPOAM	AP	APOAM	CP	CPOAM
45	82.888	94.224	79.136	97.044	97.192	78.66
70	93.964	106.608	89.32	109.296	107.424	91.73
140	101.084	113.416	97.448	115.384	112.508	99.704
500um Silicon wafer						
Entrance(um)						
Exposure duration(s)	RP	RPOAM	AP	APOAM	CP	CPOAM
45	139.036	123.708	138.304	123.08	123.54	139.32
70	139.58	124.096	139.304	124.396	125.084	141.64
140	141.676	126.104	141.604	124.76	125.388	143.324
Exit(um)						
Exposure duration(s)	RP	RPOAM	AP	APOAM	CP	CPOAM
45	85.508	97.284	78.896	97.504	97.724	80.736
70	87.132	106.284	80.148	108.908	107.024	81.748
140	88.056	111.992	81.124	114.172	112.864	84.952

In order to compare the results more rigorously, the complete data for the 3 substrates were statistically analyzed on both faces. The results of the average diameter of holes drilled in the silicon and stainless steel plates are plotted in Fig.5.4. In addition, the difference value of each hole's entrance and exit plotted in Fig.5.5.

For further understanding the drilling hole's geometry, the best method is to investigate the cross-sectional view of these holes and did trials in the early experiment. However due to the hole diameter is very small, it is difficult to prepare the cross-sectional view sample by the available laboratory device. So, this experimental analysis is only based on the entrance and exit diameter in this thesis.

Looking at the results obtained in the 500μm thick steel and 500μm thick silicon plates, the most noticeable feature is the similarity in the drilling characteristics of the RPOAM, APOAM and CP beams, since they all produce comparable hole geometries (~125μm diameter entrance and ~112μm diameter exit in silicon i.e. a sidewall half-angle taper of only ~1.5°). On the other hand, the RP and AP beams *without* angular momentum have broadly similar characteristics as the CPOAM beam (producing holes of ~142μm diameter entrance and ~84μm diameter exit in silicon i.e. a significantly larger half-angle taper of ~6.6°). These results can be understood since the former set of beams all produces Gaussian like focal intensity profiles, whereas the latter produce annular profiles with a lower peak intensity. In

other words, the drilling properties in the 500μm thick silicon and steel plates are more influenced by the focal intensity distribution than the state of polarization.

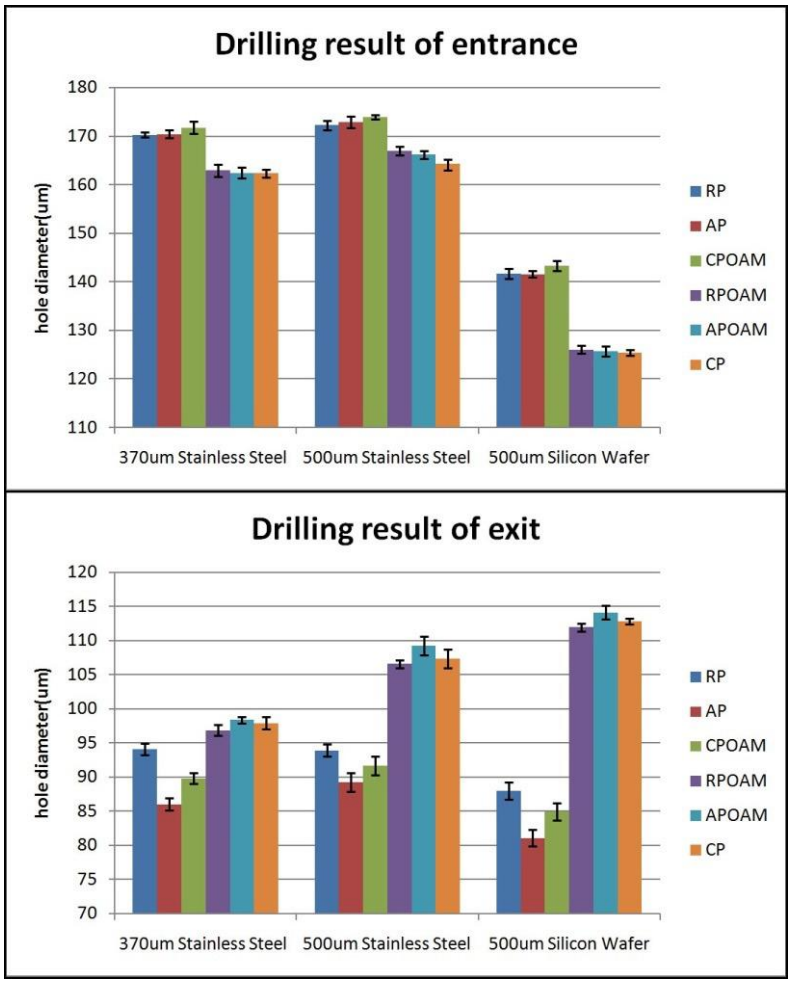

Fig. 5.4 *Data graphs showing drilling hole diameter of entrance(top graph) and exit(bottom graph) on 370um SS sheet(~20s exposure duration), 500um Stainless Steel sheet(~70s exposure duration), 500um Silicon Wafer(-140s exposure duration) with various tailored laser beams.*

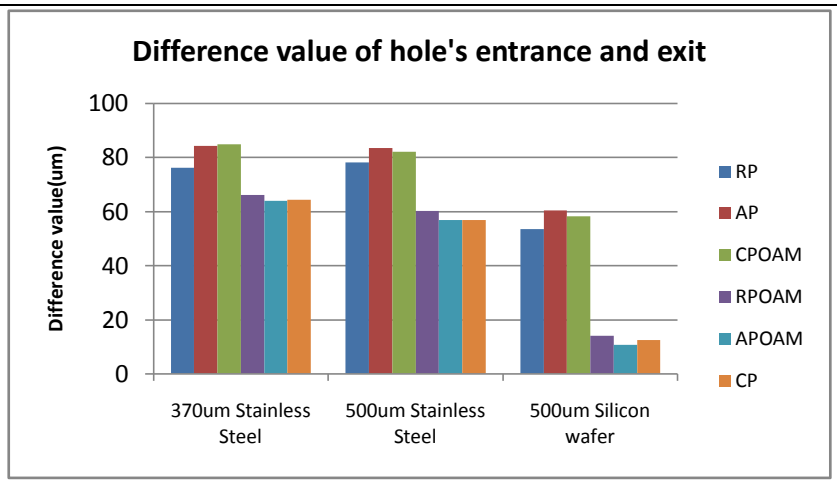

Fig. 5.5 *Data graphs showing the difference value of hole's entrance and exit in Fig.5.4.*

Looking at the drilling results in the 370μm thick stainless steel plate (Fig.5.4), it can be seen that the distinction between the drilling properties of the annular beams (i.e. RP, AP and CPOAM) and those of the Gaussian beams (i.e. RPOAM, APOAM and CP) is less obvious than with the thicker plates. Within the set of annular beams, there is a clear influence of polarization on the diameter of the exit holes. The RP beam produces a ~10% larger exit diameter than the AP beam (~94μm versus ~86μm). This is the result of the better coupling efficiency of radial polarization, which mostly produces ***p***-polarized internal reflections on the sidewalls during drilling [4,115]. On the other hand, azimuthal polarization mostly produces ***s***-polarized internal reflections, with a higher reflectivity that leads to increased losses through the hole exit aperture and thus a poorer coupling efficiency overall. The CPOAM beam produces an intermediate exit hole diameter (~87μm). This results from the average of ***p***- and ***s***-polarized internal reflections during drilling typically the same with circular polarization [116], thus an intermediate coupling

efficiency between that of radial and azimuthal polarization.

Note that the RPOAM and APOAM beams induce a hybrid state of polarization at the focal plane as demonstrated in chapter 4, and thus both produce exit holes with fairly similar diameters, however it still can be seen that the exit holes produced by APOAM is a little bit larger(~1-2%) than RPOAM from Table 5.1 in all case. This can be also considered as most proportion of ***p***-polarization produced by APOAM when near the focal region due to the polarization inversion.

In summary, these results illustrate how the beam vector fields can be tailored to specific applications requirements. By shaping the focal intensity profile and polarization distribution, the machining properties can be optimized for a given process or material. For example for an application requiring holes with reduced taper in 500μm thick silicon wafers (i.e. entrance and exit holes of similar diameter), a drilling process with a APOAM would be most appropriate, since it produces the lowest taper angle.

5.3. Chapter summary

In this Chapter this 5, the Polarization Mode Converter was combined with high laser beam fluence to micro-drill stainless steel and silicon wafer plates. Prior to testing real-time processes, the results were compared in terms of quality and efficiency, illustrateing how the distinct machining properties associated with each static polarization and wavefront, make it best suited for specific processes or materials.

From the whole drilling result, it shown that the laser beams with Gaussian like focal intensity profiles (with OAM) gain much lower sidewall taper than the beams with annular profiles (without OAM), which means drilling hole geometry is more influenced by the focal intensity distribution than the state of polarization. On the other hand, the laser beams carry with radial polarization on the focal plane produced a larger exit diameter up to 10% than the azimuthally polarized beam. This is the result of the better coupling efficiency of radial polarization on the material side walls (P polarization)

All the results illustrate how tailored vector beams can be used to optimize laser micro-processes. The great advantage of the method described here is its flexibility, with an almost infinite range of optical field combinations.

Chapter 6 Investigation of advanced annular beam in micro-processing application

6.1 Introduction

The use of interesting beam shape can make some specific laser micro-fabrication more flexible. For example, the generation of different sized annular beams can be used to obtain optical trepanning drilling, which is more efficient than the traditional mechanical trepanning drilling [7,117,118]. Besides, this annular beam also increased the processing efficiency in selective ablation for semiconductor materials. By using the same setup in previous two chapters, annular beam with various polarization can be obtained, which can be considered as another branch in optical vector field control.

In this chapter, ultrafast laser micro-processing using diffractive annular beam patterns is demonstrated. The annular beam was generated by diffractive axicon computer generated holograms (CGHs) using a SLM. The diameter of the annular beam can be easily adjusted by varying the radius of the spatial period of the axicon phase map. In addition, by combining a S-waveplate in the annular beam setup, the output annular beam polarization can be modified. Micro-holes were drilled through a 0.05mm thick stainless steel foil using the annular beams with various polarization states. Surface processing of various polarized annular beams were also used to produce aconcentric ring array, in which the rings had different polarizations, the patterns give various colour when using diffraction of side light illumination. Furthermore, these annular beams were used in selective ablation of Indium tin

oxide coated on glass substrate(ITO/glass).This approach increased the processing efficiency significantly over that of single beam processing.

6.2 Experimental and methodology

The experimental setup of annular beam micro-processing also used the High Q picosecond laser system in Chapter 4, Fig.4.1.The SLM here applied diffractive axicon CGHs to generate annular beams for the experiment.

Diffractiv eaxicon CGHs, also described as circular blazed gratings, were used to create annular beams. As shown in Fig.6.1, the radius of the smallest ring in the axicon is equal to the spatial period of the blazed grating, *d*. The blazed grating creates a +1 order beam with a diffraction angle of β, while the axicon generates a diffractive +1 order conical wave. According to the grating equation below[119]

$$d(\sin\alpha + \sin\beta) = m\lambda \qquad \text{Eq.6.1}$$

where *d* is the grating period or the radius of smallest ring in the axicon phase, α is the input beam incidence angle, *m* is the diffraction order and λ is the input beam wavelength, when *m* =1,the +1order diffraction angle:

$$\beta \approx \sin\beta = (\lambda / d) - \sin\alpha \qquad \text{Eq.6.2}$$

If keeping a small incident angle, the diffraction angle can be recognized by

$$\beta \approx \left(\lambda / d \right) \qquad \text{Eq.6.3}$$

When the diffracted conical wave is focused by the f-theta lens, an annular focus is created at the focal plane. As shown in Fig.6.2, the diameter (D) of the annular focus can be calculated by

$$D = 2r = 2f\tan\beta \approx 2f\,\beta \approx 2f\ \ \lambda / d \qquad \text{Eq.6.4}$$

where f is the focus of F-theta lens. Since the width of the annular focus is comparable to the 0th order beam waist ($2\omega_0$), the area of the annular (S) focus can be calculated by

$$S \approx 2\omega_0 c = 2\omega_0 \pi D = 4\omega_0 \pi f\ \ \lambda / d \qquad \text{Eq.6.5}$$

where c is the circumference of the annular focus.

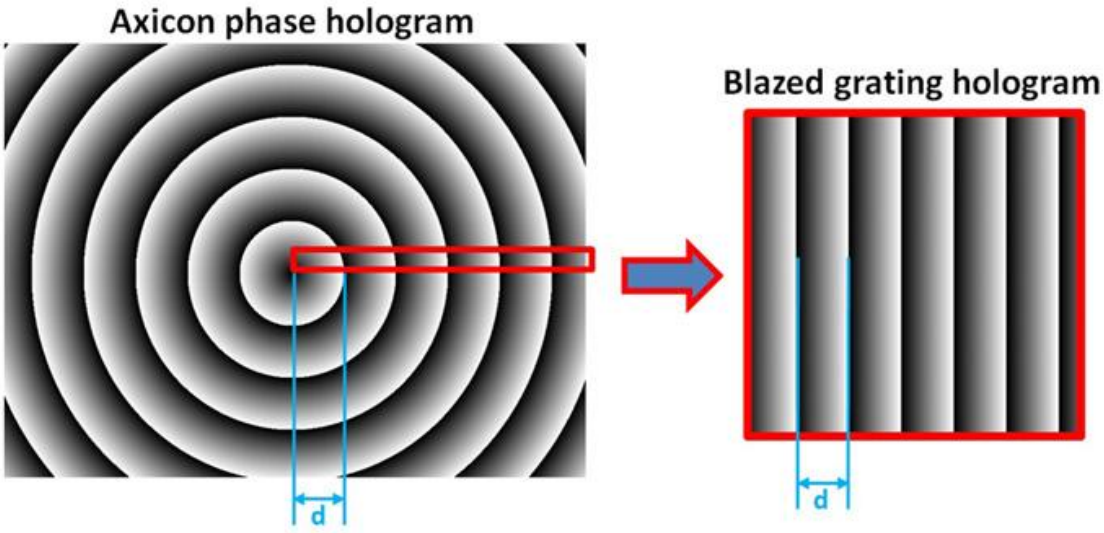

Fig. 6.1 *Diffractive axicon CGH (left) and blazed grating CGH(right).*

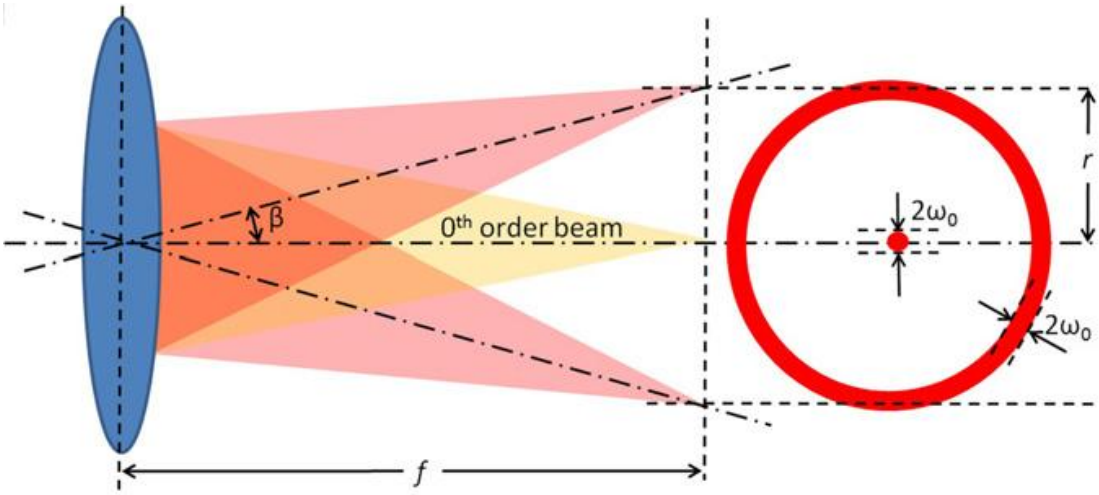

Fig. 6.2 *Annular focus created at the focal plane of the* f *-theta lens.*

During experiments, pulse energy (E_p) were directly measured by an power meter.

Peak fluences (F) for a Gaussian beam single pulsecan be calculated by

$$F = 2E_p / \left(\pi\omega_0^{\,2}\right) \qquad \text{Eq.6.6}$$

where ω_0 is the radius of the Gaussian beam waist. From Eq.6.5 and Eq.6.6,when

processing with single annular beams, the fluence in the ring of width $2\omega_0$ is then,

$$F = E_p d / (2\omega_0 \pi f \ \lambda) \qquad \text{Eq.6.7}$$

6.3 The generation of single annular focus with various polarizations and surface processing analysis

Surface ablation of a stainless steel sample using different sized annular beams created by diffractive axicon CGHs is demonstrated in Fig.6.3. The laser intensity distributions measured by the Spiricon beam profiler are presented in column (b). Each ablation annular footprint shown in the column (c) was fabricated by 100 pulses at fluence $F \approx 0.3$ J cm−2 (approximate 1.5 × ablation threshold). Note that a small circular dot machined by the undiffracted 0th order beam was found in the centre of annual rings, this is due to the diffraction efficiency of SLM is not 100% which leads to the remnant 0th order and also distortion of ring shape. To prevent the 0th order from damaging the sample, it is possible to physically block the 0th order at the Fourier plane of the 4*f* optical system using a small target.

Table 6.1 showing the comparison between theoretical and measured diameter of the annular beam (*D*) against the radius of the spatial period in the axicon CGH (*d*). As plotted in Fig.6.4, the experimental data acquired from measuring the annular

ablation footprint on the stainless steel sample reasonablely matches the theoretical data calculated using Eq.6.4. Note that when *d* is smaller the disparity between the theoretical and measured D is larger, this is due to the limitation of pixel resolution on this SLM which cannot offer smooth gradient change in phase modulation (i.e. when *d*=100, each 2π phase change present in only 5 pixels on SLM which cause steeper gradient between each pixel). when the *d* is larger, due to less blazed rings present in axicon, the annual rings are not quite round.

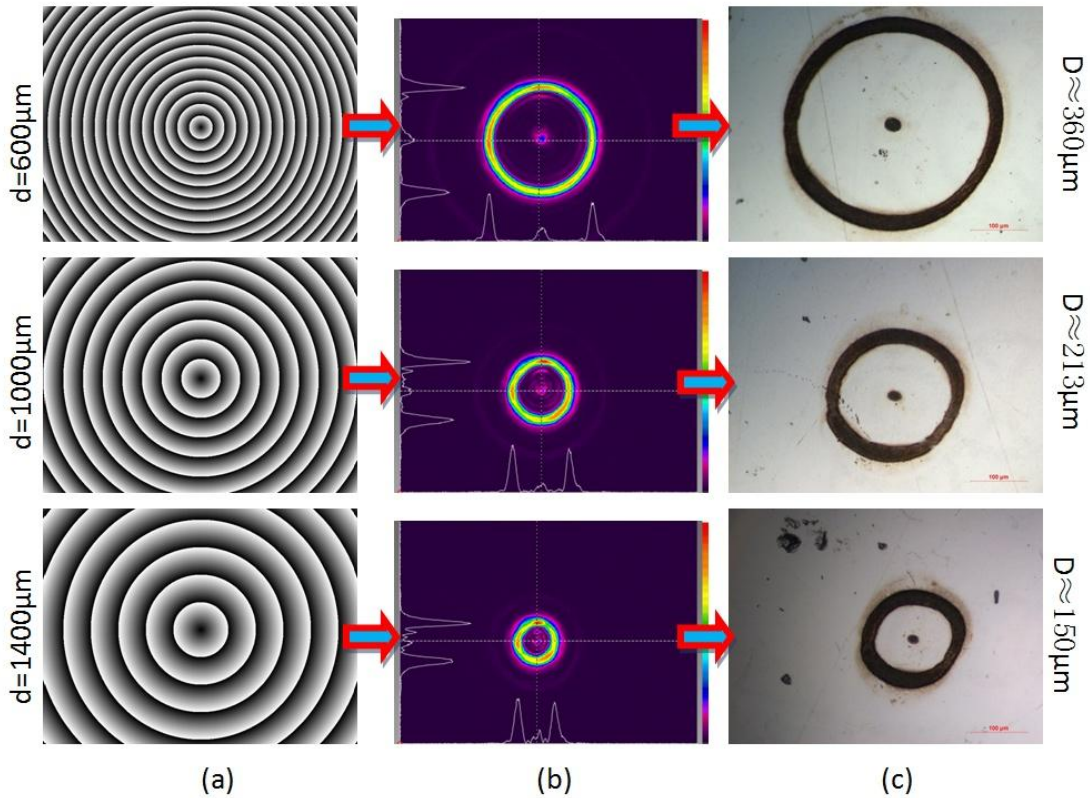

Fig. 6.3 *Single annular beam processing—column (a): diffractive axicon CGHs with different spatial period* d*; column (b): annular beams observed by the Spiricon beam profiler; column (c): optical micrographs showing the annular ablation footprints on a stainless steel sample.*

Table 6.1 Comparison between theoretical and measured diameter of the annular beam.

Spatial period ring in the Axicon phase d (μm)	Theoretical diameter of the annular ring D(μm)	Measured diameter of the annular ring D(μm)
100	2128	2247.4
200	1064	1089.1
400	532	542.3
600	354.6	360.4
800	266	271.2
1000	212.8	213.1
1200	177.3	176.4
1400	152	149.3
1600	133	129.1
1800	118.2	112.3
2000	106.4	100.1

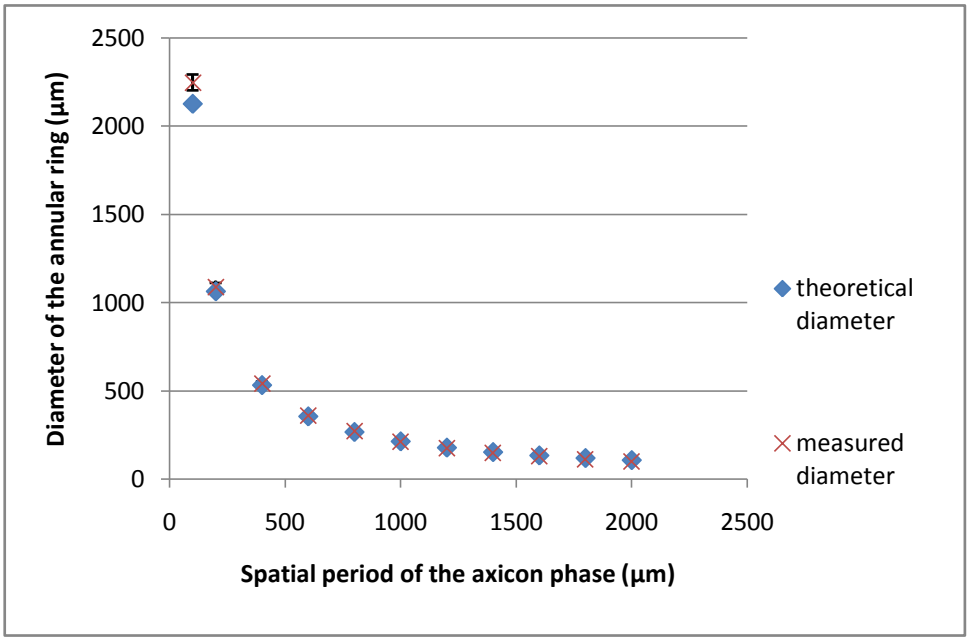

Fig. 6.4 *Graph of comparison between theoretical and measured diameters of annular ring.*

By adding a S-waveplate after the SLM, the annular output beam polarization can be modified to have linear, azimuthal, or radial polarization. This is shown convincingly below in Fig.6.5-Fig.6.7. The intensity beam profiles measured by a Spiricon camera combined with a polarizing filter transmission axis oriented vertically. The azimuthally and radially polarized annular beams present a two lobe shape which are oriented orthogonally, to be expected when an annular beam with these polarization states are analysed.These results are consistent with thoseobserved in Chapter 4 with ring mode radial and azimuthal states. The results of surface structuring also show that the LIPSS directionsin the annular rings in column confirm these polarization states unambiguously.

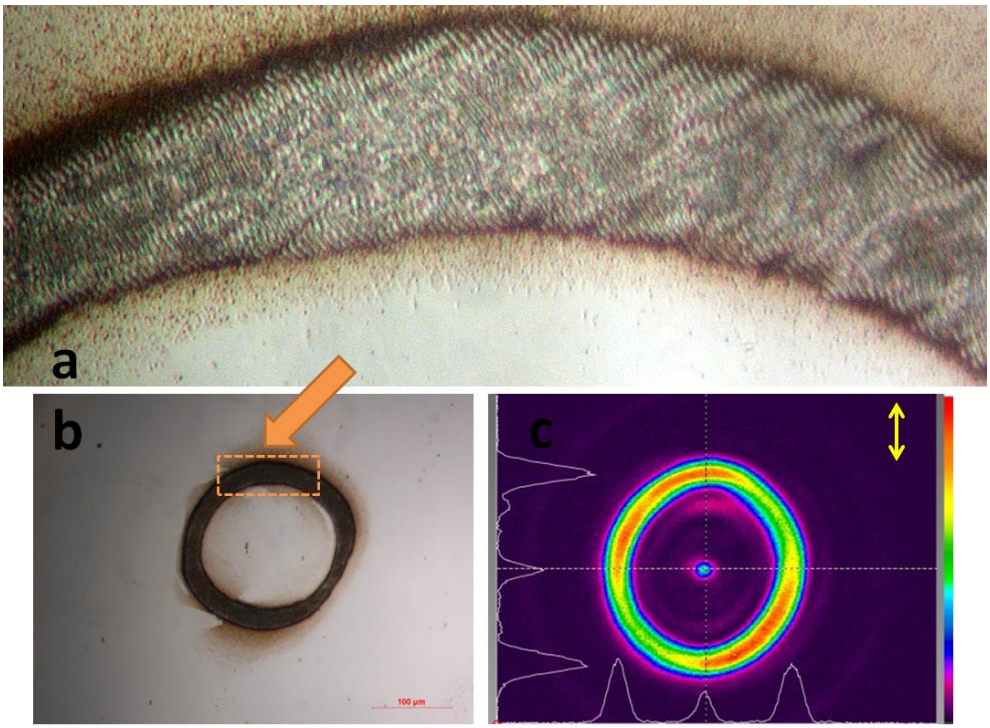

Fig. 6.5 *Linearly polarized annular beam analysis, a) magnified LIPSS pattern from b) footprint of ablation on polished stainless steel surface; c) Spiricon camera beam profile shows the intensity distrubution after the polarizing filter.*

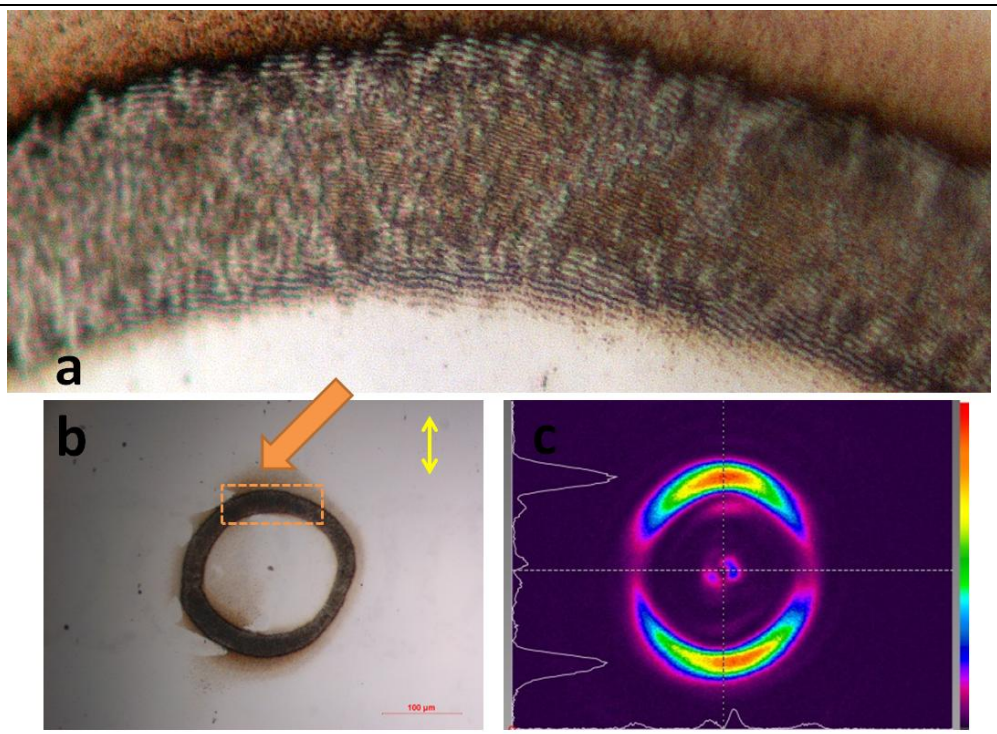

Fig. 6.6 *Radially polarized annular beam analysis, a) magnified LIPSS pattern from b) footprint of ablation on polished stainless steel surface; c) Spiricon camera beam profile shows the intensity distrubution after the polarizing filter.*

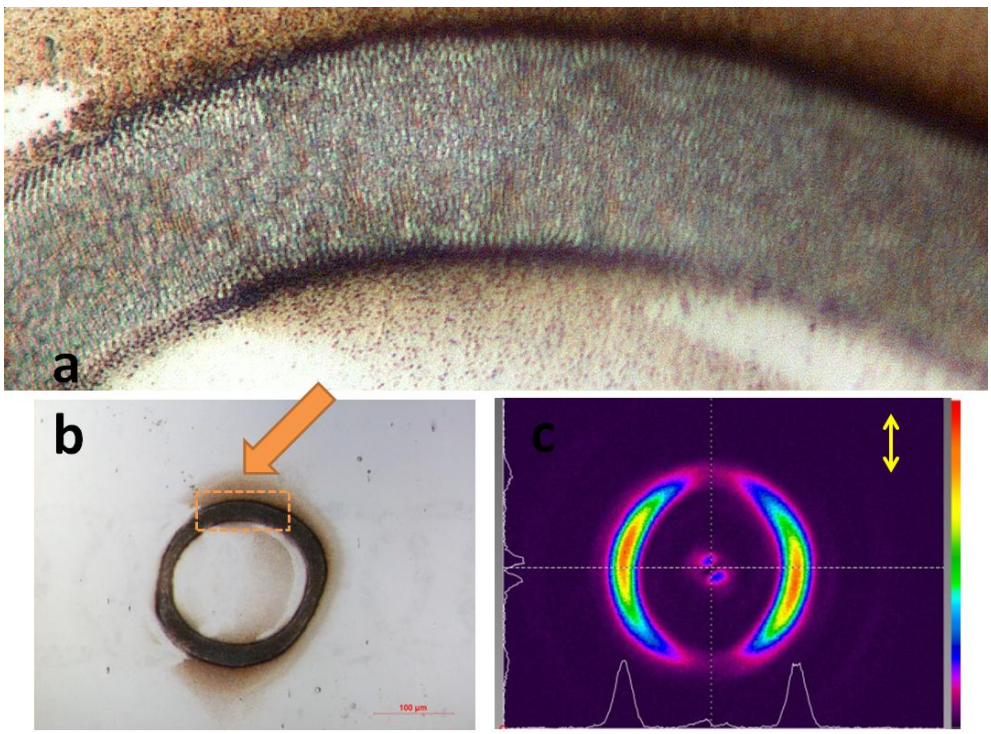

Fig. 6.7 *Azimuthally polarized annular beam analysis, a) magnified LIPSS pattern from b) footprint of ablation on polished stainless steel surface; c) Spiricon camera beam profile shows the intensity distrubution after the polarizing filter.*

Then The annular beams were used to drill holes with different polarization state through a 0.05mm thick stainless steel foil, using optical trepanning drilling [15, 16]. The laser beam was focused on the upper surface of the stainless steel foil. Since the thickness of the stainless steel foil (~50μm) is comparable to the depth of focus of the *f* -theta lens, there is no need to adjust the focal position when the laser is drilling through the foil. No processing gases were used during the experiment. As shown in Fig.6.8, drilling through the foil sample with 4 different polarized annular beams (d=1200um, D≈170um),was performed with 10000 pulses(5kHz, in 2 second) at a fluence of $F \approx 0.8$ J cm^{-2}. Fig.6.8 shows the observed entrance and exit hole diameters for comparison, one can see that the linear polarized annular beam gives the worst drilling result with elliptical entrance/exit holes. From Fig.6.9, as the radial polarized annular beam gives a P-polarization at the drilled hole wall all around the ring, hence higher absorption coefficient, it gives the largest exit diameter (D≈185um). In contrast, azmuthally polarized annular beam gives S-polarization at drilled hole wall around the ring, the absorption coefficient is lower, which gives a smaller exit(D≈175um).

In addition, comparing with annular beam drilling, when using single Gaussian beam with the same fluence ($F \approx 0.8$ J cm^{-2}) to machine this stainless steel foil by mechanical trepanning drilling, the processing time will take at least 30 second. Hence the processing speed for annular beam is 15 times faster than single Gaussian

beam in this case.

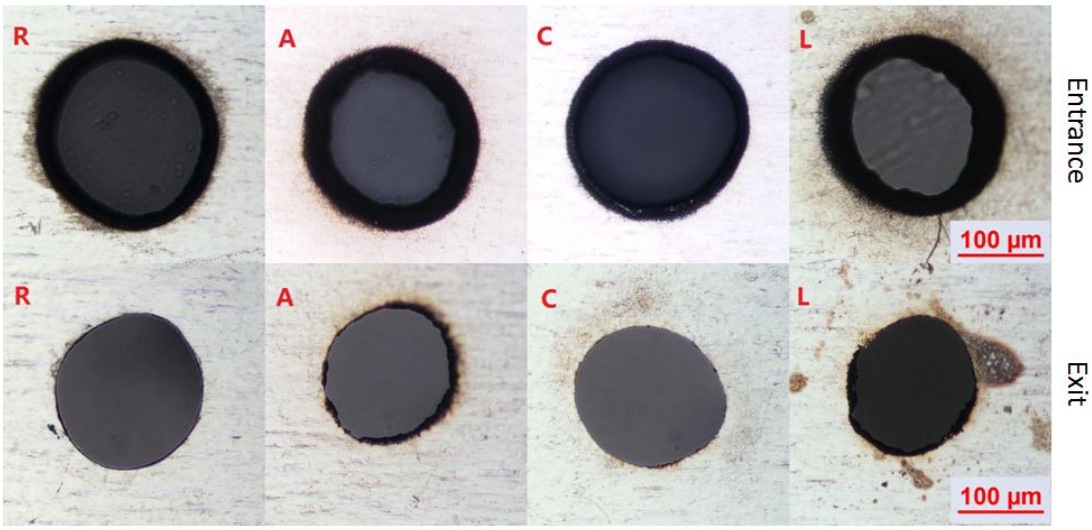

Fig. 6.8 *Microscope images of comparison between radially (R), azimuthally (A),linearly (L), circularly (C) polarized annular of drilling entrance and exit on stainless steel foil.*

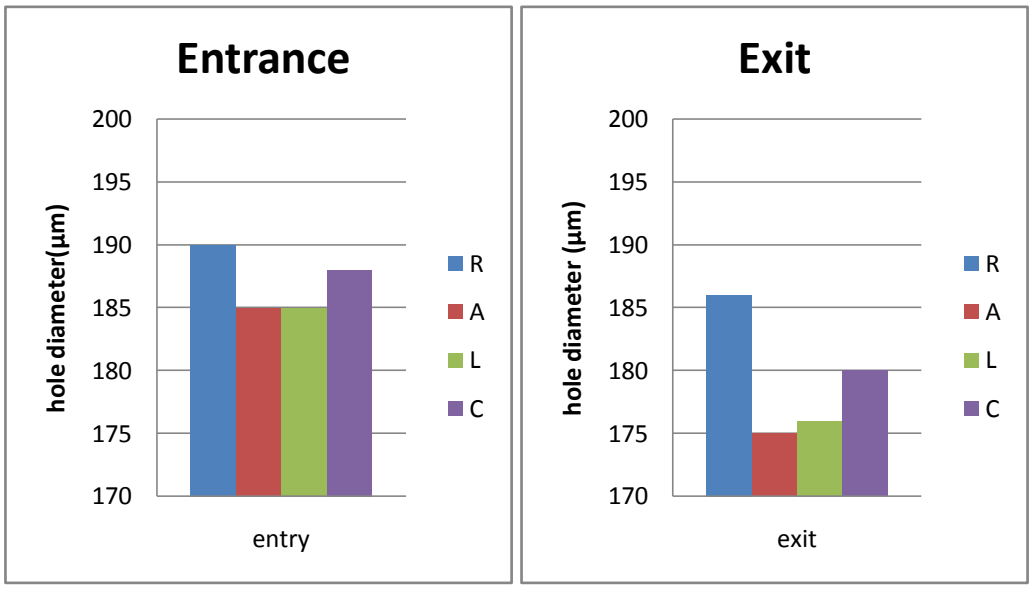

Fig. 6.9 *Graph of comparison between radially (R), azimuthally (A),linearly (L), circularly (C) polarized annular of drilling entrance and exit on stainless steel foil.*

6.4 Complex surface patterning on polished stainless steel

By synchronizing these two parameters with laser gating, a complex LIPSS ring pattern can be achieved.Fig.6.10-Fig.6.12 show several concentric rings produced by linearly, azimuthally and radially polarized annular beams by adjusting the axicon spatial period *d* on polished Stainless Steel sample. The polarization states of these beam are also easily visualized using low-angle side illumination. After cleaning, these concentric rings were observed by the microscope with side light illumination (white light, unpolarized) at grazing incidence. Due to the diffractive property of LIPSS [70], only the areas where LIPSS are perpendicular to the axis of illumination reflected the low angle light. Therefore, each pattern shows the part of the geometry that reflected the illumination through diffraction of the LIPSS. Rotating the axis of illumination by 90° reveals the remainder of the geometry.

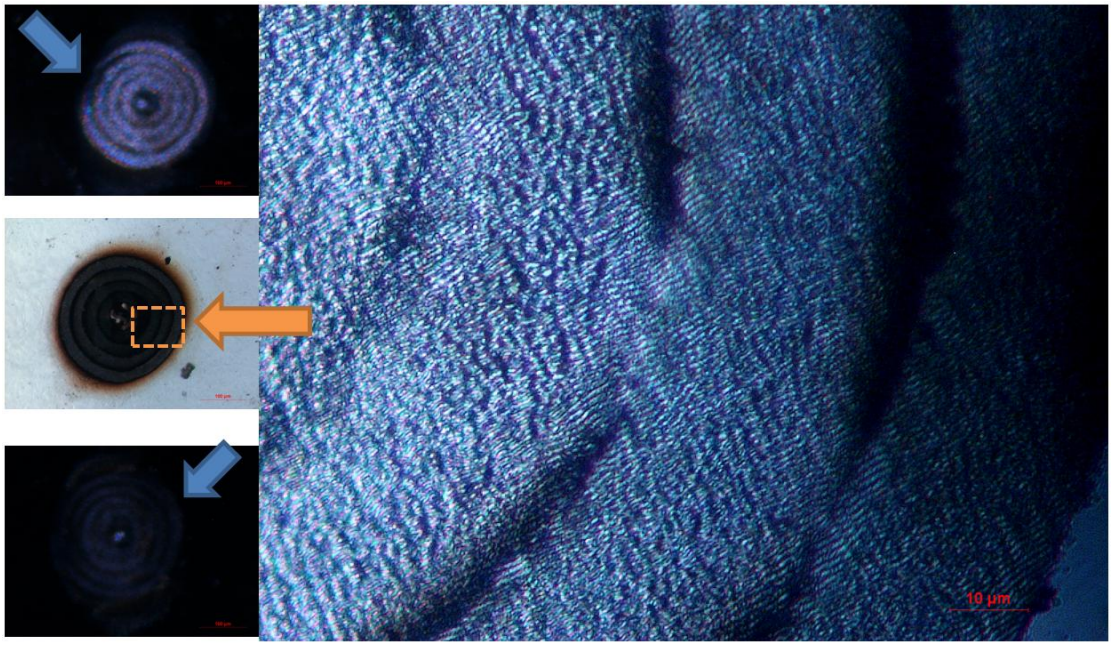

Fig. 6.10 *Concentric rings LIPSS machined by linearly polarized annular beams at side light illumination(blue arrow indicated the direction of incidentside light); magnified image shows the LIPSS direction.*

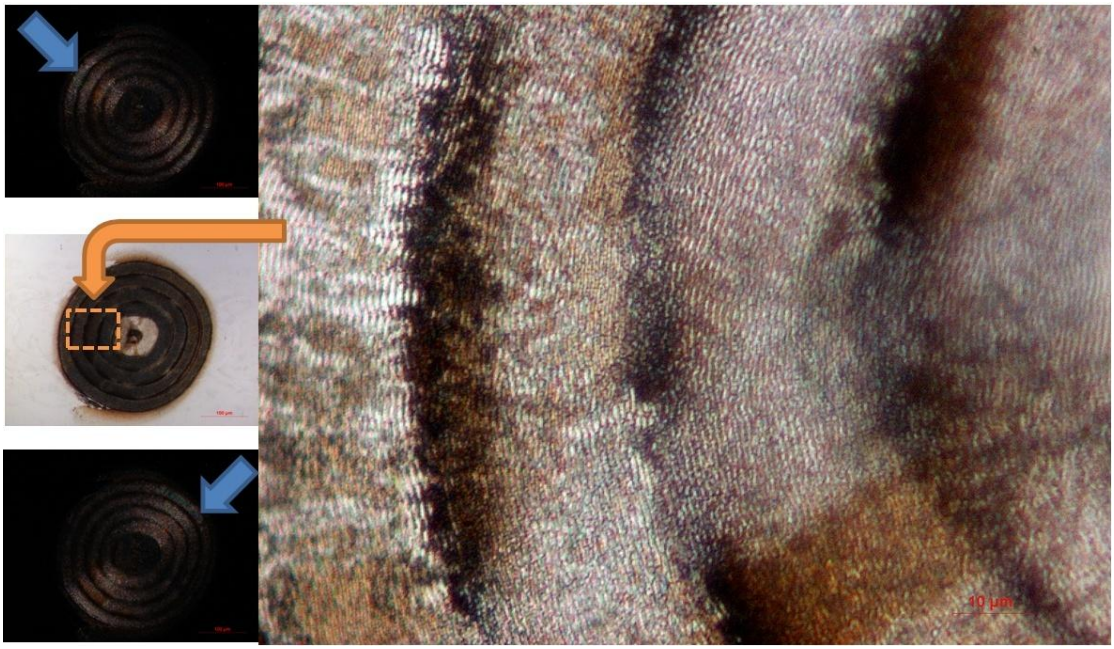

Fig. 6.11 *Concentric rings LIPSS machined by radially polarized annular beams at side light illumination(blue arrow indicated the direction of incident side light); magnified image shows the LIPSS direction.*

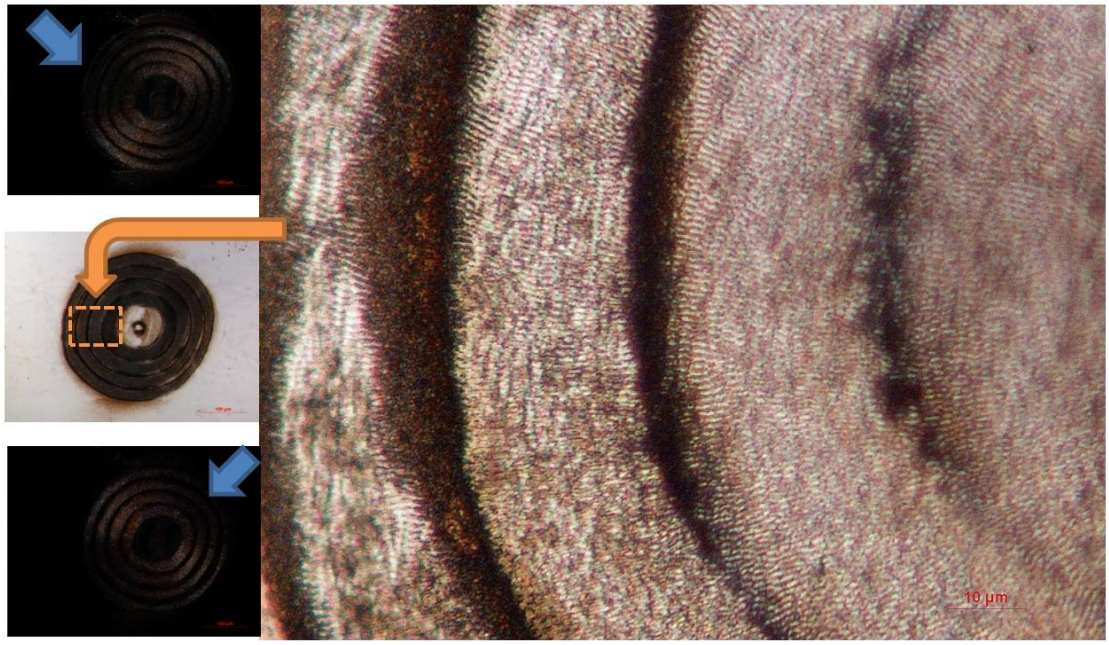

Fig. 6.12 *Concentric rings LIPSS machined by azimuthally polarized annular beams at side light illumination(blue arrow indicated the direction of incident side light); magnified image shows the LIPSS direction.*

Linear polarization shows a high contrast, expected when light is diffracted from the LIPSS when oriented 90° to incident light direction (Fig.6.10, top left). With radial polarization the diffracted light is mainly at ±45°, appearing in those regions where the LIPSS are parallel to the incident light (Fig.6.11). The results with azimuthal polarization (Fig.6.12), as expected are opposite to those with radial one.

Using this approach, a 4x6 concentric rings array were generated, and also at two orthogonal side light illumination (see Fig.6.13). All these arrays show the uniformed diffractive patterns.

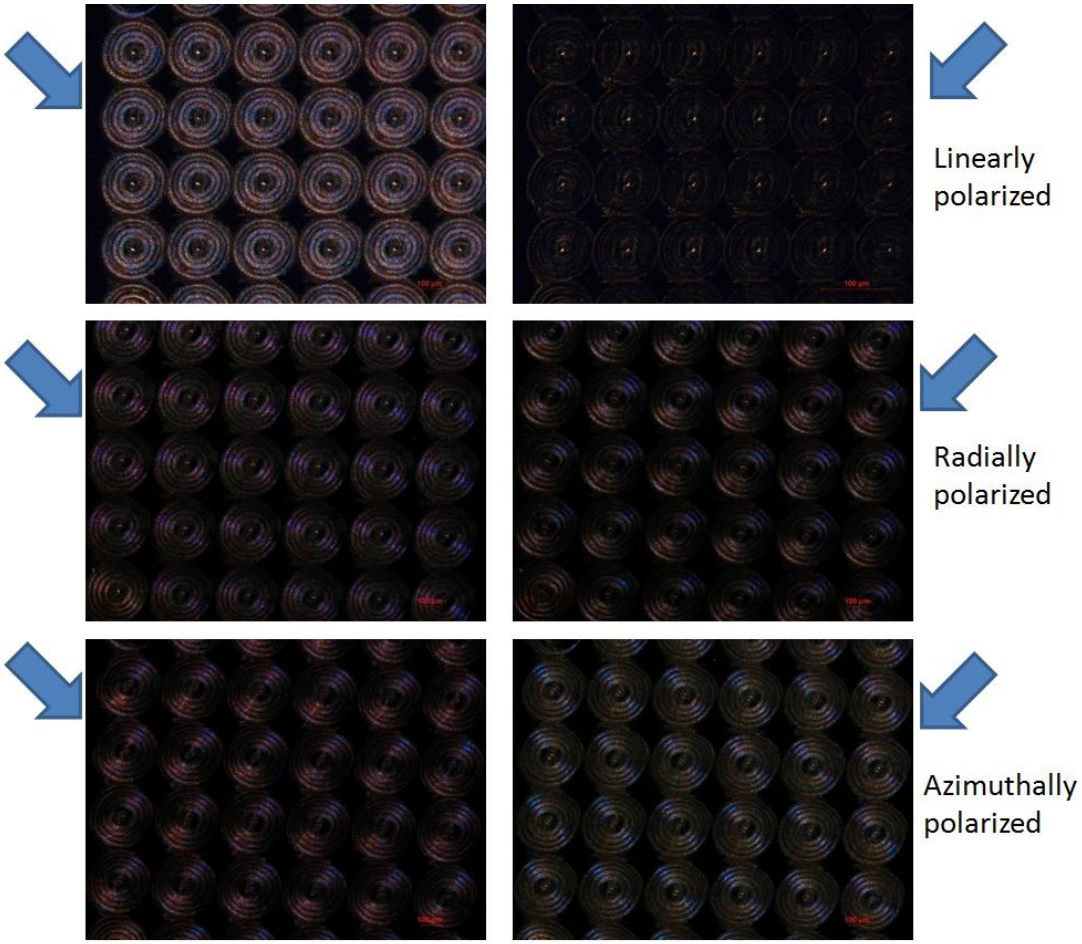

Fig. 6.13 *4x6 concentric rings array were produced by linearly, radially, azimuhally polarized annular beam at two orthogonal side light illumination (blue arrow indicated the direction of incident side light).*

The polarization of annular beam can be easily changed by rotating the S-waveplate transmission axis, when synchronizing polarization with motion control and axicon CGHs, this allowed dynamic complex plasmon structuring on the substrate. Fig.6.14 shows the concentric rings with mixed radially and azimuthally polarized annular beam. This special illumination property gives a potential application in the security data coding, follow the side light direction radial annular rings would appear bright stripes and dark stripes for azimuthal annular rings. For the bright stripe can contain digital code 1, dark stripe can contain digital code 0. Side illumination on concentric

rings can be read by a sensor which would recognize the 0,1 digital code. Using this approach, a 4x6 concentric rings array were generated at two orthogonal side light illumination in Fig.6.15. Due to only the areas where LIPSS are perpendicular to the axis of illumination reflected the low angle light, in Fig.6.15, the bright segments in left image will appear dark shadow in right image by orthogonal side light illumination.

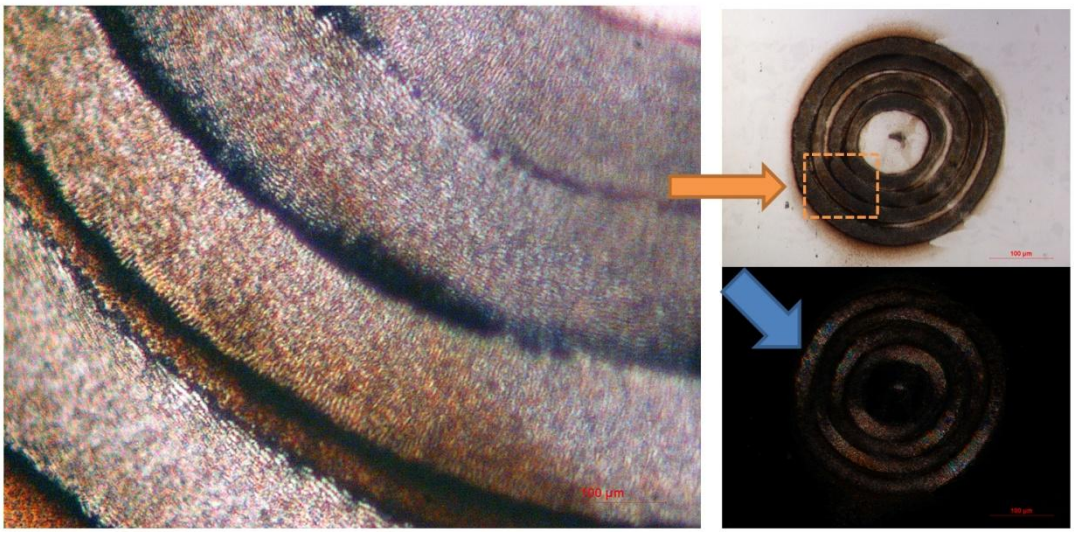

Fig. 6.14 *Concentric rings LIPSS machined by mixed radially and azimuthally polarized annular beams at side light illumination(blue arrow indicated the direction of incident side light); magnified image shows the LIPSS direction.*

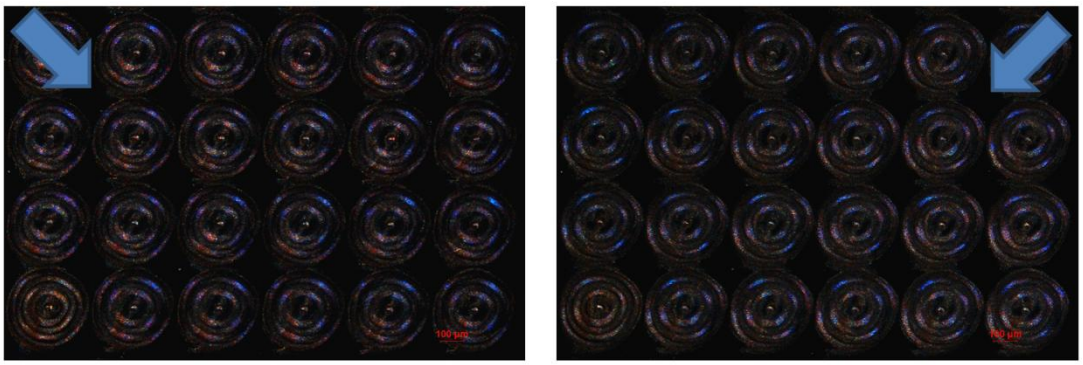

Fig. 6.15 *4x6 concentric rings array were produced by mixed radially and azimuthally polarized annular beams at side light illumination(blue arrow indicated the direction of incident side light).*

6.5 Surface processing on ITO

Transparent Conductive Oxides (TCO) materials are electrically conducting and transparent to visible light have undergone continuous development. Indium Tin Oxide (Sn-doped In_2O_3), also known as ITO, is a commonly used TCO material. has become very popular with manufacturers due to its excellent conductivity, wide optical transmission and stability in most environments.

In semiconductor manufacturing there is a requirement to be able to fabricate large numbers of devices in short time. For the selective ablation on ITO substrate, if a wider track of removal area is required on ITO, the traditional method would scan the Gaussian beam over several overlapping tracks to achieve the required width. Here then is an advantage of using the annular beam, as the diameter of the annular ring can be adjusted by the Axicon CGH to achieve the required width, hence only one scanned track is needed which reduces the processing time.

Fig.6.16 and Fig.6.17 show a comparison between annular beam and single Gaussian beam for material removal on ITO sample to produce a ～210μm track in 5mm length, used same fluence F= 0.9J/cm^2 and scanning speed 10mm/s in both case. The experimental results were observed by WYKO NT1100 white light interferometric microscope. An annular beam with 210μm diameter was used to ablate the ITO surface with a single scan in 0.5 second, the processing result is

nearly perfect in the ablated area with smooth finish (Fig.6.16). On the right-hand side, a single Gaussian beam(~30μm beam width) did the multi-scan with a 15μm hatch, hence there were 15 small tracks combined together to achieve 210μm track width, finished the process in 7.5 second (Fig.6.17). The ablated track by single Gaussian beam multiple scan clearly shows the tips structure in each overlapping scanning path, this is due to the overlapping hatch distance 15μm still a little bit wider. To solve this issue, it need reduce the value of overlapping hatch, which cause more scan numbers and deduction of processing efficiency. Hence the annular beam shows the advantage of process in higher quality and efficiency in this case.

Using the same approach, a complex pattern were produced by annular beam selective ablation on ITO/glass(see Fig.6.18). The cross-section of each slot in ablation area gain the fairly same width (~215μm) and depth (~20μm), which offers a good uniformity in this pattern. This surface analysis of WYKO interferometer shows high quality ablation avoiding damage to the substrate.

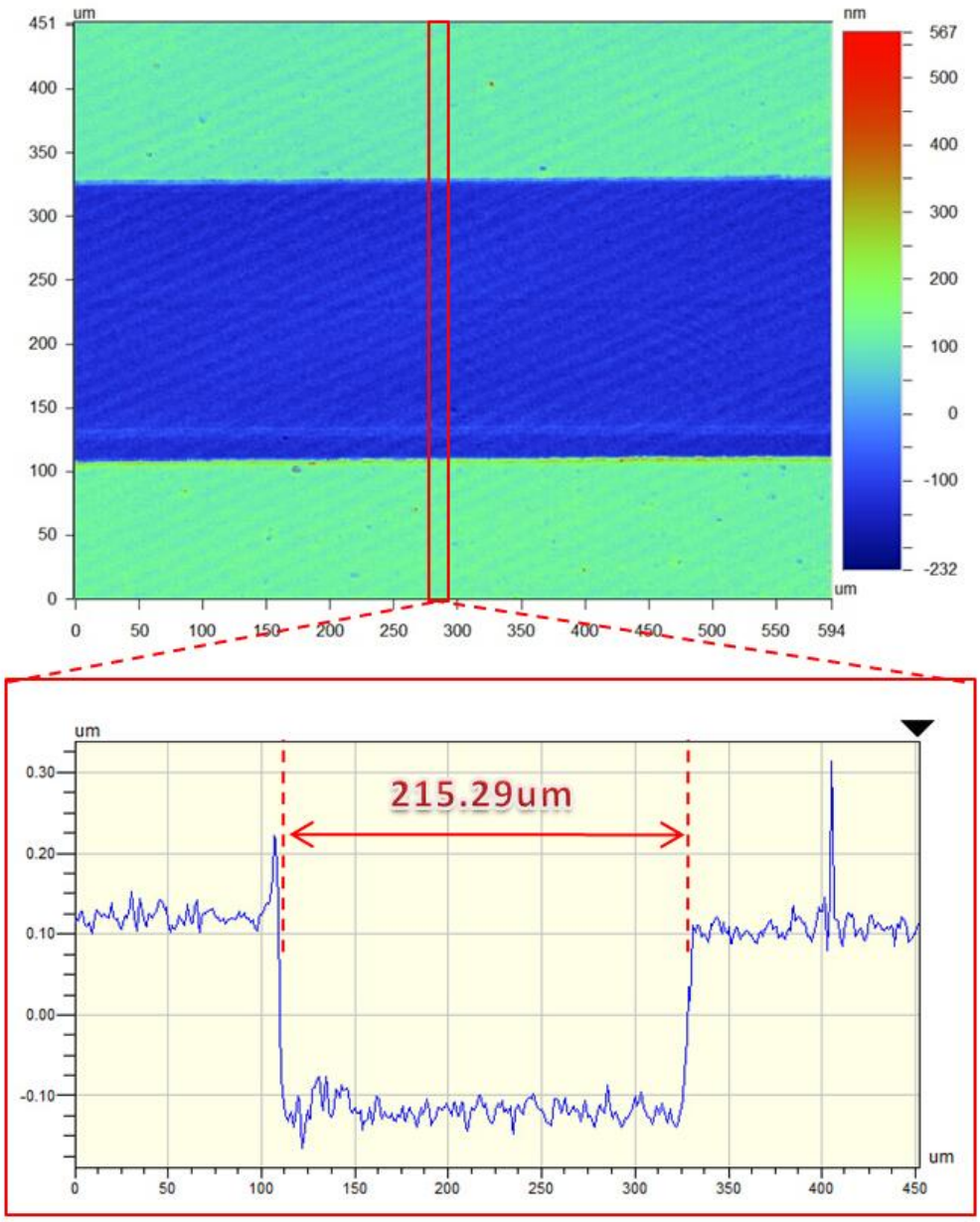

Fig. 6.16 *interferometric microscope image shows ITO sample machined by Annular beam with single scans (top); cross-sectional profile of track analysis in Y axis(bottom).*

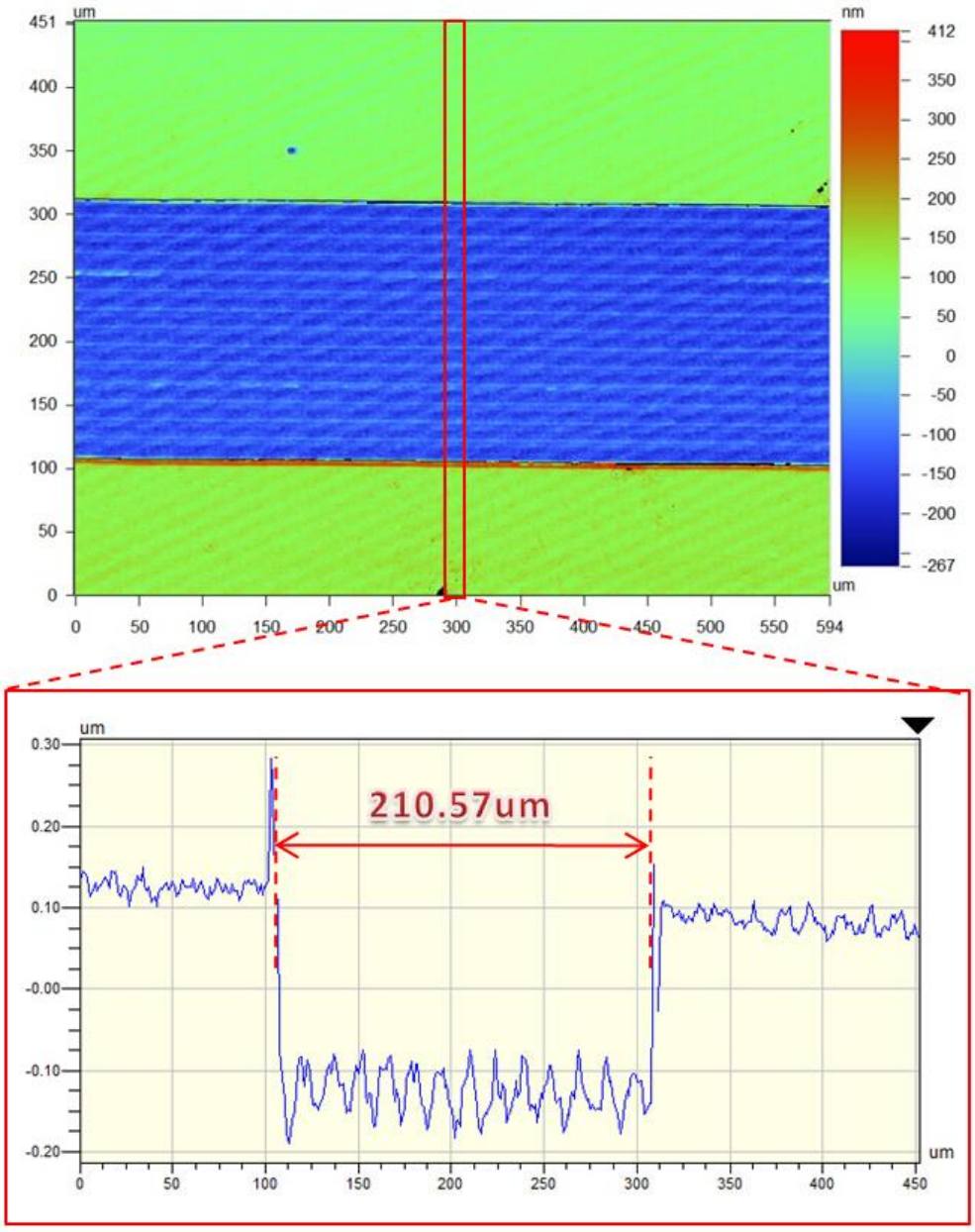

Fig. 6.17 *interferometric microscope image shows ITO sample machined by single Gaussian beam with 15 scans (top); cross-sectional profile of track analysis in Y axis(bottom).*

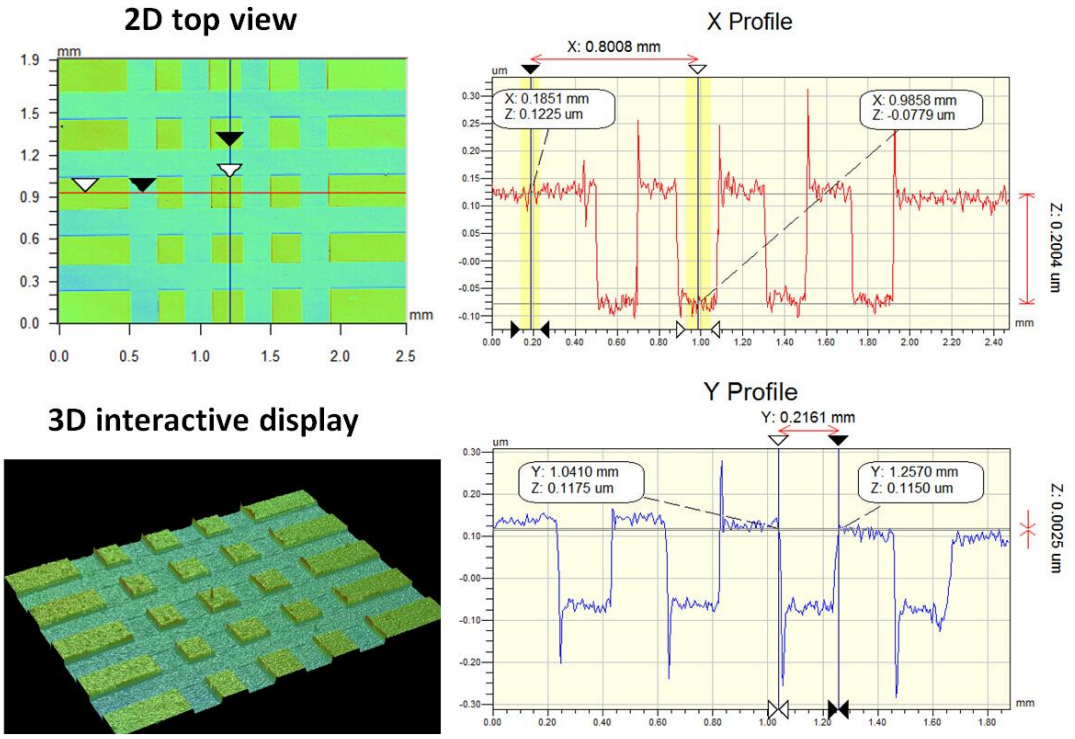

Fig. 6.18 *WYKO interferometer analysis of selective ablated pattern machined by Annular beam.*

6.7 Chapter summary

In this Chapter, ultrafast laser micro-processing using annular beams generated by diffractive axicon patterns is demonstrated. The diameter of the annular beam is adjustable by controlling the spatial period of axicon CGHs, which would be considered as an advanced beam shaping technique in order to improve the processing efficiency and flexibility.

By combining a S-waveplate in the annular beam setup, the output annular beam polarization was modified. Micro-holes were drilled through a 0.05mm thick stainless steel foil using the annular beams with various polarization states. Due to

the advantage of annular property, and avoiding high laser output attenuation the processing speed could be at least 15 times faster than with the normal Gaussian beam. In addition, as the annular beam with radial polarization gives a P-polarization at the drilled hole wall all around the ring, hence higher absorption coefficient, it gives the largest exit diameter in the drilling result. This is also consistant with the drilling results which shows the significant advantage of using radial polarization in laser micro-processing.

The polarization of annular beam can be easily changed by rotating the S-waveplate transmission axis while the diameter of the annular ring is determined by Axicon dimension, d set by the CGH. By synchronizing these two parameters with laser gating, a complex concentric LIPSS ring pattern can be achieved. Due to the diffractive property of LIPSS, each pattern gives a different light and shade appearance. Follow the side light illumination radial annular rings would appear as bright stripes and dark stripes for azimuthal annular rings. This unique technique has a potential application in the security data coding. For instance, the bright stripe can represent digital code 1 and dark stripe for code 0. Then side illumination on a series of concentric rings can be read by a sensor if the proper setup is used.

Adjustable diameter annular beam was also used in selective ablation on ITO /glass substrate, Scanning the annular beam with appropriate fluence was much more

satisfactory than using a Gaussian being which required severe attenuation to avoid substrate damage. For Gaussian beam, traditional method needs many overlapping scanns to achieve the required width, while only one scanned track is needed for annular beam by adjusting the diameter equal the track width while using much higher pulse energy. The processing result is nearly perfect for annular beam increasing the processing speed by factor of 15 Using this approach, complex, high speed patterning of ITO on glass can be achieved while showing a high quality finish and avoiding damage to the substrate.

Chapter 7 Conclusions and recommendation for future work

7.1 Conclusions

In this thesis, novel optical setups were designed to control the phase and polarization of ultrashort-pulse laser beams to create complex vector optical fields. This was achieved by using a phase only spatial light modulator and nano-structured S waveplate and combining these with a high repetition rate picosecond laser system operating at 1064nm.

In Chapter 4, the factors of generating highly advanced vector laser beams has been elucidated. Plane wave radial and azimuthal polarizations and their superpositions, logarithmic spirals (RP, AP and IP respectively) were created, which carried stationary vector fields so that local polarization direction is an invariant property as the beam propagates along the optic axis of a low NA focusing lens. when a vortex phase was applied with topological charge m=1 adding orbital angular momentum to these beams, non-stationary vector field results and beam propagation in the region around the focal plane, shows a twisting profile with non-zero intensity at the centre. Surface processing of LIPSS pattern by these tailored beams confirmed this phenomenon and theoretical Jones vector analysis gives a proper explanation. Complex logarithmic spiral LIPSS structures were created, which are the first experimental observations of such spiral vector fields, and theoretically modelled with satisfactory results.

In Chapter 5, it has shown how tailoring vector beams enables to accurately control the focal fields of ultrashort-pulse laser beams and influence their micromachining properties. The resultant vector beams were used for micro-drilling, showing how the intensity profile and state of polarization in the focal plane influence the processing speed and quality. For instance, the laser beams carry with radial polarization on the focal plane produced a larger exit diameter up to 10% than the azimuthally polarized beam. In addition, the polarized beams with vortex wavefront (Gaussian like intensity distribution) produced a lower taper of the hole's geometry than the planar wavefront (donut like intensity distribution). These results illustrate how tailored vector beams can be used to optimize laser micro-processes. The great advantage of the method described here is its flexibility, with an almost infinite range of optical field combinations which helps identify the optimized operating parameters in various applications.

In Chapter 6, ultrafast laser micro-processing using annular beams generated by diffractive axicon patterns is demonstrated, which would be considered as an advanced beam shaping technique in order to improve the processing efficiency and flexibility. Results shown the annular beam with radial polarization gives the largest exit diameter in the drilling through 0.05 thick stainless steel foil, which is also consistant with the drilling results in Chapter 5. A complex concentric LIPSS ring patterns were achieved by synchronizing annular beam's diameter and polarization

state. This unique technique has a potential application in the security data coding. Adjustable diameter annular beam was also used in selective ablation on ITO /glass substrate, Scanning the annular beam with appropriate fluence was much more satisfactory than using a Gaussian being and also increasing the processing speed by factor of 15. Using this approach, complex, high speed patterning of ITO on glass can be achieved while showing a high quality finish and avoiding damage to the substrate.

7.2 Recommendation for future work

The following recommendations for further research have arisen from the work in this thesis:

7.2.1 Optical aberration correction

In the experimental results, slight optical aberrations affected the quality of laser micro-processing. For example, the laser beam was not a perfect Gaussian (M^2 ~1.3), so that a higher beam quality laser source would reduce this source of wavefront aberration. In addition, optical aberration due to the flatness of the SLM used in the experiments induced residual phase distortions.

When a OAM applied by the SLM, the vortex phase produced a singularity at the optical axis, the pixels of the SLM that were very close to this central phase singularity induced significant diffraction effect, this affected the focusing properties of the CVBs and polarization purity as well. Future work could look at using a second SLM in the set-up, which induces a corrective phase pattern designed to compensate the residual phase aberrations on the first SLM.

When generated the annular beam by CGH axicon, the gradient change of grey level in a blazed grating is limited by the SLM pixel number, which cannot provide a full phase modulation in a single spatial period. This affected the diffraction efficiency of axicon phase hologram which leads to the remnant 0th order in the centre of annular ring and also distortion of ring shape. A potential future work could use a SLM with higher pixel resolution to improve the diffraction efficiency of axicon phase, hence a better ring shape. In addition, using a small target properly located at the Fourier plane of the 4f optical system to physically block the 0th order would be recommended.

7.2.2 Industrial processing with CVBs

In a laser micro-processing setup, the focal intensity distribution (i.e. the size and shape of the focused laser spot) and state of polarization are of great importance as it

impacts on the quality and efficiency of the process. As described in this thesis, CVBs have specific properties which influence the micro-drilling results. Various industries require production of high-aspect-ratio structures such as vias or channels, advanced helical drilling can be applied by using appropriate CVBs to optimize the coupling of laser beam energy. Synchronizing the motion of the work piece, this allows adjustment of focal position during processing which could improve the energy penetration, hence higher process efficiency and quality could be achievable.

7.2.3 Cylindrical vector beams in high NA focusing applications

In this thesis research, all the experiments are based on the low NA focusing of CV beams, the further research work can be explored in the high NA focusing of CV beams. As described in the literature review, the radially polarized beams focused with high numerical aperture optics lead to strong longitudinal electric fields, which would be implemented in many applications, including particle acceleration, high capacity optical recording, near-field microscopy, optical trapping of metallic particles, and second-harmonic generation.

7.2.4 Parallel processing using multiple annular beams

As described in Chapter 6, the generation of different sized annular beams can be

used to obtain optical trepanning drilling, which is more efficient than the traditional mechanical trepanning drilling. For further improvement of processing efficiency, multiple annular beams with arbitrary arrangement can be achievable by superimposing an axicon CGH and a grating and lenses algorithm calculated multi-beam CGH. In theory, if the laser source has higher enough power, by using this approach, the full laser output can be fully used without any attenuation which is ideal in a real industrial situation.

7.2.5 Surface LIPSS pattern in information encoding application

The optical diffractive property of LIPSS could be a key feature in a secure data encoding application. The unique designed LIPSS patterns, difficult to copy, may have great potential in the security marking industry for high value products, especially as complex polarizations were synchronized with scanning on a material surface. With such a highly flexible, real time laser polarization state encoding, each product can contain individual, unique LIPSS patterns difficult to counterfeit. Future work could develop this data encoding further and demonstrate decoding using an appropriate optical sensor technique.

References

[1] Kraus, M., Ahmed, M., Michalowski, A., Voss, A., Weber, R. and Graf, T. (2010). Microdrilling in steel using ultrashort pulsed laser beams with radial and azimuthal polarization. Opt. Express, 18(21), p.22305.

[2] Lou, K., Qian, S., Ren, Z., Tu, C., Li, Y. and Wang, H. (2013). Femtosecond Laser Processing by Using Patterned Vector Optical Fields. Sci. Rep., 3.

[3] Lerman, G. and Levy, U. (2008). Effect of radial polarization and apodization on spot size under tight focusing conditions. Opt. Express, 16(7), p.4567.

[4] Weber, R., Michalowski, A., Abdou-Ahmed, M., Onuseit, V., Rominger, V., Kraus, M. and Graf, T. (2011). Effects of Radial and Tangential Polarization in Laser Material Processing. Physics Procedia, 12, pp.21-30.

[5] Marrucci, L., Manzo, C. and Paparo, D. (2006). Optical Spin-to-Orbital Angular Momentum Conversion in Inhomogeneous Anisotropic Media. Phys. Rev. Lett., 96(16).

[6] Hamazaki, J., Morita, R., Chujo, K., Kobayashi, Y., Tanda, S. and Omatsu, T. (2010). Optical-vortex laser ablation. Opt. Express, 18(3), p.2144.

[7] Zeng, D., Latham, W. and Kar, A. (2006). Characteristic analysis of a refractive axicon system for optical trepanning. Optical Engineering, 45(9), p.094302.

[8] Kuang, Z., Perrie, W., Edwardson, S., Fearon, E. and Dearden, G. (2014). Ultrafast laser parallel microdrilling using multiple annular beams generated by a spatial light modulator. Journal of Physics D: Applied Physics, 47(11), p.115501.

[9] MAIMAN, T. (1960). Stimulated Optical Radiation in Ruby. Nature, 187(4736), pp.493-494.

[10] O'Neill, F. (1972). Picosecond pulses from a passively mode-locked cw dye laser. Optics Communications, 6(4), pp.360-363.

[11] Dietel, W., Döpel, E., Kühlke, D. and Wilhelmi, B. (1982). Pulses in the femtosecond range from a cw dye ring laser in the colliding pulse mode-locking (CPM) regime with down-chirp. Optics Communications, 43(6), pp.433-436.

[12] Klopotek, P., Burghardt, B. and Muckenheim, W. (1987). Short pulses from excimer lasers. J. Phys. E: Sci. Instrum., 20(10), pp.1269-1270.

[13] Ostendorf, A., Bauer, T., Korte, K., Howorth, J., Momma, C., Rizvi, N., Saviot, F., Salin, F. (2002). Development of an industrial femtosecond laser micro-machining system, Proc. SPIE 4633, 128-135

[14] Lamb, W. (1964). Theory of an Optical Maser. Phys. Rev., 134(6A), pp.A1429-A1450.

[15] Hargrove, L., Fork, R. and Pollack, M. (1964). Locking of HeNe Laser Modes Induced by Synchronous Intracavity Modulation Appl. Phys. Lett., 5(1), p.4.

[16] Cavalieri, A. (2010). Beyond ultrafast. Physics World, 23(05), pp.47-51.

[17] Krueger, A. (2004). Getting Practical. SPIE Newsroom.

[18] Strickland, D. and Mourou, G. (1985). Compression of amplified chirped optical pulses. Optics Communications, 56(3), pp.219-221.

[19] Image taken from University of Michigan, dept of engineering. [Cited Oct.2015; available at: http://cuos.engin.umich.edu/researchgroups/hfs/facilities/chirped-pulse-amplification/]

[20] Dausinger, F., Hügel, H., Konov, V. (2002). Micro-machining with Ultra-short Laser Pulses, from Basic Understanding to Technical Application. International Conference of Advanced Laser Technologies 2002,Adelboden, Switzerland, ALT-0221

[21] Dausinger, F. (2003). Machining of Metals with Ultrashort Laser Pulses: Fundamental Aspects and Their Consequences. International Conference of Lasers and Electrooptics 2003, Munich, Germany, CK5-1-FRI.23

[22] Murray, J. and Lowdermilk, W. (1980). ND : YAG regenerative amplifier. J. Appl. Phys., 51(7), p.3548.25

[23] Lin, L., Ouyang, B., Li, S., Ge, W., Kang, Y. and Chen, S. (1991). A compact subnanosecond high power Nd:YAG laser system. Optical and Quantum Electronics, 23(3), pp.433-438.

[24] Ruggiero, A., Scherer, N., Mitchell, G., Fleming, G. and Hogan, J. (1991). Regenerative amplification of picosecond pulses in Nd:YAG at repetition rates in the 100-kHz range. Journal of the Optical Society of America B, 8(10), p.2061.28

[25] Walker, D., Flood, C., van Driel, H., Greiner, U. and Klingenberg, H. (1994). High power diode-pumped Nd:YAG regenerative amplifier for picosecond pulses. Appl. Phys. Lett., 65(16), p.1992.30

[26] Dymott, M. and Weingarten, K. (2001). Picosecond diode-pumped laser

system with 93-W average power and 23-mJ pulse energy. Appl. Opt., 40(18), p.3042.32

[27] Kleinbauer, J., Knappe, R. and Wallenstein, R. (2004). A powerful diode-pumped laser source for micro-machining with ps pulses in the infrared, the visible and the ultraviolet. Applied Physics B, 80(3), pp.315-320.

[28] Nd:VAN regenerative laser amplifier, Manual of High-Q IC-355-800ps Photonics Solutions Laser, 2007

[29] Fianium ultrafast fiber lasers, Official webpage of Fianium laser [Cited Oct.2015; available at: http://www.fianium.com/]

[30] Hendow, S. and Shakir, S. (2010). Structuring materials with nanosecond laser pulses. Opt. Express, 18(10), p.10188.

[31] Bado, P., Clark, W., Said, A. Ultrafast laser micromaching hand book, Official Webpage of Clark-MXR. [Cited Oct. 2015; available at: http://www.cmxr.com/Education/Introduction.html]

[32] Rizvi, N. (2003). Femtosecond Laser Micromachining: Current Status and Applications. RIKEN Review 50, Focused on Laser Precision Microfabrication (LPM 2002): 107-112

[33] Föhl C., Dausinger F. (2006). High precision laser drilling with ultra short pulses - fundamental aspects and technical applications, Proc. PICALO 2: 281-286 34.

[34] Breitling, D., Föhl, C., Dausinger, F., Kononenko, T. and Konov, V. (2004). Drilling of Metals. Topics in Applied Physics, pp.131-156.

[35] Dausinger F. (2003). Femtosecond technology for precision manufacturing: Fundamental and technical aspects, RIKEN Review 50, Focused on Laser Precision Microfabrication (LPM 2002): 77-82

[36] Breitling D., Ruf A., Dausinger F. (2004). Fundamental aspects in machining of metals with short and ultrashort laser pulses, Proc. SPIE 5339: 49-63

[37] O'Shea, D. (1985). Elements of modern optical design. New York: Wiley.

[38] Hecht, E. (1998). Optics. Reading, Mass.: Addison-Wesley.

[39] Image taken from youtube.com. [Cited Oct.2015; available at: https://www.youtube.com/watch?v=Q0qrU4nprB0]

[40] Hall, D. (1996). Vector-beam solutions of Maxwell's wave equation. Optics Letters, 21(1), p.9.

[41] Erdélyi, M. and Gajdátsy, G. (2008). Radial and azimuthal polarizer by means

of a birefringent plate. Journal of Optics A: Pure and Applied Optics, 10(5), p.055007.

[42] Pohl, D. (1972). Operation of a Ruby Laser in the Purely Transverse Electric Mode TE01. Appl. Phys. Lett., 20(7), p.266.

[43] Mushiake, Y., Matsumura, K. and Nakajima, N. (1972). Generation of radially polarized optical beam mode by laser oscillation. Proceedings of the IEEE, 60(9), pp.1107-1109.

[44] Zhan, Q. and Leger, J. (2002). Microellipsometer with radial symmetry. Appl. Opt., 41(22), p.4630.

[45] Allegre, O., Jin, Y., Perrie, W., Ouyang, J., Fearon, E., Edwardson, S. and Dearden, G. (2013). Complete wavefront and polarization control for ultrashort-pulse laser microprocessing. Opt. Express, 21(18), p.21198.

[46] Jin, Y., Allegre, O., Perrie, W., Abrams, K., Ouyang, J., Fearon, E., Edwardson, S. and Dearden, G. (2013). Dynamic modulation of spatially structured polarization fields for real-time control of ultrafast laser-material interactions. Opt. Express, 21(21), p.25333.

[47] Beresna, M., Gecevičius, M., Kazansky, P. and Gertus, T. (2011). Radially polarized optical vortex converter created by femtosecond laser nanostructuring of glass. Appl. Phys. Lett., 98(20), p.201101.

[48] Zhan, Q. and Leger, J. (2002). Focus shaping using cylindrical vector beams. Opt. Express, 10(7), p.324.

[49] Zhan, Q. (2004). Trapping metallic Rayleigh particles with radial polarization. Opt. Express, 12(15), p.3377.

[50] Niziev, V. and Nesterov, A. (1999). Influence of beam polarization on laser cutting efficiency. Journal of Physics D: Applied Physics, 32(13), pp.1455-1461.

[51] Meier, M., Romano, V. and Feurer, T. (2006). Material processing with pulsed radially and azimuthally polarized laser radiation. Appl. Phys. A, 86(3), pp.329-334.

[52] Image taken from Hamamatsu photonics official webpage. [Cited Oct.2015; available at: http://www.hamamatsu.com/eu/en/product/category/3200/4178/index.html]

[53] Efron, U. (1995). Spatial light modulator technology. New York: Marcel Dekker.

[54] KUANG, Z. (2010). Parallel diffractive multi-beam ultrafast laser

micro-processing. PhD thesis, University of Liverpool, UK.

[55] Hamamatsu X10468 series data sheet. [Cited Oct.2015; available at : http://www.hamamatsu.com/resources/pdf/ssd/x10468_series_etc_kacc1172e.pdf]

[56] Spangenberg, D., Dudley, A., Neethling, P., Rohwer, E. and Forbes, A. (2014). White light wavefront control with a spatial light modulator. Opt. Express, 22(11), p.13870.

[57] Moreno, I., Davis, J., Hernandez, T., Cottrell, D. and Sand, D. (2011). Complete polarization control of light from a liquid crystal spatial light modulator. Opt. Express, 20(1), p.364.

[58] Chen, J., Hirayama, T., Ishizuka, K. and Tonomura, A. (1994). Spherical aberration correction using a liquid-crystal spatial-light modulator in off-axis electron holography. Appl. Opt., 33(28), p.6597.

[59] Weiner, A. (2000). Femtosecond pulse shaping using spatial light modulators. Rev. Sci. Instrum., 71(5), p.1929.

[60] Birnbaum, M. (1965). Semiconductor Surface Damage Produced by Ruby Lasers. J. Appl. Phys., 36(11), p.3688.

[61] Guillermin, M., Garrelie, F., Sanner, N., Audouard, E. and Soder, H. (2007). Single- and multi-pulse formation of surface structures under static femtosecond irradiation. Applied Surface Science, 253(19), pp.8075-8079.

[62] Sakabe, S., Hashida, M., Tokita, S., Namba, S. and Okamuro, K. (2009). Mechanism for self-formation of periodic grating structures on a metal surface by a femtosecond laser pulse. Phys. Rev. B, 79(3).

[63] Borowiec, A. and Haugen, H. (2003). Subwavelength ripple formation on the surfaces of compound semiconductors irradiated with femtosecond laser pulses. Appl. Phys. Lett., 82(25), p.4462.

[64] Jiang, L., Shi, X., Li, X., Yuan, Y., Wang, C. and Lu, Y. (2012). Subwavelength ripples adjustment based on electron dynamics control by using shaped ultrafast laser pulse trains. Opt. Express, 20(19), p.21505.

[65] Sipe, J., Young, J., Preston, J. and van Driel, H. (1983). Laser-induced periodic surface structure. I. Theory. Phys. Rev. B, 27(2), pp.1141-1154.

[66] Emmony, D. (1973). Laser mirror damage in germanium at 10.6 μm. Appl. Phys. Lett., 23(11), p.598.

[67] Varlamova, O., Costache, F., Ratzke, M. and Reif, J. (2007). Control parameters in pattern formation upon femtosecond laser ablation. Applied

Surface Science, 253(19), pp.7932-7936.

[68] Vorobyev, A. and Guo, C. (2008). Colorizing metals with femtosecond laser pulses. Appl. Phys. Lett., 92(4), p.041914.

[69] Lochbihler, H. (2009). Colored images generated by metallic sub-wavelength gratings. Opt. Express, 17(14), p.12189.

[70] Dusser, B., Sagan, Z., Soder, H., Faure, N., Colombier, J., Jourlin, M. and Audouard, E. (2010). Controlled nanostructrures formation by ultra fast laser pulses for color marking. Opt. Express, 18(3), p.2913.

[71] Long, J., Fan, P., Zhong, M., Zhang, H., Xie, Y. and Lin, C. (2014). Superhydrophobic and colorful copper surfaces fabricated by picosecond laser induced periodic nanostructures. Applied Surface Science, 311, pp.461-467.

[72] Neale, A., Jin, Y., Ouyang, J., Hughes, S., Hesp, D., Dhanak, V., Dearden, G., Edwardson, S. and Hardwick, L. (2014). Electrochemical performance of laser micro-structured nickel oxyhydroxide cathodes. Journal of Power Sources, 271, pp.42-47.

[73] Sushant, D., Nishant. S., Purohit, R. (2006). A review on laser drilling and its Techniques. Proceedings: International Conference on Advances in Mechanical Engineering-2006 (AME 2006).

[74] Momma, C., Chichkov, B., Nolte, S., von Alvensleben, F., Tünnermann, A., Welling, H. and Wellegehausen, B. (1996). Short-pulse laser ablation of solid targets. Optics Communications, 129(1-2), pp.134-142.

[75] Chichkov, B., Momma, C., Nolte, S., Alvensleben, F. and Tünnermann, A. (1996). Femtosecond, picosecond and nanosecond laser ablation of solids. Appl. Phys. A, 63(2), pp.109-115.

[76] Momma, C., Nolte, S., Kamlage, G., von Alvensleben, F. and Tunnermann, A. (1998). Beam delivery of femtosecond laser radiation by diffractive optical elements. Applied Physics A: Materials Science & Processing, 67(5), pp.517-520.

[77] Preuss, S., Demchuk, A. and Stuke, M. (1995). Sub-picosecond UV laser ablation of metals. Applied Physics A: Materials Science & Processing, 61(1), pp.33-37.

[78] Gotz, T. and Stuke, M. (1997). Short-pulse UV laser ablation of solid and liquid metals: indium. Applied Physics A: Materials Science & Processing, 64(6), pp.539-543.

[79] Sudani, N., Venkatakrishnan, K. and Tan, B. (2009). Laser singulation of thin wafer: Die strength and surface roughness analysis of 80μm silicon dice.

Optics and Lasers in Engineering, 47(7-8), pp.850-854.

[80] Corcoran, A., Sexton, L., Seaman, B., Ryan, P. and Byrne, G. (2002). The laser drilling of multi-layer aerospace material systems. Journal of Materials Processing Technology, 123(1), pp.100-106.

[81] Tönshoff, H., Momma, C., Ostendorf, A., Nolte, S. and Kamlage, G. (2000). Microdrilling of metals with ultrashort laser pulses. Journal of Laser Applications, 12(1), p.23.

[82] Ancona, A., Röser, F., Rademaker, K., Limpert, J., Nolte, S. and Tünnermann, A. (2008). High speed laser drilling of metals using a high repetition rate, high average power ultrafast fiber CPA system. Opt. Express, 16(12), p.8958.

[83] Nolte, S., Momma, C., Kamlage, G., Ostendorf, A., Fallnich, C., von Alvensleben, F. and Welling, H. (1999). Polarization effects in ultrashort-pulse laser drilling. Applied Physics A: Materials Science & Processing, 68(5), pp.563-567.

[84] Föhl, C., Dausinger, F. (2003). High precision deep drilling with ultrashort pulses, Proc. SPIE 5063, 346-351

[85] Dickey, F. and Holswade, S. (2000). Laser beam shaping. New York: Marcel Dekker.

[86] Miyasaka, M. and Stoemenos, J. (1999). Excimer laser annealing of amorphous and solid-phase-crystallized silicon films. J. Appl. Phys., 86(10), p.5556.

[87] Chrisey, D. and Hubler, G. (1994). Pulsed laser deposition of thin films. New York: J. Wiley.

[88] Sugioka, K., Meunier, M. and Piqué , A. (2010). Laser precision microfabrication. Heidelberg: Springer-Verlag.

[89] Garcés-Chávez, V., McGloin, D., Melville, H., Sibbett, W. and Dholakia, K. (2002). Simultaneous micromanipulation in multiple planes using a self-reconstructing light beam. Nature, 419(6903), pp.145-147.

[90] Arlt, J., Hitomi, T. and Dholakia, K. (2000). Atom guiding along Laguerre-Gaussian and Bessel light beams. Applied Physics B: Lasers and Optics, 71(4), pp.549-554.

[91] Molina-Terriza, G., Torres, J. and Torner, L. (2007). Twisted photons. Nat Phys, 3(5), pp.305-310.

[92] Duocastella, M. and Arnold, C. (2012). Bessel and annular beams for materials processing. Laser & Photonics Reviews, 6(5), pp.607-621.

[93] Durnin, J., Miceli, J. and Eberly, J. (1987). Diffraction-free beams. Phys. Rev. Lett., 58(15), pp.1499-1501.

[94] MCLEOD, J. (1954). The Axicon: A New Type of Optical Element. Journal of the Optical Society of America, 44(8), p.592.

[95] Courvoisier, F., Lacourt, P., Jacquot, M., Bhuyan, M., Furfaro, L. and Dudley, J. (2009). Surface nanoprocessing with nondiffracting femtosecond Bessel beams. Optics Letters, 34(20), p.3163.

[96] Wise, F., Chong, A. and Renninger, W. (2008). High-energy femtosecond fiber lasers based on pulse propagation at normal dispersion. Laser & Photonics Review, 2(1-2), pp.58-73.

[97] Andrews, D. (2008). Structured light and its applications. Amsterdam: Academic Press.

[98] Nutfield XLR8 two axis scan head hardware manual. [Cited Oct.2015; available at : https://nutfieldtech.com/xlr8-10-packaged-2-axis-scan-head/]

[99] Zhan, Q. (2009). Cylindrical vector beams: from mathematical concepts to applications. Advances in Optics and Photonics, 1(1), p.1.

[100] Tovar, A. (1998). Production and propagation of cylindrically polarized Laguerre–Gaussian laser beams. Journal of the Optical Society of America A, 15(10), p.2705.

[101] Novotny, L., Beversluis, M., Youngworth, K. and Brown, T. (2001). Longitudinal Field Modes Probed by Single Molecules. Phys. Rev. Lett., 86(23), pp.5251-5254.

[102] Varin, C. and Piché, M. (2002). Acceleration of ultra-relativistic electrons using high-intensity TM01 laser beams. Applied Physics B, 74(S1), pp.s83-s88.

[103] Anoop, K., Rubano, A., Fittipaldi, R., Wang, X., Paparo, D., Vecchione, A., Marrucci, L., Bruzzese, R. and Amoruso, S. (2014). Femtosecond laser surface structuring of silicon using optical vortex beams generated by a q-plate. Appl. Phys. Lett., 104(24), p.241604.

[104] Lou, K., Qian, S., Ren, Z., Wang, X., Li, Y., Tu, C. and Wang, H. (2012). Self-formed two-dimensional near-wavelength microstructures on copper induced by multipulse femtosecond vector optical fields. Journal of the Optical Society of America B, 29(9), p.2282.

[105] Guosheng, Z., Fauchet, P. and Siegman, A. (1982). Growth of spontaneous periodic surface structures on solids during laser illumination. Phys. Rev. B, 26(10), pp.5366-5381.

[106] Huang, M., Zhao, F., Cheng, Y., Xu, N. and Xu, Z. (2009). Origin of Laser-Induced Near-Subwavelength Ripples: Interference between Surface Plasmons and Incident Laser. ACS Nano, 3(12), pp.4062-4070.

[107] Ringermacher, H. and Mead, L. (2009). A new formula describing the scaffold structure of spiral galaxies. Monthly Notices of the Royal Astronomical Society, 397(1), pp.164-171.

[108] Cardano, F., Karimi, E., Marrucci, L., de Lisio, C. and Santamato, E. (2013). Generation and dynamics of optical beams with polarization singularities. Opt. Express, 21(7), p.8815.

[109] Wang, X., Ding, J., Ni, W., Guo, C. and Wang, H. (2007). Generation of arbitrary vector beams with a spatial light modulator and a common path interferometric arrangement. Optics Letters, 32(24), p.3549.

[110] Machavariani, G., Lumer, Y., Moshe, I. and Jackel, S. (2007). Effect of the spiral phase element on the radial-polarization (0,1)∗ LG beam. Optics Communications, 271(1), pp.190-196.

[111] Zhao, Q., Malzer, S. and Wang, L. (2007). Formation of subwavelength periodic structures on tungsten induced by ultrashort laser pulses. Optics Letters, 32(13), p.1932.

[112] Klug, U., Düsing, J., Sato, T., Washio, K. and Kling, R. (2010). Polarization converted laser beams for micromachining applications. Proc. SPIE 7590, 759006.

[113] Gori, F. (2001). Polarization basis for vortex beams. Journal of the Optical Society of America A, 18(7), p.1612.

[114] Intonti, F., Caselli, N., Lawrence, N., Trevino, J., Wiersma, D. and Dal Negro, L. (2013). Near-field distribution and propagation of scattering resonances in Vogel spiral arrays of dielectric nanopillars. New Journal of Physics, 15(8), p.085023.

[115] Allegre, O., Perrie, W., Edwardson, S., Dearden, G. and Watkins, K. (2012). Laser microprocessing of steel with radially and azimuthally polarized femtosecond vortex pulses. Journal of Optics, 14(8), p.085601.

[116] Allegre, O., Perrie, W., Bauchert, K., Liu, D., Edwardson, S., Dearden, G. and Watkins, K. (2012). Real-time control of polarisation in ultra-short-pulse laser micro-machining. Appl. Phys. A, 107(2), pp.445-454.

[117] Zeng, D., Latham, W. and Kar, A. (2005). Two-dimensional model for melting and vaporization during optical trepanning. *J. Appl. Phys.*, 97(10), p.104912.

[118] Rioux, M., Tremblay, R. and Bélanger, P. (1978). Linear, annular, and radial

focusing with axicons and applications to laser machining. *Appl. Opt.*, 17(10), p.1532.

[119] Lipson, S. and Lipson, H. (1969). Optical physics. London: Cambridge U.P.

[120] Hardware implementation of the system transfer function: the 4f correlator. [Cited Oct.2015; available at : https://en.wikipedia.org/wiki/Fourier_optics#Fourier_analysis_and_functional_decomposition]